Non-Euclidean Geometries and Transformation Optics

Timothy Michael McManus

School of Electronic Engineering and Computer Science

Queen Mary, University of London

A thesis submitted to the University of London in partial fulfillment of the requirements for the degree of

Doctor of Philosophy

October 2015

Statement of originality

I, Timothy Michael McManus, confirm that the research included within this thesis is my own work or that where it has been carried out in collaboration with, or supported by others, that this is duly acknowledged below and my contribution indicated. Previously published material is also acknowledged below.

I attest that I have exercised reasonable care to ensure that the work is original, and does not to the best of my knowledge break any UK law, infringe any third partys copyright or other Intellectual Property Right, or contain any confidential material.

I accept that the College has the right to use plagiarism detection software to check the electronic version of the thesis.

I confirm that this thesis has not been previously submitted for the award of a degree by this or any other university.

Signature: Timothy Michael McManus
Date: December 10, 2015

Publications and contributions

Refereed papers

- 'Isotropic and anisotropic surface wave cloaking techniques,' McManus, T. M., La Spada, L. and Hao, Y., *Journal of Optics*, accepted October 30, 2015.
  Contributions: Initial idea, theoretical derivations, numerical modeling, data post-processing and manuscript preparation.

- 'Illusions and cloaks for surface waves,' McManus, T. M., Valiente-Kroon, J. A., Horsley, S. A. R. and Hao, Y., *Scientific Reports*, **4**, 5977 (2014) doi 10.1038/srep05977.
  Contributions: Initial idea, theoretical derivations, numerical analogues to analytical solutions, numerical modeling and manuscript preparation.

- 'Lenses on curved surfaces,' Mitchell-Thomas, R.C., Quevedo-Tereul, O., McManus, T. M., Horsley, S. A. R. and Hao, Y., *Optics Letters*, **39**, Issue 12, 3551-3554 (2014) doi 10.1364/OL.39.003551.
  Contributions: Expansion of theoretical derivations, numerical solutions and manuscript editing.

- 'Perfect surface wave cloaks,' Mitchell-Thomas, R.C., Quevedo-Tereul, O., McManus, T. M., Horsley, S. A. R. and Hao, Y., *Phys. Rev. Lett.*, **111**, 213901(2013) doi 10.1103/PhysRevLett.111.213901.
  Contributions: Expansion of theoretical derivations, numerical solutions and manuscript editing.

Conference papers

- 'The anti-fish eye cloak for surface wave antennas,' Mitchell-Thomas, R. C., Quevedo-Tereul, O., McManus, T. M., Horsley, S. A. R. and Hao, Y., *Proceedings of the 8th European Conference on Antennas and Propagation*, 267-268, The Hague, Netherlands, April 6-11 (2014) doi 10.1109/EuCAP.2014.6901742.
  Contributions: Numerical solutions and manuscript editing.

- 'Conformal surface lenses from a bed of nails,' Quevedo-Tereul, O., Mitchell-Thomas, R. C., McManus, T. M., Horsley, S. A. R. and Hao, Y., *Proceedings of the 8th European Conference on Antennas and Propagation*, 269-270, The Hague,

Netherlands, April 6-11 (2014) doi 10.1109/EuCAP.2014.6901743.
Contributions: Numerical solutions and manuscript editing.

- '2D optical transformations for surfaces,' Mitchell-Thomas, R. C., McManus T. M., Quevedo-Tereul, O. and Hao, Y., *2014 IEEE Antennas and Propagation Society International Symposium*, 761-762, Memphis, Tennessee, U.S.A., July 6-11 (2014) doi 10.1109/APS.2014.6904710.
  Contributions: Theoretical derivation expansion and manuscript editing.

Oral presentations

- 'Asymmetric flat reflector from transformation optics,' McManus, T. M., Yang, R., Quevedo-Teruel, O. and Hao, Y., *Proceedings of the 7th European Conference on Antennas and Propagation*, 1836 - 1839, Gothenburg, Sweden, April 8-12 (2013).
  Contributions: Initial idea, theoretical derivation, numerical modeling and manuscript preparation/presentation.

- 'Current research efforts in transformation optics (non-Euclidean geometries) at QMUL', McManus, T. M., and Hao, Y., United States Army Research Lab, Aberdeen Proving Ground, Maryland, U.S.A., September 4-5 (2013).
  Contributions: Initial idea, theoretical derivation, numerical modeling, software development and manuscript preparation/presentation.

- 'A generalized dipole moment based approach for modelling of nanoparticles,' Naeem, M., McManus, T. M., and Hao, Y., *The 30th International Review of Progress in Applied Computational Electromagnetics*, Jacksonville, Florida, U.S.A., March 23-27 (2014).
  Contributions: Numerical modeling, manuscript editing/presentation.

Funding

This thesis was funded by the Engineering and Physical Sciences Research Council (EPSRC), UK under a Programme Grant (EP/I034548/1) 'The Quest for Ultimate Electromagnetics using Spatial Transformations (QUEST)'.

To my friends and family

Acknowledgements

Firstly, I would like to thank my family (Tim, Joyce and Paige) for supporting me throughout my entire academic career. Also, I would like to thank my supervisors Prof. Yang Hao, and Dr. Juan Valiente-Kroon for their guidance during my doctoral candidacy. Lastly, I would like to thank Dr. Oscar Quevedo-Teruel, Dr. Rhiannon Mitchell-Thomas and Dr. Simon Horsley all of whom played an important role in my PhD.

Abstract

The purpose of this thesis was to use the theory of transformation optics (TO) to control light along non-Euclidean surfaces. Chapter 2 provides an introduction to the fundamental theory of TO, the basics of non-Euclidean geometries, and a broad chronological overview of TO from its inception to the time this thesis was written. Chapter 3 details a novel application of Fermat's principle to cloak rotationally symmetric surface deformations from surface waves using an isotropic, all-dielectric, electrically thin material overlay. Also in this chapter, a realizable surface wave cloaking device is designed and its performance is validated. Chapter 4 builds directly upon Chapter 3 and describes how to map a rotationally symmetric flat lens onto a rotationally symmetric surface deformation via an isotropic, all-dielectric, electrically thin material overlay. This chapter also includes the design and validation of two realizable surface wave lenses borne out of this approach. Chapter 5 addresses the primary limiting design factor found in Chapter 3 and 4 (rotational symmetry), by deriving from Maxwell's equations, an equivalence to handle rotationally asymmetric or more generally 'arbitrary' surfaces. This work is significant because it provides a truly general solution to the problem of creating cloaks and illusion devices for surface wave applications. Finally, in Chapter 6 for the first time, a direct comparative study of two distinct surface wave cloaking techniques, from Chapter 3 and Chapter 5, is conducted and the results are examined.

Contents

List of Figures

List of Tables

Chapter 1

Introduction

1.1 Aim of research

The aim of the work presented in this thesis is to derive, implement and validate different techniques to manipulate electromagnetic (EM) surface waves on non-Euclidean geometries via transformation optics (TO). The techniques borne out of this work include a unique application of Fermat's principle as well as a fundamental ground-up derivation used to link curved and flat surfaces. The first technique calls for an electrically thin isotropic material overlay whereas the second calls for an anisotropic one. Central to both of these methods is the geometrical optics (GO) approximation due to the fact that the surface deformations under investigation are electrically large. Lastly, a large part of this work involves the development and testing of a novel suite of numerical tools that are used to solve for the required device properties.

1.2 Outline

1.2.1 Background

Chapter 2 provides a review of the fundamentals of TO starting with the idea of a spatial transformation media which effectively performs a coordinate transformation between what is known as the virtual and physical spaces. Moreover, there is a focus on understanding wave propagation in both isotropic and anisotropic media, and when appreciable differences arise (e.g. via the constitutive relations between electric field strength and dielectric displacement), they are examined. Also, the geometrical optics (GO) approximation is introduced and the conditionals required for it be a good approximation of the wave equation are studied. Next, a brief introduction to non-Euclidean geometries is presented and the fundamental differences between Euclidean

and non-Euclidean geometries, in their broadest sense, are listed. As the majority of this thesis focuses on two-dimensional manifolds (surfaces), a suitable parameter is put forth that clearly demonstrates the type (Euclidean or non-Euclidean) of surface under investigation. Lastly, a literature review of TO is conducted starting with the founding theoretical works. Next, a yearly-segmented chronological literature review (starting in 2006 and ending in mid-2015) is presented and the role of TO in, but not limited to, fundamental theory, numerical modeling, device design and experimental validation is examined. Also during this review extra commentary is included on works that are particularly novel and influential. The literature review is concluded with an examination of three works that use the idea of non-Euclidean geometries in the context of TO.

1.2.2 Rotationally symmetric surface wave cloaks

In Chapter 3 a new method (fundamentally different from previous methods proposed by transformation plasmonics), utilizing Fermat's principle, is used to create an omnidirectional, purely dielectric, electrically thin material overlay to cloak a finite, curved (i.e. non-Euclidean) surface deformation from surface waves in the microwave regime. First its derivation is produced and a number of sample surface deformations (hemispheric, conic and Gaussian) are studied. Then, a numerical solution is derived to account for any limitations, found in the analytical approach when $R(\theta)$ (which is related to the profile of a given surface deformation) can not be expressed in a closed-form. Next, the parallel plate waveguide simulation technique is introduced and the performance of a hemispheric, conic and Gaussian cloak is investigated using a full-wave EM solver. Here it is demonstrated that the curvature, K, mismatch between the surface deformation and the flat approach plane leads to undesirable scattering and because of this a particular focus is placed on surfaces that did not have this problem (i.e. a Gaussian surface). To further quantify the performance of each cloak, a sampling line study is carried out and it is determined that the Guassian-shaped cloak most closely emulates the wave behavior of a plane wave traveling in a flat waveguide.

Next, to convert the proposed material solution from its parallel plate waveguide form into a real surface wave form, the required material parameters (i.e. ε_r) for a thin material on a perfect electric conductor (PEC) ground plane are determined via the use of a commercially available EM solver. These results are then used to design an all-dielectric material overlay of uniform thickness, that would cloak a cosine-shaped surface deformation from a surface wave. The proposed device is then simulated using a commercial EM solver and it is demonstrated that the surface wave cloak design functioned properly in the desired frequency band and possesses a good level of modal

confinement. The surface wave cloaking design recipe described in this chapter is novel because it leads to the creation of a thin, isotropic, all-dielectric material overlay that can be used to cloak a rotationally symmetric surface deformation for all angles of incidence over a given frequency band.

1.2.3 Rotationally symmetric surface wave lenses

In Chapter 4 a realizable method for mapping flat, isotropic, surface wave lens onto rotationally symmetric surface deformations is put forward. First, the design recipe first used in Chapter 3 is expanded to allow for the mapping of flat refractive index profiles onto rotationally symmetric surfaces. To demonstrate how one does this, a number of analytical examples are gone through step-by-step which include the mapping of: a black hole lens onto a hemispheric deformation, a Luneburg lens onto a conic deformation, a Luneburg lens onto a hemispheric deformation and a Maxwell's fish eye (MFE) lens onto a hemisphere. The final case of attempting to map a MFE lens onto a hemispheric surfaces leads to the idea of an 'equivalent surface', which in its simplest sense is a curved homogeneous surface that behaves, electrically speaking, in the same fashion as its flat, inhomogeneous analogue. A general method for obtaining the equivalent surface of a flat lens is then derived and the relation between a hemispheric deformation and a MFE lens is used to check its validity. A numerical solution for mapping lenses onto curved surfaces is later derived for instances where $R(\theta)$ of a given rotationally symmetric surface are not expressible in closed-form. Moving on, a parallel plate waveguide simulation technique used in Chapter 3 is implemented once again. Here the performances of Luneburg lens and a MFE lens in a number of configurations are investigated using a commercial full-wave EM solver. Here it is demonstrated (as was also witnessed in Chapter 3) that the curvature, K, mismatch between the surface deformation and the flat approach plane leads to undesirable pattern characteristics. Of all the curved surface lens configurations those that avoided these curvature discontinuities function (emulate the behavior of their flat lens analogues) the best.

Finally, in an attempt to convert the proposed material solution from its parallel plate waveguide form into a real surface wave form, the required material properties for a thin material overlay on a PEC ground plane are determined. Here instead of maintaining the thickness of the material overlay and varying ε_r as is done in Chapter 3, the opposite is done were ε_r is maintained ($\varepsilon_r = 15$) and the thickness of the material overlay is varied according to a calculated relation between material thickness and modal refractive index. This design strategy is particularly interesting as it can be realized via the increasingly accessible rapid fabrication technique of 3D printing. To demonstrate the efficacy of the proposed designs they are simulated using a commercial full-wave

EM solver. Here it is demonstrated that the material realizations of the Luneburg lens and the MFE lens on a cosine-shaped PEC deformation function properly in a given frequency band. These simulation results also reveal a good level of modal confinement across said band as well. The curved surface wave lens design recipe described in this chapter is novel because it leads to the creation of a thin, isotropic, homogeneous material overlay that can be used to control the propagation of surface waves (via a lens) along nearly any smooth rotationally symmetric PEC surface deformation.

1.2.4 Cloaks and illusion devices for general surfaces

In Chapter 5 the structural limitations found in Chapter 3 and Chapter 4, namely the required rotational symmetry of the surface deformation, are addressed. In order to do so, a fundamentally different approach needs to be considered that could deal with rotationally asymmetric surfaces (RASs). First, in the case of the illusion device (a flat materially inhomogeneous device that emulates the scattering characteristics of a curved homogeneous device), a ground-up derivation is developed and the prescribed material properties for an example surface (an asymmetric Gaussian deformation) are discussed. Then, moving onto the cloaking of a RAS, another ground-up derivation is provided to cloak smooth surface deformations. Afterwards, a numerical solution is put forward to handle computer-aided design (CAD) surfaces, and the validity of the proposed technique is tested in both one and two dimensions.

In order to validate that the prescribed material loadings borne out of the proposed techniques do in fact create the desired devices, the parallel plate waveguide simulation technique used in Chapter 3 is implemented in a commercially available full-wave electromagnetic solver. Here it is demonstrated that the scattering characteristics of the RAS can be faithfully recreated by an illusion device. To quantify just how well the illusion device functions a sample line study is conducted and it is found that an excellent level of agreement exists between the curved RAS and the flat illusion device. Next, the numerical technique found within this chapter is used to calculate the required material properties to create an illusion device for a CAD surface, and it is demonstrated that it successfully recreates the scattering characteristics of its curved analogue for two different angles of incidence. Lastly, the same RAS used in the analytically defined illusion device case study, is shown to be completely cloaked for two different angles of incidence and the efficacy of cloak itself is quantified by analyzing the field distribution along two different sample lines (one for each angle of incidence). Owing to the material complexity of the proposed devices it is noted that fabricating a true surface wave device, though outside the domain of this thesis, may be obtainable using a variety of different techniques found within the metasurface community.

The surface wave illusion and cloaking design recipe described in this chapter is novel because it can be applied to nearly any smooth surface (whether its form is known analytically or in the form of a CAD file, hence the term 'general'), as well as the fact that all the devices borne out of it are omnidirectional.

1.2.5 A comparative study of cloaking schemes

Chapter 6 describes a direct, comparative study between the surface wave cloaking techniques introduced in Chapter 3 and Chapter 5. The cloak from Chapter 3 is refereed to as an isotropic surface wave cloak (ISC) and the cloak from Chapter 5 is referred to as an anisotropic surface wave cloak (ASC), due to the material properties called for by the two techniques. Owing to the limiting factor of rotational symmetry inherent to the ISC approach, a surface deformation amenable to both techniques is studied. The simulation method used in the Chapter 3 and Chapter 5 is implemented via commercial full-wave EM solver and the performance of both of the cloaks for multiple angles of incidence is analyzed. As the two cloaks behave virtually identically when inspecting the amplitude of their scattered E-field, focus is instead put on the performance of their scattered magnitude and phase which allows for clear distinctions to be made. To add a more robust quantification of the surface wave cloaks performance, the idea of a 'bounding ring' is introduced which is designed to capture the omnidirectional scattering of the surface deformations. Lastly, in an attempt to quantify the performance of a surface wave cloak with a single value, a mean absolute error calculation is performed and the results for the different cloaking techniques are analyzed. The comparative study described in this chapter is unique because it is the first of its kind to directly compare two disparate surface wave cloaking techniques through the use a performance metric (i.e. MAE and weighted MAE) that is specifically crafted to encapsulate the important characteristics of surface wave cloaks.

Chapter 2

Background

2.1 Introduction

In this chapter a number of key ideas are introduced and explained that form the foundation of this thesis. First, the fundamentals of transformation electromagnetics, often refereed as transformation optics (TO), are investigated. To start, the empty-space Maxwell's equations in an arbitrary coordinate system are introduced and their equivalence (via scaling and constitutive relations) to the media-filled macroscopic Maxwell's equations in a Cartesian coordinate system are derived. This forms the basis of what comes to be regarded as a spatial transformation media which effectively performs a coordinate transformation between what is known as the virtual and physical spaces. Moreover, throughout said derivation, there is a focus on understanding wave propagation (namely with respect to the wave vector $\boldsymbol{k}$) in both isotropic and anisotropic media, and when appreciable differences arise (e.g. via the constitutive relations between electric field strength and dielectric displacement), they are examined. Afterwards, the geometrical optics (GO) approximation is introduced and the conditionals required for it be a good approximation of the wave equation are studied. Finally, Maxwell's equations are rewritten in the limits of GO and an examination of the wave vector as it relates to the dielectric properties of an anisotropic media (or conversely a curved space) is conducted.

Next, a brief introduction to non-Euclidean geometries is presented. Here the fundamental differences between Euclidean and non-Euclidean geometries, in their broadest sense, are listed. As the majority of this thesis focuses on two-dimensional manifolds (surfaces), a suitable parameter is put forth that clearly demonstrates the type (i.e. Euclidean or non-Euclidean) of surface under investigation. Also, a clear explanation as to how this thesis fits into the greater body of work that is TO as well as to how it is fundamentally different from other efforts is provided.

Lastly, a literature review of TO is conducted. First, the founding theoretical works are examined and the impact of the coordinate transformations espoused by TO are noted in fields well outside the traditional influences of electromagnetics. Next, a yearly-segmented chronological literature review (starting in 2006 and ending in mid-2015) is presented and the role of TO in, but not limited to, fundamental theory, numerical modeling, device design and experimental validation is examined. Also during this review extra commentary is included on works that are particularly novel and influential. The literature review is then followed by an examination of three works that use the idea of non-Euclidean geometries in the context of TO.

2.2 Maxwell's equations

Fundamental to the understanding of TO, is how Maxwell's equations form a link between geometries and dielectric media. An excellent review of how Maxwell's equations appear in the context of TO is provided by Leonhardt and Philbin [1] and is summarized in this chapter with a particular focus on the relation between geometry and media, geometrical optics (GO), and the conditionals required for GO to be a good approximation to the wave equation. To start, Maxwell's equations relating the electric field strength, $\underline{E}$, and the magnetic induction, $\underline{B}$, in empty, Cartesian flat space [2] are introduced as

$$\nabla \cdot \underline{E} = \frac{\rho}{\varepsilon_0}, \tag{2.1a}$$

$$\nabla \times \underline{B} = \frac{1}{c^2}\frac{\partial \underline{E}}{\partial t} + \mu_0 \underline{j}, \tag{2.1b}$$

$$\nabla \times \underline{E} = -\frac{\partial \underline{B}}{\partial t}, \tag{2.1c}$$

$$\nabla \cdot \underline{B} = 0, \tag{2.1d}$$

where, from (2.1a) to (2.1d), the following are described: Gauss's law, Ampere's law with Maxwell's displacement current, Faraday's law of induction and the absence of magnetic monopoles. Also, as is traditionally the case, SI units are used, with ε_0, μ_0 and c, representing the electric permittivity, magnetic permeability and the speed of light, respectively, all in a vacuum. Lastly, ρ is the charge density and $\underline{j}$ is the current density. Note that unless otherwise stated, the Cartesian coordinate system is employed throughout this thesis. The equations in (2.1) can be recast in arbitrary

spatial coordinates, via the following relations,

$$\nabla \cdot \underline{V} = \frac{1}{\sqrt{g}} \partial_i \sqrt{g} V^i, \tag{2.2a}$$

$$(\nabla \times \underline{V})^i = \epsilon^{ijk} V_{k,j}, \tag{2.2b}$$

as

$$\frac{1}{\sqrt{g}} \left(\sqrt{g} E^i\right)_{,i} = \frac{\rho}{\varepsilon_0}, \tag{2.3a}$$

$$\epsilon^{ijk} H_{k,j} = \varepsilon_0 \frac{\partial E^i}{\partial t} + j^i, \tag{2.3b}$$

$$\epsilon^{ijk} E_{k,j} = -\mu_0 \frac{\partial H^i}{\partial t}, \tag{2.3c}$$

$$\frac{1}{\sqrt{g}} \left(\sqrt{g} H^i\right)_{,i} = 0, \tag{2.3d}$$

where $\underline{B} = \mu_0 \underline{H}$, via the constitutive relation, g is the determinant of the metric tensor g_{ij} and ϵ^{ijk} is defined as

$$\epsilon^{ijk} = \pm \frac{1}{\sqrt{g}} [ijk] \,. \tag{2.4}$$

For those unfamiliar with the notation used in (2.3) or new to tensor analysis, the author suggests reading the first section of the Appendix before proceeding. Here, the reader can find information on: raising and lowering indices, covariant and contravariant differentiation, the Riemann tensor, derivative notation, divergence, curl and the Laplacian. A more thorough introduction to the field can be found in [1, 3–8]. Returning to (2.4), the permutation (Levi-Civita) symbol $[ijk]$ is defined by

$$[ijk] = \begin{cases} +1, & \text{if ijk is an even permutation of 123,} \\ -1, & \text{if ijk is an odd permutation of 123,} \\ 0, & \text{otherwise.} \end{cases} \tag{2.5}$$

Here it is important to point out that the $\pm$ symbol found in (2.4) is a direct result of $[ijk]$ being a psuedo-tensor in that its components can undergo a sign change in a coordinate transformation (e.g. when going from left to right-handed coordinates), in addition to the usual transformation laws. Rewriting (2.3) with all the vector indices in the lower position (see Appendix) and using the following relation described in (2.4),

(2.3) can be recast as

$$\left(\sqrt{g}g^{ij}E_j\right)_{,i} = \frac{\sqrt{g}\rho}{\varepsilon_0}, \tag{2.6a}$$

$$[ijk]H_{k,j} = \varepsilon_0 \frac{\partial\left(\pm\sqrt{g}g^{ij}E_j\right)}{\partial t} \pm \sqrt{g}j^i, \tag{2.6b}$$

$$[ijk]E_{k,j} = -\mu_0 \frac{\partial\left(\pm\sqrt{g}g^{ij}H_j\right)}{\partial t}, \tag{2.6c}$$

$$\left(\sqrt{g}g^{ij}H_j\right)_{,i} = 0. \tag{2.6d}$$

Maxwell's equations in the form of (2.6), which represent empty curved space, resemble the macroscopic Maxwell equations in a dielectric media [2] which are

$$\nabla \cdot \underline{D} = \underline{\varrho}, \tag{2.7a}$$

$$\nabla \times \underline{H} = \frac{\partial \underline{D}}{\partial t} + \underline{J}, \tag{2.7b}$$

$$\nabla \times \underline{E}, = -\frac{\partial \underline{B}}{\partial t}, \tag{2.7c}$$

$$\nabla \cdot \underline{B} = 0, \tag{2.7d}$$

where $\underline{D}$ and $\underline{H}$ are the dielectric displacement and magnetic field strength, respectively. Using right-handed Cartesian coordinates, (2.7) can be written as

$$D^i_{,i} = \varrho, \tag{2.8a}$$

$$[ijk]H_{k,j} = \frac{\partial D^i}{\partial t} + J^i, \tag{2.8b}$$

$$[ijk]E_{k,j} = -\frac{\partial B^i}{\partial t}, \tag{2.8c}$$

$$B^i_{,i} = 0. \tag{2.8d}$$

Upon inspection of (2.6) and (2.8) it is revealed that the laws in (2.6) can be expressed in terms of their macroscopic analogues in (2.8) via the following scaling relations

$$\varrho = \pm\sqrt{g}\rho, \tag{2.9a}$$

$$J^i = \pm\sqrt{g}j^i, \tag{2.9b}$$

and constitutive equations

$$D^i = \varepsilon_0 \varepsilon^{ij} E_j, \tag{2.10a}$$

$$B^i = \mu_0 \mu^{ij} H_j, \tag{2.10b}$$

$$\varepsilon^{ij} = \mu^{ij} = \pm\sqrt{g} g^{ij}, \tag{2.10c}$$

where ε^{ij} and μ^{ij} are given in terms of the geometry. Equation (2.10c) is extremely powerful, because it states that an equivalence exists between empty-space Maxwell's equations in arbitrary coordinates and geometries and the macroscopic Maxwell's equations in right-handed Cartesian coordinates. In effect it shows how geometries can be regarded as dielectric media and vice versa.

Examination of ε^{ij} and μ^{ij} reveal a number of important features. First, it should be noted that ε^{ij} and μ^{ij} are real, symmetric matrices, because g^{ij} is itself real and symmetric [1]. That being said ε^{ij} and μ^{ij}, can also be expressed in matrix form as $\boldsymbol{\varepsilon}$ and $\boldsymbol{\mu}$, respectively, as will be done in the remainder of this derivation when it eases explanations. Moving on, as $\boldsymbol{\varepsilon}$ is a matrix, it follows that the dielectric displacement, $\underline{D} = \varepsilon_0 \boldsymbol{\varepsilon} \underline{E}$, will not always point in the direction of $\underline{E}$. As is also the case for $\underline{B}$ and $\underline{H}$ ($\underline{B} = \mu_0 \boldsymbol{\mu} \underline{H}$). Traditionally, when such a relation exists in a media (e.g. certain crystals) it is referred to as anisotropic. However, it is important to keep in mind that unlike most anisotropic media (whether man made or naturally occurring), the media borne out of (2.10c) is impedance-matched ($\eta = \sqrt{\mu/\varepsilon}$) because $\boldsymbol{\varepsilon} = \boldsymbol{\mu}$. This effectively means that spatial geometries appear as anisotropic impedance-matched media. It is possible to show that the converse is also true by noting that $\det\boldsymbol{\varepsilon} = \pm\sqrt{\det \boldsymbol{g}} = \pm\sqrt{g}$, which then means that

$$g^{ij} = \frac{\varepsilon^{ij}}{\det\boldsymbol{\varepsilon}}, \tag{2.11}$$

which in matrix notation appears as

$$\boldsymbol{g} = (\det\boldsymbol{\varepsilon})\, \boldsymbol{\varepsilon}^{-1}. \tag{2.12}$$

Looking ahead, it is advantageous at this point to discuss how the refractive index appears in an impedance-matched anisotropic media. It is known from Fermat's principle [9] that the geometry of light in an isotropic media is a function of the refractive index. More specifically, the principle states that light rays follow extremal paths (most often the ones of the shortest optical length - geodesics). As pointed out by Leonhardt and Philbin [1], in the case of flat, isotropic materials this is a straight-forward concept and the refractive index can be regarded as the ratio of $\mathrm{d}s$ and $\mathrm{d}l$, which are the length elements perceived by the light, and the length element in the physical space,

respectively. Now in the case of anisotropic media borne out of the above equivalence this relation becomes more complex in that $\mathrm{d}s$ is also now dependent upon direction.

Nevertheless, as a result of $\boldsymbol{\varepsilon}$ being real and symmetric, it is possible to align the axes of a local Cartesian coordinate system with the eigenvectors of $\boldsymbol{\varepsilon} = \boldsymbol{\mu}$. These local eigenvalues of $\boldsymbol{\varepsilon}$ are denoted as $\{\varepsilon_x, \varepsilon_y, \varepsilon_z\}$ in such a way that

$$\boldsymbol{\varepsilon} = \mathrm{diag}\left(\varepsilon_x, \varepsilon_y, \varepsilon_z\right), \tag{2.13a}$$

$$\mathrm{det}\boldsymbol{\varepsilon} = \varepsilon_x \varepsilon_y \varepsilon_z, \tag{2.13b}$$

where $\{\varepsilon_x, \varepsilon_y, \varepsilon_z\}$ are regarded as principal values. Take for example, a line element $\mathrm{d}z$ in the z-direction and placing it in (2.12) shows that the square of the corresponding optical line element is $\varepsilon_x \varepsilon_y \mathrm{d}x^2$. This then implies that the square of the refractive index n_z in the z-direction must be $\varepsilon_x \varepsilon_y$. Carrying out a similar operation for line elements in the other directions the following can be established

$$\mathrm{diag}\left(n_x^2, n_y^2, n_z^2\right) = \mathrm{diag}\left(\varepsilon_y \varepsilon_z, \varepsilon_z \varepsilon_x, \varepsilon_x \varepsilon_y\right), \tag{2.14}$$

which reveals that the refractive index in a given direction of the local eigensystem dielectric matrix depends on the dielectric properties in the orthogonal directions. Ultimately this is to be expected because electromagnetic waves are transversal in that their field are oriented in a direction orthogonal to the direction of propagation. Expressing the refractive index as $\boldsymbol{n} = \mathrm{diag}\left(n_x, n_y, n_z\right)$, and solving for the matrix product $\boldsymbol{n} \otimes \boldsymbol{n}$ one finds

$$\boldsymbol{n}^2 = \left(\mathrm{det}\boldsymbol{\varepsilon}\right) \boldsymbol{\varepsilon}^{-1} = \boldsymbol{g}, \tag{2.15}$$

which when

$$\boldsymbol{\varepsilon} = \boldsymbol{\mu} = \begin{pmatrix} \varepsilon_{xx} & \varepsilon_{xy} & \varepsilon_{xz} \\ \varepsilon_{yx} & \varepsilon_{yy} & \varepsilon_{yz} \\ \varepsilon_{zx} & \varepsilon_{zy} & \varepsilon_{zz} \end{pmatrix}, \tag{2.16}$$

equals

$$\boldsymbol{n}^2 = \begin{pmatrix} \varepsilon_{yy}\varepsilon_{zz} - \varepsilon_{yz}\varepsilon_{zy} & \varepsilon_{xz}\varepsilon_{zy} - \varepsilon_{xy}\varepsilon_{zz} & \varepsilon_{xy}\varepsilon_{yz} - \varepsilon_{xz}\varepsilon_{yy} \\ \varepsilon_{yz}\varepsilon_{zx} - \varepsilon_{yx}\varepsilon_{zz} & \varepsilon_{xx}\varepsilon_{zz} - \varepsilon_{xz}\varepsilon_{zx} & \varepsilon_{xz}\varepsilon_{yx} - \varepsilon_{xx}\varepsilon_{yz} \\ \varepsilon_{yx}\varepsilon_{zy} - \varepsilon_{yy}\varepsilon_{zx} & \varepsilon_{xy}\varepsilon_{zx} - \varepsilon_{xx}\varepsilon_{zy} & \varepsilon_{xx}\varepsilon_{yy} - \varepsilon_{xy}\varepsilon_{yx} \end{pmatrix}. \tag{2.17}$$

An important feature to note in (2.14) is that it is valid for anisotropic impedance-matched media at rest, because it is independent of the eigenvector system established by $\boldsymbol{\varepsilon}$. In turn, (2.14) demonstrates how $\boldsymbol{n}$ is related to the dielectric properties of a media which further generalizes Fermat's principle, as it was introduced previously, in that it shows that the $\boldsymbol{n}^2$ effectively establishes the metric of light.

2.2.1 Transformation media and electromagnetic waves

In the preceding derivation, the empty-space Maxwell's equations in an arbitrary coordinate system were interpreted as if they were in fact in a right-handed Cartesian system with an effective medium. At first this may be puzzling as to why someone would want to do this, but [1] provides a clear and systematic explanation concerning how to interpret and utilize this approach. First, it is important not only to regard these two sets of equations as having different coordinate systems, but also as two different spaces, which may or may not have a dielectric within them. For example, what is usually called the virtual space has no medium within it, and in turn the free-space Maxwell's equations in a right-handed Cartesian coordinate system are used to describe it. The choice of coordinate system to describe a space will be discussed later, and Cartesian coordinates are chosen here simply to be consistent with the previous derivation. Moving on, a transformation is then performed which results in the creation of an effective media (2.10c), and these transformed coordinates are regarded as the physical space which contains said media. In turn this effective medium can be regarded as a transformation media because it performs a coordinate transformation of Maxwell's equations between the virtual and physical spaces (see Figure 2.1). This technique provides a very important tool in that it provides a concise way to determine the effect a medium will have on the propagation of light.

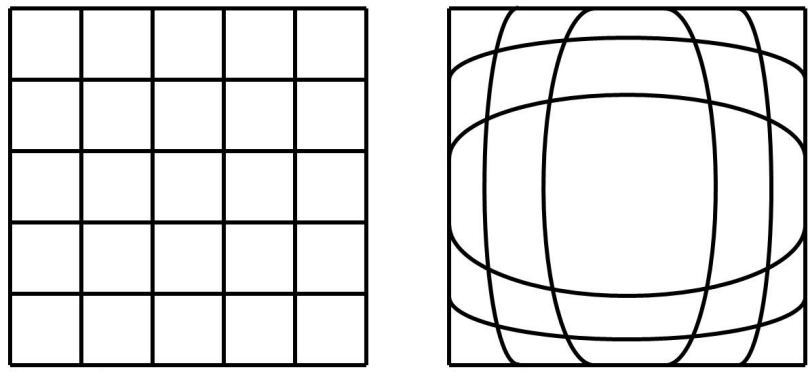

Figure 2.1: A sample virtual space (left) and corresponding physical space (right). Note the use of x'^i to define points in the virtual space and x^i to define those in the physical space.

Letting x'^i represent a curvilinear system (cylindrical, spherical, etc.) and g_{ij} rep-

resent the metric tensor of, the empty-space Maxwell's equations (2.3) appear as

$$\frac{1}{\sqrt{g}}\left(\sqrt{g}E^i\right)_{,i} = \frac{\rho}{\varepsilon_0}, \tag{2.18a}$$

$$[ijk]H_{k,j} = \varepsilon_0\frac{\partial\sqrt{g}E^i}{\partial t} + \sqrt{g}j^i, \tag{2.18b}$$

$$[ijk]E_{k,j} = -\mu_0\frac{\partial\sqrt{g}H^i}{\partial t}, \tag{2.18c}$$

$$\frac{1}{\sqrt{g}}\left(\sqrt{g}H^i\right)_{,i} = 0, \tag{2.18d}$$

and using the same curvilinear coordinate system, x'^i, but γ_{ij} to represent the metric tensor, the macroscopic Maxwell equations in a media (2.8) representing the physical space, can be recast as

$$\left(\sqrt{\gamma}D^i\right)_{,i} = \sqrt{\gamma}\rho, \tag{2.19a}$$

$$[ijk]H_{k,j} = \frac{\partial\sqrt{\gamma}D^i}{\partial t} + \sqrt{\gamma}j^i, \tag{2.19b}$$

$$[ijk]E_{k,j} = -\frac{\partial\sqrt{\gamma}B^i}{\partial t}, \tag{2.19c}$$

$$\left(\sqrt{\gamma}B^i\right)_{,i} = 0. \tag{2.19d}$$

Just as was the case before, (2.18) can be interpreted as (2.19) if the charge and current densities are rescaled, as was done in (2.13), and the constitutive relation

$$\varepsilon^{ij} = \mu^{ij} = \pm\frac{\sqrt{g}}{\sqrt{\gamma}}g^{ij}, \tag{2.20}$$

is established. If the virtual space is not a vacuum, but is instead comprised of an isotropic medium with permittivity ε' and permeability μ' (where the character $'$ denotes relation to the virtual space) then (2.20) becomes

$$\varepsilon^{ij} = \pm\frac{\sqrt{g}}{\sqrt{\gamma}}g^{ij}\varepsilon', \tag{2.21a}$$

$$\mu^{ij} = \pm\frac{\sqrt{g}}{\sqrt{\gamma}}g^{ij}\mu'. \tag{2.21b}$$

Further expanding (2.21) to account for the case when different coordinate systems are employed to represent the virtual and physical spaces, requires the use of the transformation matrix (sometimes refereed to as the Jacobian) $\mathbf{\Lambda}$, where

$$\mathbf{\Lambda} = \Lambda^i_{i'} = \frac{\partial x^i}{\partial x^{i'}}, \tag{2.22}$$

and after some manipulation (2.21) can be recast in matrix form as

$$\boldsymbol{\varepsilon} = \frac{\sqrt{g'}}{\sqrt{\gamma}} \frac{\boldsymbol{\Lambda} \left(\boldsymbol{g'}\right)^{-1} \boldsymbol{\Lambda}^T}{\det \boldsymbol{\Lambda}} \varepsilon' \tag{2.23a}$$

$$\boldsymbol{\mu} = \frac{\sqrt{g'}}{\sqrt{\gamma}} \frac{\boldsymbol{\Lambda} \left(\boldsymbol{g'}\right)^{-1} \boldsymbol{\Lambda}^T}{\det \boldsymbol{\Lambda}} \mu', \tag{2.23b}$$

which describes a highly general transformation. Here it is worth noting that when the virtual space is filled with an isotropic media (ε' and μ'), ε^{ij} and μ^{ij} are proportional to each other according to (2.21), and this means that the physical space may no longer be impedance-matched to free-space. That being said, (2.23) provides a direct method to produce spatial transformation media, and this technique will serve as a guide for a derivation involving electromagnetic waves confined to a surface later in this thesis.

In preparation for the introduction of geometric optics it is useful to develop the wave equation in a form that can be easily coupled with what has been previously derived. First, assume that the medium of interest is time-independent, and impedance match ($\boldsymbol{\varepsilon} = \boldsymbol{\mu}$), and there are no current or charges present, then from (2.3) the wave equation appears as

$$\epsilon^{ijk} \left(\epsilon_{klm} E^{m;l}\right)_{;j} + \frac{1}{c^2} \frac{\partial^2 E^i}{\partial t^2} = 0, \tag{2.24}$$

where derivatives are expressed as covariant derivatives (;), as opposed to contravariant (,) as was done in (2.3), to simplify the following derivations. Using the notation $\nabla_i V^j \equiv V^j_{;} i$ (see Appendix) and the formula $\epsilon^{ijk}\epsilon_{klm} = g^i_l g^j_m - g^i_m g^j_l$ (2.24) becomes

$$\frac{1}{c^2} \frac{\partial^2 E^i}{\partial t^2} = \nabla^j \nabla_j E^i - \nabla_j \nabla^i E^j, \tag{2.25}$$

which after lowering the index of E_i and using the commutator: $\left(\nabla_k \nabla_l - \nabla_l \nabla_k\right) U^i = R^i_{jkl} U^j$ takes on the form

$$\frac{1}{c^2} \frac{\partial^2 E^i}{\partial t^2} = \nabla^j \nabla_j E_i - R^k_{jki} E^j. \tag{2.26}$$

Contracting indices, the second order Riemann tensor (see Appendix), R^k_{jki}, appears as the Ricci tensor, R_{ij} and (2.26) is recast as

$$\nabla^j \nabla_j E^i - R_{ij} E^j - \frac{1}{c^2} \frac{\partial^2 E_i}{\partial t^2} = 0, \tag{2.27}$$

which when taken in conjunction with

$$\nabla_i E^i = 0, \tag{2.28}$$

completely describes the behavior of an electromagnetic wave purely in terms of the electric field. This derivation can be adapted to describe the electromagnetic wave purely in terms of the magnetic field as well, assuming an impedance-matched medium (or its effective geometry) is under investigation. In conclusion, what has been derived thus far forms the foundation of transformation optics (TO).

2.2.2 Geometrical optics

Geometric optics (GO), sometimes refereed to as ray optics, makes approximative statements about full electromagnetic waves (e.g. (2.27)) were the waves are regarded as modulated plane waves with a slowly varying amplitude and a rapidly oscillating phase. In order to determine when GO is a valid approximation, it is important to quantify certain conditionals that relate to GO. To start the electromagnetic field strengths, are treated as complex quantities ($\mathcal{E}_i$ and $\mathcal{H}_i$) oscillating at positive frequencies with

$$E_i = \mathcal{E}_i \mathrm{e}^{i\phi}, H_i = \mathcal{H}_i \mathrm{e}^{i\phi}, \tag{2.29}$$

where ϕ is phase. It should be noted that in order for E_i to describe an actual electromagnetic wave propagating through space in time, $E_i = \mathcal{E}_i \mathrm{e}^{i\phi} + \mathcal{E}_i^* \mathrm{e}^{-i\phi}$, but through superposition [10] the negative-frequency components are always following the positive-frequency components and there is no loss in generality by just focusing on the positive-frequency components as will be done throughout this discussion. Moving on, it is assumed that the variation of phase is more rapid than any changes in the amplitude of the fields and the medium through which the wave is traveling. Furthermore, it is assumed that ϕ progresses in time with constant angular frequency, ω

$$\omega = -\frac{\partial \phi}{\partial t} = \text{constant}. \tag{2.30}$$

The phase, ϕ, propagates with the wave vector (which is a one-form and not a true vector) as $k_i = \nabla_i \phi$ or $\boldsymbol{k} = \boldsymbol{\nabla}\phi$ and has the following structure

$$\phi = \phi(\boldsymbol{r}) - \omega t, \tag{2.31}$$

where

$$\phi_0 = \int \boldsymbol{k} \cdot \mathrm{d}\boldsymbol{r}. \tag{2.32}$$

The modulus of $\boldsymbol{k}$ is k which relates to the familiar wavelength, λ, and period T via $\lambda = 2\pi/k$ and $T = 2\pi/\omega$, respectively. Noting, via the dispersion equation [9] for an

isotropic media,

$$\omega = \frac{ck}{n} \tag{2.33}$$

it is apparent that k depends on the optical properties of the media through which the electromagnetic wave is traveling, and that when said media varies so must k. With that in mind the more familiar conditional for GO to be a good approximation is framed as

$$|\nabla \lambda_m| \ll 1, \tag{2.34}$$

where λ_m is the wavelength in a medium. What (2.34) actually means can be described as follows. Limiting the plane wave propagation to two dimensions in a Cartesian space (2.34) expands as

$$|\nabla \lambda_m| = \sqrt{\left(\frac{\partial \lambda_m}{\partial x}\right)^2 + \left(\frac{\partial \lambda_m}{\partial y}\right)^2 + \left(\frac{\partial \lambda_m}{\partial z}\right)^2} \ll 1. \tag{2.35}$$

Then assuming that the material that the plane wave is traveling through is both isotropic and only varying in the X-direction, (2.35) is recast as

$$\frac{\partial \lambda_m}{\partial x} \ll 1, \tag{2.36}$$

which implies that

$$\partial \lambda_m \ll \partial x, \tag{2.37}$$

meaning that the wavelength in the medium must vary much less than the length over which it is traversing. As curved surfaces are of interest in this thesis it is worth investigating how curvature (namely scalar curvature, R (see Appendix)) manifests itself in terms of a GO conditional. Starting from (2.27), Leonhardt and Philbin [1] provide the following conditional which can be regarded as an expansion of (2.34)

$$|R_{ij}|\, \lambda_m^2 \ll 1, \tag{2.38}$$

where because the Ricci tensor, R_{ij}, is constructed from second order partial derivatives of the metric, and in turn has units of an inverse square length (in Cartesian coordinates), λ_m must appear as λ_m^2 to account for this. Restricting (2.38) to two-dimensional manifolds (surfaces) and noting that λ_m is a scalar, it implies

$$\lambda_m \ll \frac{1}{\sqrt{|R|}}, \tag{2.39}$$

which means that the GO approximation is not valid for surfaces that have sharp (relative to λ_m) corners, cusps or points. This is a feature that will be demonstrated in Chapter 3 through the study of a conic surface deformation. Moreover, a step-by-step example of how (2.38) is used to solve a real world problem can be found in the 'Simulations' section of Chapter 3. Therefore, (2.34) and (2.38) are the basic conditionals of the GO, and because they are invariant under coordinate transformations, it means that if GO is valid in the virtual space, it is also valid in the physical space.

Implementing the conditionals mentioned above, and assuming that the electromagnetic wave has the structure stated in (2.29), (2.27) appears as

$$\nabla^j \nabla_j E_i = \nabla^j \mathrm{e}^{i\phi} \left(\nabla_j \mathcal{E}_i + i k_j \mathcal{E}_i \right), \tag{2.40}$$

which after manipulation, takes on the form

$$\frac{\partial^2 E_i}{\partial t^2} = \mathrm{e}^{i\phi} \left(\frac{\partial^2 \mathcal{E}_i}{\partial t^2} - 2i\omega \frac{\partial \mathcal{E}_i}{\partial t} - \omega^2 \mathcal{E}_i \right). \tag{2.41}$$

In (2.41), the primary contribution comes from the final term $\omega^2 \mathcal{E}_i$, as a result of the fact that ϕ and $k_j k^j$ are the most rapidly varying features of the electromagnetic wave. Next, by requiring that wave equation (2.26) be satisfied for all amplitudes of $\mathcal{E}^i$ as is done in [1], one obtains the dispersion relation

$$k^j k_j = \frac{\omega^2}{c^2}, \tag{2.42}$$

which can be recast in terms of the metric tensor of the geometry as

$$g^{ij} k_i k_j = \frac{\omega^2}{c^2}. \tag{2.43}$$

Using the previously found relation of $\boldsymbol{g} = (\det \boldsymbol{\varepsilon})\, \boldsymbol{\varepsilon}^{-1}$ and (2.15) the following is obtained

$$\omega^2 = c^2 \boldsymbol{k} \cdot \boldsymbol{n}^2 \boldsymbol{k}, \tag{2.44}$$

which is the same as the formula for the refractive index in an anisotropic impedance-matched in [9].

Finally, starting with the empty-space Maxwell's equations in arbitrary coordinates

$$\frac{1}{\sqrt{g}}\left(\sqrt{g}E^i\right)_{,i} = \frac{\rho}{\varepsilon_0}, \tag{2.45a}$$

$$\epsilon^{ijk}H_{k,j} = \varepsilon_0\frac{\partial E^i}{\partial t} + j^i, \tag{2.45b}$$

$$\epsilon^{ijk}E_{k,j} = -\mu_0\frac{\partial H^i}{\partial t}, \tag{2.45c}$$

$$\frac{1}{\sqrt{g}}\left(\sqrt{g}H^i\right)_{,i} = 0, \tag{2.45d}$$

and letting $E = \mathcal{E}_i e^{i\phi}$ and $H = \mathcal{H}_i e^{i\phi}$, and assuming no charges and currents, as well as ignoring the derivatives of both the metric and field amplitudes $\mathcal{E}$ and $\mathcal{H}$ as they are negligible in comparison to the derivatives of the phase ϕ, results in (2.45) taking on the sought after geometrical optics approximation of Maxwell's equations:

$$k_i\mathcal{E}^i = 0, \tag{2.46a}$$

$$\epsilon^{ijk}k_j\mathcal{H}_k = -\omega\varepsilon_0\mathcal{E}^i, \tag{2.46b}$$

$$k_i\mathcal{H}^i = 0, \tag{2.46c}$$

$$\epsilon^{ijk}k_j\mathcal{E}_k = \omega\mu_0\mathcal{H}^i, \tag{2.46d}$$

where propagation in a media is described, and not just a vacuum. The wave vector, $\boldsymbol{k}$, plays a critical role in understanding what is stated in (2.46) and though it only appears in as a one-form in (2.46) it is important to keep in mind that $\boldsymbol{k}$ is in fact two distinct geometrical objects. First, as mentioned before, k_i is a one-form that represents the gradient of the phase ϕ, but k^i represents the ray direction and is in fact a propagation vector. These two objects are related by

$$k^i = g^{ij}k_j, \tag{2.47}$$

which is a general relation between a vector and a one-form. Put in a more a physical context, k^i is tangent to the light rays, but it is not equal to k_i, which means that in an anisotropic media (and its effective geometry) the light rays are not orthogonal to the phase surfaces, unlike the case in isotropic media. With that being said, it is important to note the index positions as they relate to the fields in (2.46). Equations (2.46a) and (2.46c) state that the field amplitudes are orthogonal to the wave vector k_i, but keeping in mind the constitutive relations ($D^i = \varepsilon_0\varepsilon^{ij}E^j$ and $B^i = \mu_0\mu^{ij}H_j$, $k_i\mathcal{E}^i$) and $k_i\mathcal{H}^i$ refer to $\underline{D}$ and $\underline{B}$, respectively and not $\underline{E}$ and $\underline{H}$. Through lowering the indices of the fields in (2.46a) and (2.46c), and in turn raising them in the kernal k, it can be shown that $\underline{E}$ and $\underline{H}$ are orthogonal to k^i. Collectively this means that in an

anisotropic media, $\underline{D}$ is orthogonal to k_i and $\underline{H}$, and $\underline{B}$ is orthogonal to $\underline{E}$ and k_i. It is only in isotropic media (where the effective geometry is conformally flat) that the more familiar relations exist where $\underline{E}$ is orthogonal to $\underline{H}$, $\underline{D}$ points in the same direction as $\underline{E}$ and $\underline{B}$ points in the same direction as $\underline{H}$. Of course other expressions such as the total energy density and energy flux can be derived in the regime of GO using (2.46) as a starting point, as is done in [1], but their utility falls outside the scope of this introduction.

In conclusion, in this section the key aspects TO are introduced. Starting from the empty-space Maxwell's equations in Cartesian coordinates, and then casting them in an empty curved space, their equivalence (via a scaling factor and constitutive relation) to the macroscopic Maxwell's equations in a dielectric media is derived. This then allows for the discussion of virtual and physical spaces, as well as the idea of a spatial transformation media (a media which effectively performs a coordinate transformation between said spaces). Noting that in some instances it may be advantageous to describe the virtual space and physical space with different coordinate systems, the transformation tensor is included in the solution for the transformation media as well, thereby providing a truly generalized method. Later, geometrical optics is introduced and the required conditionals needed to make it a good approximation to the wave equation are noted. Then, the importance of the wave vector is studied and Maxwell's equations in the regime of geometric optics are derived. Finally, how the transformation media appears under the geometrical optics approximation is studied.

2.3 Non-Euclidean geometries

The idea of non-Euclidean geometries relates to the idea of spaces (either virtual or physical) in TO. What follows is a general introduction to what is meant by the term 'non-Euclidean' in the context of this thesis. Here a geometry is, as is the accepted mathematical definition [11], a complete, locally homogeneous, Riemannian manifold. A Euclidean geometry is a geometry that follows Euclid's fifth or parallel postulate [12] which can be phrased as, 'Given any straight line and a point not on it, there exists one and only one straight line which passes through that point and never intersects the first line, no matter how far they are extended.'

Noting that only two-dimensional manifolds [13] (mathematical objects that can be regarded as surfaces) are discussed in this thesis, perhaps a better way to discuss Euclid's fifth postulate is in relation to collections of lines (e.g. a triangle) on said geometries and not just how lines behave with respect to a common perpendicular. For example, it is well known that the summation of interior angles of a triangle on a Euclidean geometry (e.g. a flat plane) is equal to $\pi/2$. However, something interesting

occurs when a triangle is constructed on a non-Euclidean geometry which is a geometry that does not follow the parallel line postulate in either one of two ways. In the case of hyperbolic geometries [14] (sometimes referred to as Lobachevskii geometries), the aforementioned parallel lines effectively 'curve' away from one another (often called ultraparallels) with increasing distance as they move away from the common perpendicular. A triangle constructed on such a geometry would have a summation of interior angles less than $\pi/2$, and by extension, a quadrilateral (as it is composed of two triangles) would have a summation of interior angles less than π. A local partial model of a hyperbolic geometry is a psuedosphere [15]. The second type of non-Euclidean geometry is of the elliptic [16] variety where the parallel lines 'curve' towards one another and eventually intersect. This feature manifests itself in triangles and quadrilaterals whose summation of interior angles are greater than $\pi/2$ and π, respectively. A local partial model of an elliptic geometry is a sphere. Having reviewed the very basics of non-Euclidean geometries, and how they manifest themselves in familiar polygons, their relation to TO is now explained.

In the previous examples, the summation of interior angles of triangles on different geometries was used as a means of explaining some intrinsic properties of the geometries themselves. What is ultimately of interest, however, regarding these geometries are the length minimizing paths between points on them (i.e. geodesics). Interest in non-Euclidean geometries, at least in this thesis, is a result of the fact that light travels along geodesics (both material and spatial) [1] and depending upon what space/geometry the light is propagating along will influence its path. Lastly, as this thesis is focused with the manipulation of light confined to surfaces of non-zero curvature it is important to clarify what is meant by 'curvature.' In this thesis, when discussing curvature what is being commented on is the Gaussian curvature [3], which in a very general form is defined as

$$K = K\left(\boldsymbol{x}; \boldsymbol{U}, \boldsymbol{V}\right) = \frac{R_{ijkl} U^i V^j U^k V^l}{G_{pqrs} U^p V^q U^r V^s}, \tag{2.48}$$

where

$$G_{pqrs} \equiv g_{pr} g_{qs} - g_{ps} g_{qr} \tag{2.49}$$

and $\boldsymbol{U} = U^i$ and $\boldsymbol{V} = V^i$ are contravariant vectors. Worth noting, is that the Gaussian curvature is related to the scalar curvature by $R = 2K$. Now, according to (2.48) K depends not only on position ($\boldsymbol{x}$), but also on a pair of directions selected at each point (the vectors $\boldsymbol{U}$ and $\boldsymbol{V}$), which is different than the traditional notion of scalar curvature on a two-dimensional manifold that would only depend on the points in space. The reason for this is that to limit the idea of curvature simply to points in space for higher dimensional manifolds would be severely limiting (a discussion that falls outside of the

domain of this thesis), but it will be shown below that assuming that a two-dimensional manifold ($n = 2$) is under study (as is the case throughout this thesis), (2.48) is purely point specific as anticipated. First, the Riemann tensor of the first kind is defined by

$$R_{ijkl} = \frac{\partial \Gamma_{jli}}{\partial x^k} - \frac{\partial \Gamma_{jki}}{\partial x^l} + \Gamma_{ilr}\Gamma^r_{jk} - \Gamma_{ikr}\Gamma^r_{jl}, \tag{2.50}$$

and by letting $n = 2$ it can be shown that only non-zero components of R_{ijkl} are

$$R_{1212} = R_{2121} = -R_{1221} = -R_{2112}. \tag{2.51}$$

This implies that for $n = 2$,

$$\begin{aligned} K &= \frac{R_{ijkl}U^iV^jU^kV^l}{G_{pqrs}U^pV^qU^rV^s} \\ &= \frac{R_{1212}\left[\left(U^1\right)^2\left(V^2\right)^2 - 2U^1V^2U^2V^1 + \left(U^2\right)^2\left(V^1\right)^2\right]}{G_{1212}\left[\left(U^1\right)^2\left(V^2\right)^2 - 2U^1V^2U^2V^1 + \left(U^2\right)^2\left(V^1\right)^2\right]} \\ &= \frac{R_{1212}}{G_{1212}} = \frac{R_{1212}}{g_{11}g_{22} - \left(g_{12}\right)^2}, \end{aligned} \tag{2.52}$$

where R_{1212} can then be calculated directly via

$$\begin{aligned} R_{1212} = \frac{1}{2}\left(\frac{\partial^2 g_{12}}{\partial x^2 \partial x^1} + \frac{\partial^2 g_{21}}{\partial x^1 \partial x^2} - \frac{\partial^2 g_{11}}{\partial x^2 \partial x^2} - \frac{\partial^2 g_{22}}{\partial x^1 \partial x^1}\right) \\ + \Gamma_{121}\Gamma^1_{21} - \Gamma_{111}\Gamma^1_{22} + \Gamma_{122}\Gamma^2_{21} - \Gamma_{112}\Gamma^2_{22}. \end{aligned} \tag{2.53}$$

The Γ terms (Christoffel symbols) can be solved by

$$\Gamma^i_{jk} = g^{ir}\Gamma_{jkr}, \tag{2.54}$$

and

$$\Gamma_{ijk} = \frac{1}{2}\left(\frac{\partial g_{jk}}{\partial x^i} + \frac{\partial g_{ki}}{\partial x^j} - \frac{\partial g_{ij}}{\partial x^k}\right). \tag{2.55}$$

Recasting (2.53) in Cartesian coordinates

$$\begin{aligned} R_{1212} = \frac{1}{2}\left(\frac{\partial^2 g_{12}}{\partial y \partial x} + \frac{\partial^2 g_{21}}{\partial x \partial y} - \frac{\partial^2 g_{11}}{\partial y^2} - \frac{\partial^2 g_{22}}{\partial x^2}\right) \\ + \Gamma_{121}\Gamma^1_{21} - \Gamma_{111}\Gamma^1_{22} + \Gamma_{122}\Gamma^2_{21} - \Gamma_{112}\Gamma^2_{22}, \end{aligned} \tag{2.56}$$

it is possible to directly solve for Riemann tensor of the first kind, and in turn the desired Gaussian curvature, K, which as anticipated is purely a function of a point in space. More detail is provided in the introduction of each chapter detailing how non-Euclidean

surfaces, and their curvature, play a role in the proposed TO approaches. With that being said, a literature review of the field of transformation electromagnetic/optics is now presented.

2.4 A literature review of TO

2.4.1 Founding theoretical works

The underlying idea behind transformation optics (TO) was first proposed by Pendry *et al.* [17] and independently by Leonhardt [18]. Both works make an appeal to the form invariance of Maxwell's equations under coordinate transformations to control electromagnetic (EM) waves by altering the EM properties (i.e. ε_{ij} and μ_{ij}) of the media through which they travel, the fundamentals of which (focusing on Leonhardt's approach) were detailed earlier in this chapter. In [17] Pendry *et al.* utilized the consistent displacement of the electric displacement $\underline{D}$, magnetic flux density $\underline{B}$ and Poynting vector $\underline{S}$ via a coordinate transformation technique to configure electromagnetic fields into nearly any arrangement. Said coordinate transformation technique ensure that the proscribed material properties (ε_{ij} and μ_{ij}) of the space of interest satisfy Maxwell's equations, and leads to the idea of a 'transformation media'. A thorough mathematical explanation of this derivation can be found in the supplemental materials section of [17]. This work is highly important not only because it provided an elegant method for manipulating EM fields, but also because it exposed the greater physics and electrical engineering community to the idea of cloaking and more exotic lens designs. The same can be said for Leonhardt's seminal work [18], and the derivations found therein constitutes the majority of the work found in the previous section. These two works ([17] and [18]) form the theoretical foundation upon which the majority of TO is built.

Another informative theoretical work by Leonhardt *et al.* [19] focused on explaining the link between general relativity (where the form invariance of Maxwell's equations had been utilized for decades) and electrical engineering, which aided in exposing the those outside of the theoretical physics community (namely, electrical engineers) to the basic ideas of TO. The idea of coordinate transformations also grabbed the attention of those entirely outside of the electromagnetics community and lead to the design of heat cloaks/concentrators [20, 21], acoustic cloaks [22, 23], elasto-mechanical cloaks [24, 25], fluid flow cloaks [26, 27] and even multiphysics cloaks [28, 29]. Returning back to electromagnetics community, and what arguably constitutes the bulk of research in TO community, are efforts that focus more upon design methodologies which are then utilized to design devices (e.g. cloaks, lenses, surface overlays, etc.), and a summary,

though by no means exhaustive, of such works is provided below. Here it is important to emphasis that the order in which publications appear within each paragraph (segmented yearly) is in no way related to the time of the year in which they were published - their ordering is arbitrary. Also, works that focus explicitly on TO as it relates to surface waves will be introduced and reviewed at the beginning of chapters that they are particularly relevant to.

2.4.2 A chronological review of TO

Since its founding in 2006, TO has been an ever-expanding field of study spanning fundamental theory, numerical modeling, device fabrication and experimental validation. Owing to the sheer breadth of the field, it is perhaps simplest to discuss TO in a chronological fashion. The review starts with the founding works [17, 18] which have already been discussed. Soon after the publications of these works (still in 2006), early design techniques including material property calculations [30] needed for the design of a 2D metamaterial cloak at microwave frequencies [31], were proposed by Schurig *et al.*. The experimentally validated design put fourth in [31] had a number of shortcomings, but perhaps most limiting was its inherent reliance on the resonant properties of the metamaterials themselves (which lead to the narrow-band performance). The year after, in 2007, Kong *et al.* [32] demonstrated (via full-wave EM simulations) the use of coordinate transformations to design novel planar antennas.

Two years after the first experimental validation of a cloaking device [30] (2008), the fundamental idea of cloaking was reworked by Li et al. [33] by making a surface deformation on a flat conducting ground plane appear, electrically speaking, flat to an incident space wave via a carpet cloak. This work was very important because it had the advantage, compared to the previous 2D metmaterial cloak [31], of having non-singular material properties, which allowed for an isotropic material realization. Furthermore, this technique made the possibility of obtaining a broadband cloak a realistic prospect. This same year, Ochiai and Leonhardt [34] proposed a dielectric invisibility cloak based on negative refraction and optical conformal mapping where the time-delay present in other free-space cloaks was reduced to zero.

In 2009 a number of new and interesting ideas were developed in the field of TO. Kwon *et al.* [35] developed (and validated via full-wave simulations) a technique to scan beams on flat surfaces using TO. Also during this year, Liu et al. [36] used TO to design and later experimentally demonstrate a broad band ground-plane cloak (carpet cloak) while Valentine *et al.* [37] designed, via quasi-conformal TO, and experimentally demonstrate the first ever optical carpet cloak. This was a particularly important advancement because it was the first demonstration of optical cloaking, whereas previous

efforts had focused in the microwave regime. Hao and Mittra [38] also published a book this same year that detailed the FDTD modeling of metamaterials and it would go on to serve as a reference text for those trying to model the devices borne out of TO. In 2009 Lai *et al.* [39] proposed the idea of illusion optics where TO was used to make an object appear, electrically speaking, as if it where another object. This work was important in the sense that it recasted the idea of cloaking as a special form of an illusion device. Also, the idea of a complimentary media invisibility cloak was proposed (and validated via full-wave simulations) by Lai *et al.* [40] were objects outside the cloak itself were hidden. Lastly in 2009, an entirely different approach to cloaking was developed by Vasquez *et al.* [41] where it was demonstrated via full-wave simualations, that three or more active devices could create a 'quiet zone' between them where an object placed in said zone would become virtually invisible.

The following year, in 2010, Leonhardt and Philbin published a monograph [1] on the topic of TO which has been a reference for researchers in the field ever since. Also, this same year, expanding on the illusion concept proposed in [39], Chen *et al.* [42] through the use of TO developed (and validate via full-wave simulations) a device that could simultaneously cloak an object and generate illusion images. During the same time, Huidoboro *et al.* [43] modified TO to control surface plasmon polaritons (SPPs) where three examples were put forward to demonstrate the efficacy of the method: a beam shifter, a cylindrical cloak and a ground-plane cloak. A similar use of TO to control SPPs was also examined by Kadic *et al.* [44] this same year, and sample devices were detailed. An appreciable contribution to the engineering side of TO came from Tang *et al.* [45] in 2010, where a discrete coordinate transformation technique was proposed (and validated via full-wave simulations) which allowed for the creation of all-dielectric flat antennas among other devices [46, 47]. Zheng *et al.* [48], following on from the work done by Vasquez *et al.* [41], demonstrated how active sources could be used to create illusion devices as well. Finally, also in 2010, Ozgun and Kuzuoglu [49] provided a comprehensive review of the state of TO (as well as devices borne out of it) and how it had evolved since its inception in 2006.

In 2011 a growing number of publications, compared to previous years, focused on the engineering/practical side of TO. Argyropoulos *et al.* [50] studied the transient response (via an FDTD technique) of previously proposed cloaks and concentrators and drew new conclusions regarding the bandwidth performance of said devices. This work would later serve as a guide for the practical implementation of devices borne out of TO. Also, in 2011, Selvanayagam *et al.* [51] proposed (and validated via a full-wave simulations) a lattice of skewed transmission lines to implement a full effective material tensor. This work was important because it demonstrated how the anisotropic effective medium called for by a pure implementation of TO could in fact be realized in three

dimensions. This same year Yang *et al.* demonstrated a broadband zone plate lens [52] and a broadband beam-steerable flat reflector [53], both of which used a discretized version of TO [46], and by consequence were purely dielectric. The final publication from 2011 that is commented on is that of Chen *et al.* [54] which describes what is referred to as a macroscopic invisibility cloak (of the ground-plane variety) for visible light. In this work the fabrication of a macroscopic volumetric cloak (constructed from birefringent crystals) is described and it is experimentally demonstrated that for a specific light polarization, three dimensional objects (of the scale of a centimeters and millimeters), can be cloaked from visible light.

In terms of research output, 2012 was similar to 2011 in the sense that a lot of efforts focused on the design of realizable novel devices. For example, Wu *et al.* [55] designed (via quasi-confromal TO) and validated via full-wave simulations, an all-dielectric, broadband, low-loss collimating lens that could radiate multiple directive beams when fed by a simple line source. Similarly, making an appeal to a conformal transformation Aganejad *et al.* [56] proposed and numerically validated an isotropic graded index lens that when placed in a horn antenna produced a highly directive beam with low sidelobes. Also this same year, Kwon [57] expanded the use quasi-conformal TO to lenses on conformal arrays to enable new scanning capabilities. Tang *et al.* [58] expanded (and numerically validated) upon the idea of the carpet cloak [33] by effectively modifying it as a novel lens that created a highly directive beam for an antenna that was placed beneath it. Focusing instead on the manipulation of magnetic fields, Navau *et al.* [59] used TO to create a magnetic shell that could harvest magnetic energy and distribute it as desired which had clear applications in the wireless transmission of energy. Lastly, Zhu *et al.* [60] utilized a linear coordinate transformations that resulted in the creation of materially homogeneous plasmonic devices such as cloaks and concentrators whose performances were validated in finite-element simulations.

In 2013, a number of important works were published including a book by Werner *et al.* [61] summarizing to date the field of TO as well as their material realization via metamaterials. This same year, Shen *et al.* [62] proposed and experimentally validated the concept of conformal surface plasmons (CSPs) for use in the microwave regime which appeared as a flexible sub-wavelength film that could be folded, bent and twisted to control the flow of CSPs. Also, in 2013 Li *et al.* [63] proposed (and validated via full-wave simulations) the use of homogeneous materials (in both anisotropic and isotropic forms) to create an illusion devices (in both 2D and 3D) that, electrically speaking, shrunk an object. This work is noted because not only did it further expand the application of TO, it also provided a material recipe for building a realizable device. In the same year, Wu *et al.* [64] provided a systematic comparison (via full-wave simulation) between two different TO design approaches (linear geometrical

transformations and quasi-conformal mapping) for a quad-beam focusing lens, where the advantages and disadvantages of each method were clearly identified. Finally, in 2013, Ma *et al.* [65] experimentally validated for the first time, active cloaking and illusion devices for DC electricity.

The following year, in 2014, Kraft *et al.* [66] used TO as a mathematical tool to identify symmetries (electrically speaking) among apparently asymmetric structures such as an ellipse/spheroid. Also on the theoretical side of TO, Kinsler *et al.* [67] expanded the theory of a space-time cloak into that of the carpet or ground-plane cloak. In the same year, Ginis *et al.* [68] demonstrated how TO can be applied to to create a specific kind of metamaterial which could be used to control Cherenkov radiation. Also, Oliveri *et al.* [69] proposed and validated (via full-wave simulations) a generalized quasi-conformal TO design methodology which allowed for an arbitrary physical antenna array arrangement, coated with a appropriate lens, to emulate the radiating features of an arbitrary reference virtual antenna array in free space. Another practical application of TO came from Mateo-Segura *et al.* [70] where a flat all-dielectric Luneburg lens was designed, simulated and experimentally validated. Lastly, in 2014, Horsley *et al.* [71] proposed and validated via full-wave simulations a means of removing singular refractive indices, produced during the TO design process, from surface wave devices by replacing them with an equivalent sculpted surface.

Thus far in 2015 (the year this thesis was written), there seems to be an even mix of interest in the theoretical underpinnings of TO [17, 18], and device realization. First, Xu and Chen [72] provided a review of conformal transformation optics upto the end of December 2014, and this has served as a good starting point for those not familiar with the design technique. Kraft *et al.* [73] have used TO to deign plasmonic gratings that support both localized and propagating plasmons which has applications in the fields of optical biosensing as well as solar cell design. Also focusing on the application front of TO, are Junqueira *et al.* [74] who compared different anisotropy reduction schemes typical employed within TO (e.g. conformal and quasi-conformal mappings) which could be used as a design tool for other devices borne out of TO. Lastly, there have been two publications that investigate space-time TO, instead of the traditional spatial TO. The first is by Boston [75] where a derivation of the required permeability, permittivity, and magnetoelectric couplings for light in the media to follow a closed geodesics (thereby theoretically permitting time travel). The second is by Thompson *et al.* [76] who also proposes a space-time cloak, but uses it as a means to enhance the conceptual understanding of spatial TO, which would in turn hopefully allow for increased functionality of the theory. Thus, having provided a brief chronological overview of TO since its inception, three works that provide some motivation for this thesis are introduced below.

2.4.3 Non-Euclidean TO

In recent years there have been a number of attempts to couple the ideas of non-Euclidean geometries and TO as they apply to space waves. Perhaps the most well known and first of these efforts was by Leonhardt and Tyc [77], where they proposed the use of a curved non-Euclidean space (in their case a sphere) to ease the material parameters traditionally called for by such free-space cloaks, and in turn create a broadband cloaking device. In this work, the authors note the primary limiting factor of traditional cloaking via a transformation media (i.e. superluminal travel by light inside of the proposed device), and put forward the idea of using instead curved spaces where light may 'propagate along closed loops or may avoid some regions altogether.' This method relies on the use of branch cuts, and other techniques that fall outside the immediate domain of this thesis, but an excellent summary of the mathematical underpinning of the theory itself can be found in the supplemental material section of [77]. That being said, [77] acts, in relation to this thesis, as a motivation for looking more closely into non-Euclidean geometries in general as they relate to TO.

A later work which offers full-wave simulation results of the devices proposed in [77] was carried out by Tyc *et al.* [78]. Here the authors explore, both analytically and numerically, the full wave propagation of a two-dimensional cloak proposed in [77]. In doing so, it is demonstrated (via full-wave EM simulation) that the device works perfectly in the limit of geometrical optics (as was expected in [77]), but possess some imperfections (in the form of diffraction and phase delay) when operating below the optical limit. The authors point out that this behavior is to be expected from a technique borne out of GO and such imperfections can be made arbitrarily small by increasing the frequency of the incident field. Finally, Tyc *et al.* [78] mention that though the device does not work perfectly for light waves, this does not diminish its value, as it is ultimately realizable (does not call for material with singular properties). As it relates to this thesis Tyc *et al.* [78], provides a solid reference for the full-wave modeling of non-Euclidean devices (though they are fundamentally still flat ($K = 0$) surfaces in [78]), as well as the idea of taking into account the 'optical limit' of a TO device.

Lastly, a work involving the use of a non-Euclidean transformation is by Yao *et al.* [79]. Here the authors propose a thin collimating metamaterial in the shape of a hyperbolic lens with a point source embedded in its perimeter. The proposed method successively transforms (via stereographic projection) spherical wave-fronts (in the virtual space) into planar wave fronts (in the physical space), which gives rise to the profile and material loading of the sought after lens. It is clear that the authors of [79] are aware of the necessity of their device to operate within the optical limit, which

explains why, at its lowest frequency of interest ($f = 2.5$ GHz), it is electrically large (calling for a diameter of approximately $17\lambda_0$ and a central thickness of $4.2\lambda_0$). This work, also places an emphasis on realizability in that the material parameters called for by the technique are non-singular. In an attempt to scale down the size of the lens, the authors offer two methods. The first involves using a translational planes, in the definition of stereographic projections, and the second, the use of a bispherical coordinates to describe the virtual space (spherical wave fronts). Beyond its application to non-Euclidean transformations, the work of Yao *et al.* [79] is worth noting because it provides a practical implementation of TO, though once again focused on space waves and not surface waves.

In summary, a number of efforts, owing to inherent physical limitations of techniques proposed in the early stages of TO, have focused on the use of non-Euclidean geometries [77–79]. Through treating the spaces of interest as non-Euclidean geometries, it was demonstrated that the material singularities that plagued earlier designs could be avoided. That being said, all of the devices mentioned in [77–79] are materially anisotropic which does limit there immediate usage from an applications perspective.

2.5 Conclusions

In this chapter a number of key ideas were introduced and explained. First, the fundamentals of transformation optics (TO) were investigated. To start, the empty-space Maxwell's equations in an arbitrary coordinate system were presented and their equivalence (via scaling and constitutive relations) to the media-filled macroscopic Maxwell's equations in a Cartesian coordinate system were derived. This formed the basis of what is known as a spatial transformation media which performs a coordinate transformation between the virtual and physical spaces. Also throughout said derivation, there was a focus on understanding the wave propagation in both isotropic and anisotropic media, and when appreciable differences appeared (e.g. via the constitutive relations between electric field strength and dielectric displacement), they were examined. Finally the geometrical optics (GO) approximation was introduced and the conditionals required for it be a good approximation of the wave equation were studied. Finally, Maxwell's equations were rewritten in the limits of GO and an examination of the wave vector as it related to the dielectric properties of an anisotropic media (or conversely a curved space) was studied.

Next, a brief introduction to non-Euclidean geometries as they appear in this thesis, was presented. Here the fundamental differences between Euclidean and non-Euclidean geometries, in their broadest sense, were detailed. As the majority of this thesis focuses on intrinsically two-dimensional manifolds (surfaces), a suitable parameter (Gaussian

curvature, K) was put forth that clearly demonstrated the type of surface under investigation.

Finally, a literature review of TO was conducted. First, the founding theoretical works were examined and the impact of coordinate transformations espoused by TO were noted in fields well outside the traditional influences of electromagnetics. Next, a yearly-segmented chronological literature review (starting in 2006 and ending in mid-2015) was presented and the role of TO in, but not limited to, fundamental theory, numerical modeling, device design and experimental validation was examined. Also during this review extra commentary was included on works that were particularly novel and influential. The literature review was concluded with an examination of three works that make an appeal to non-Euclidean geometries, but all with a focus on space waves and not surface waves.

Chapter 3

Rotationally symmetric surface wave cloaks

3.1 Introduction

The idea of cloaking an object has been at the center of interest in transformation optics (TO) for quite some time, but mostly for objects in three dimensional free-space [17, 18, 31, 33, 36, 37, 48, 54, 77]. However, recently a number of researchers have been trying to manipulate electromagnetic waves that are bound to two-dimensional surfaces: surface waves. One of the first to use TO as a tool to control the flow of surface plasmon polaritons (surface waves propagating along a metal-dielectric interface with a field distribution that is evanescent in the direction perpendicular to the interface) was done by Huidobro *et al.* [43], and at the same time independently by Liu *et al.* [80] where the use of quasi-conformal mapping was also studied. In both these works, it was shown, among other things, that a surface deformation can effectively be 'cloaked' from an incident surface wave using the tools provided by TO. However, the transformation media (overlay) itself proposed in both [43] and [80] are electrically large which is a drawback from an engineering perspective where the space occupied by any such cloak would want to be minimized. Focusing again on realizability, the cloaking medium proposed in [43] required a metamaterial implementation due to its exotic material requirements (inherent anisotropy), whereas the design proposed in [80] can be realized in a purely dielectric form (via a quasi-conformal mapping solution). Worth highlighting is the fact that the surface deformations studied in [43] are finite in three-dimensions whereas they are effectively infinite in one of the dimensions in the case of [80]. Another effort that expands upon the work in [43] is that of Huidobro *et al.* [81] where conformal and quasi-conformal mappings (similar to what was done by Liu *et al.* [80]) are used to engineer refractive index films to coat metallic surface

deformations. Here again however, a deformation that is effectively infinite in one of the three-dimensions is studied. Also worth noting is that the previous three works [43, 80, 81] focus on light at optical wavelengths. The efforts of Huidobro *et al.* [43, 81] and Liu *et al.* [80] along with the works of Kadic *et al.* [44, 82], Zhu *et al.* [60] and Yang *et al.* [83] constitute the main efforts involving the use of TO to control surface waves (often referred to as transformation plasmonics) that are most closely related to the work found in this chapter.

In this chapter a new method, utilizing Fermat's principle, is used to create an omnidirectional, purely dielectric, electrically thin material overlay that can cloak a finite, curved (i.e. non-Euclidean) surface deformation from surface waves in the microwave regime. First, its derivation, starting with Fermat's principle, is produced and a number of sample surfaces are studied. Next, a numerical solution is derived to account for any limitations, found in the analytical approach. Afterwards, the performance of three distinct surface waves cloaks are analyzed (via full-wave electromagnetic (EM) simulations). Finally, a realizable surface wave cloak is designed, modeled, and validated via full-wave EM simulation.

3.2 Analytical solutions for cloaking surface deformations

To start, a coordinate invariant definition of optical path length, S, in an isotropic medium in $\mathbb{R}^2$ is put forward in

$$S = \int_a^b n(x^1)\,\mathrm{d}S, \tag{3.1}$$

where a, b and $\mathrm{d}S$ represent, two different points along $\mathbb{R}$ and the line element, respectively. The reason for this particular form of the optical path length is as follows. For simplicity, and underlying mathematical considerations, this formalism is focused on studying surface deformations whose rotational profiles, regarded as space curves, $\gamma(x^1) \in \mathbb{R}^2$, are a function of a single variable $x^1 \in \mathbb{R}$ which there also exists a one-to-one relationship between γ and x^1. From an applications point of view this means that the following formalism is only valid for designing rotationally symmetric surface wave cloaks. However, this is not to say that a further generalized form of this technique could not be derived to account for rotationally asymmetric surfaces, but the underlying elegance and ultimate 'ease-of-use' of the formalism would most likely be compromised in the process.

Moving on, the last piece of (3.1) that needs to be addressed is the line element, $\mathrm{d}S$ which is solely dependent upon the parameterization of the space curve γ, used to connect points a and b. If Cartesian coordinates (i.e. $x^1 = x$ and $x^2 = y$) are employed

then

$$\mathrm{d}S = \sqrt{1 + \left(\frac{\mathrm{d}y}{\mathrm{d}x}\right)^2}\,\mathrm{d}x, \tag{3.2}$$

whereas if spherical coordinates are employed (i.e. $x^1 = r$ and $x^2 = \theta$) then,

$$\mathrm{d}S = \sqrt{r^2 + \left(\frac{\mathrm{d}r}{\mathrm{d}\theta}\right)^2}\,\mathrm{d}\theta. \tag{3.3}$$

In short, the decision on the coordinate system employed to describe the profile of the surface deformation will dictate the parameterization of γ, and in turn the form of $\mathrm{d}S$. Ultimately, this decisions is arbitrary though certain profiles are less cumbersome to describe in certain coordinate systems, and it is advantageous to use the simplest method to parameterize γ whenever possible.

With a formalism for optical path length in (3.1) in place, it is now possible to properly address the problem of creating a rotationally symmetric surface wave cloak. In a very basic sense in order to cloak an object, at least in this context, the optical path length, S', in the curved space, must be the same as the optical path length, S, in the flat space. The space curves along which this equivalence must occur is represented by γ' and γ in Figure 3.1. With this in mind (3.1) can be applied as

$$S' = S \implies \int_{a'}^{b'} n'(x'^1)\,\mathrm{d}S' = \int_a^b n(x^1)\,\mathrm{d}S. \tag{3.4}$$

For surface wave cloaking applications, $n(x^1)$ is regarded as a constant (as it corresponds to the homogeneous refractive index of a flat plane) and (3.4) takes on the form

$$\int_{a'}^{b'} n'(x'^1)\,\mathrm{d}S' = n\int_a^b \mathrm{d}S. \tag{3.5}$$

Worth highlighting is that the solved for refractive index, n', in (3.5) will also be isotropic due to the fact that it is effectively the refractive index along a line (mathematically speaking it is nothing more than a scalar) and does not have a second dimension to 'be anisotropic about'. It is not until this refractive index is rotationally swept about the origin of a given surface deformation does it appear as a physical material tensor where, owing to the symmetry of the surface deformations, isotropy is once again preserved.

3.2.1 Hemispheric surface deformation

As a proof of concept, a hemispheric deformation surrounded by a flat approach plane is cloaked from a surface wave. Here the refractive index, n_c, of a hemispheric deformation is solved for in such a way that it appears as if it were, electrically speaking, a flat plane of uniform refractive index, n. Taking advantage of the spherical coordinate system, (3.5) takes on the form

$$\int_0^{\frac{\pi}{2}} n_c(\theta)\sqrt{(R(\theta))^2 + (R'(\theta))^2}\,\mathrm{d}\theta = n\int_0^R \mathrm{d}r, \tag{3.6}$$

where, $R(\theta)$ represents the length of a curve that starts at the origin and terminates on the surface of interest, θ is the traditional polar angle, and R is the radius of the hemisphere. Taking into account that $R(\theta) = R$ for a hemispheric deformation of radius R, (3.6) reduces to

$$R\int_0^{\frac{\pi}{2}} n_c(\theta)\,\mathrm{d}\theta = n\int_0^R \mathrm{d}r. \tag{3.7}$$

In order to solve for $n_c(\theta)$ one more equation aside from (3.7) is needed to effectively 'link' the two surfaces, and this appears via equating two different circular paths (α' and α in Figure 3.1), which are related via a simple projection of the curved surface onto the flat one. Mathematically speaking, the electrical path lengths along the circumference

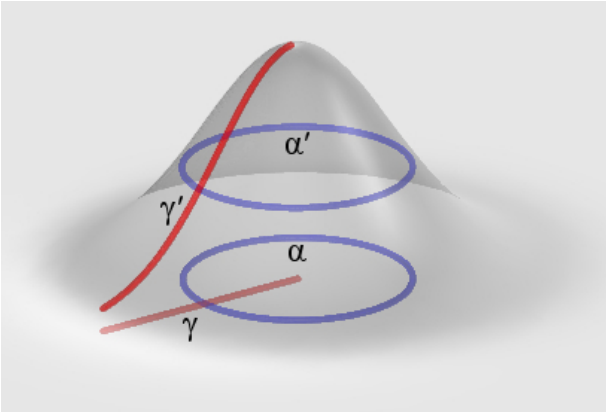

Figure 3.1: Space curves on a rotationally symmetric surface, and a flat surface. γ' and γ correspond to the left and right-hand sides, respectively, of (3.5) while α' and α correspond to the left and right-hand sides, respectively, of (3.8)

.

of a circle of arbitrary radius on the two surfaces is equated,

$$2\pi R\sin(\theta)n_c(\theta) = 2\pi r n, \tag{3.8}$$

where $R\sin(\theta)$ is how r is defined along the hemisphere. Simplifying (3.8), solving for r

$$r = \frac{1}{n}\left[R\sin(\theta)n_c(\theta)\right], \tag{3.9}$$

and noting that after implicit differentiation

$$\mathrm{d}r = \frac{R}{n}\left[\cos(\theta)n_c(\theta) + \sin(\theta)n_c'(\theta)\right]\mathrm{d}\theta, \tag{3.10}$$

it is possible to directly equate the integrands in (3.7) as

$$n_c(\theta)R\mathrm{d}\theta = n\left\{\frac{R}{n}\left[\cos(\theta)n_c(\theta) + \sin(\theta)n_c'(\theta)\right]\mathrm{d}\theta\right\}. \tag{3.11}$$

After a little manipulation, (3.11) is recast as

$$\frac{n_c'(\theta)}{n_c(\theta)} = \frac{1}{\sin(\theta)} - \frac{\cos(\theta)}{\sin(\theta)}, \tag{3.12}$$

which, using a well-known relation in calculus is equivalent to

$$\frac{\mathrm{d}}{\mathrm{d}\theta}\log\left(n_c(\theta)\right) = \frac{1}{\sin(\theta)} - \frac{\cos(\theta)}{\sin\theta}. \tag{3.13}$$

After performing the necessary integration the desired solution is found to be

$$n_c(\theta) = \frac{\tan\left(\frac{\theta}{2}\right)}{\sin(\theta)}. \tag{3.14}$$

Having solved for the correct refractive index distribution, n_c to cloak a hemispheric surface deformation from surface waves, a structure that is equally common place, but not as easily parametrically described is investigated: a conic surface.

3.2.2 Conic surface deformation

There are mainly two reasons for investigating a conic surface. First, and perhaps most importantly from a mathematical perspective, is to demonstrate that the proposed analytical solution is robust enough to be valid for surfaces other than a hemisphere. Secondly, and perhaps most importantly from an applications perspective, is that the proposed formalism does not explicitly account for surface wave backscattering issues (a problem that will become apparent in the simulation results for the hemispheric deformation found later in this chapter), introduced at the boundary of the approach plane and the hemisphere itself. At this interface, though there is a continuous refractive index ($n = 1$ in the above derivation), there is a rapid discontinuity in the Gaussian

curvature between the flat approach plane ($K = 0$) and the hemisphere ($K = 1/R^2$). This curvature mismatch occurs at every point along the edge of the hemisphere and leads to the surface wave being scattered back in the direction from which it came. In order to solve for this problem, it is necessary to reduce this mismatch as much as possible and perhaps the simplest surface that allows for the control of this curvature discontinuity whilst still imposing a rotational symmetry on the surface itself is in the form of a conic surface deformation.

First, a cone of height, b along the Z-axis and a radius of a in the XY-plane is constructed. Setting $z = R\cos(\theta)$ and $x = R\sin(\theta)$ it is possible to express $R(\theta)$ as

$$R(\theta) = \frac{b}{\cos(\theta) + \frac{b}{a}\sin(\theta)}. \tag{3.15}$$

This is an important feature of this surface deformation, because unlike in (3.8), R varies as a function of θ and this will have noticeable effects on the complexity of the final solution. Next, solving for r as it appears in (3.9)

$$r = \frac{R(\theta)\sin(\theta)n_c(\theta)}{n}, \tag{3.16}$$

implies that

$$\mathrm{d}r = \left[R'(\theta)\sin(\theta)n_c(\theta) + R(\theta)\cos(\theta)n_c(\theta) + R(\theta)\sin(\theta)n_c'(\theta)\right]. \tag{3.17}$$

After equating the integrands as was done for the hemispheric surface, and performing a little algebraic manipulation

$$\frac{n_c'(\theta)}{n_c(\theta)} = n\left[\frac{\sqrt{(R(\theta))^2 + (R'(\theta))^2}}{R(\theta)\sin(\theta)} - \frac{R'(\theta)}{R(\theta)} - \frac{\cos(\theta)}{\sin(\theta)}\right]. \tag{3.18}$$

Solving for $n_c(\theta)$ with $n = 1$,

$$n_c(\theta) = \frac{e^{\int \chi(\theta)\mathrm{d}\theta}}{R(\theta)\sin(\theta)} \tag{3.19}$$

where

$$\chi = \frac{\sqrt{(R(\theta))^2 + (R'(\theta))^2}}{R(\theta)\sin(\theta)}. \tag{3.20}$$

which leads to the desired equivalence

$$\int_0^{\frac{\pi}{2}} e^{\int \chi(\theta)\mathrm{d}\theta}\chi(\theta)\mathrm{d}\theta = \int_0^a \mathrm{d}r = a, \tag{3.21}$$

when $b < a$.

Inspection of (3.19) reveals that $n_c\left(\frac{\pi}{2}\right) = 1$ (which means the proposed cloak has the same refractive index at its perimeter as the surrounding approach plane), but as $\theta \to 0$, $n_c \to 0$. Ultimately this problem can be dealt with by using a technique proposed by Horsley *et al.* [71] where singular refractive indices can be removed by creating an appropriately sculpted surface. In this particular instance, in order to account for a refractive index equal to zero, a very sharp point (with an appropriate profile) is introduced instead. This takes advantage of the underlying idea of TO in the context of surface waves where an equivalence exists between material properties such as refractive index and geometric properties such as length or curvature.

Having established that the proposed technique works for cloaking rotationally symmetric surfaces whose profiles are ultimately expressed in terms of $R(\theta)$, a further generalized technique is explored where $R(\theta)$ is not known or possibly even obtainable in a closed form. As it turns out, this exact circumstance is quite common when one needs to design a surface that is both smooth (does not possess a point or cusp, much like what was seen in the cone) and does not introduce a sharp curvature, K, mismatch with the flat approach plane (as was seen in the case of the hemisphere), and is investigated in the next section.

3.3 Numerical solution for cloaking surface deformations

To illustrate the need for a numerical solution to the proposed formalism, consider $\gamma(x) = e^{-3x^2}$, which meets both the conditions of possessing no cusps/points for all $x \in [0, \infty]$ as well as having a smooth transition to the approach plane. Using the traditional relationship between Cartesian and polar coordinates as was done for the conic surface deformation, where $x = R\sin(\theta)$ and $z = \gamma(x) = R\cos(\theta)$, results in the following relation

$$R\cos(\theta) = e^{-3R^2\sin^2(\theta)}, \tag{3.22}$$

where it is not possible to solve for $R(\theta)$ explicitly, which in turn means that the proposed formalism can not be directly applied. However, there is a way to solve for n_c, but it relies on successfully performing two distinct tasks. First, a numeric approximation (i.e. a forward difference approximation) to a calculate a single variable differential must be implemented

$$f'(a) \approx \frac{f(a+h) - f(a)}{h}, \tag{3.23}$$

which for this particular application appears as

$$n_c' \approx \frac{n_{c,i} - n_{(c,i+1)}}{\Delta\theta}. \tag{3.24}$$

Ultimately, the solution to n_c', just as with any simple derivative of this form, can be made arbitrarily accurate by altering $\Delta\theta$. Beyond this, it is important to keep in mind that (3.24) is only a valid approximation of the derivative if and only if the contour under investigation is void of any discontinuous features like cusps, creases, holes or edges at points of interest. Taking this into account, a generalized form of (3.12) is put forward

$$\frac{n_c'(\theta)}{n_c(\theta)} = \frac{1}{\sin(\theta)} - \frac{R'(\theta)}{R(\theta)} + \frac{\cos(\theta)}{\sin(\theta)} \tag{3.25}$$

in which (3.24) is then substituted

$$\frac{n_{c,i} - n_{c,i+1}}{\Delta\theta n_{c,i}} = \csc(\theta_i) - \frac{R'(\theta_i)}{R(\theta_i)} + \cot(\theta_i), \tag{3.26}$$

and $n_{c,i+1}$ is solved for

$$n_{c,i+1} = n_{c,i} - \Delta\theta \left[\csc(\theta_i) - \frac{R'(\theta_i)}{R(\theta_i)} + \cot(\theta_i)\right], \tag{3.27}$$

where $n_{c,i}$ is an a priori boundary condition, i is the index of an element, and $R'(\theta)$ is determined numerically in the same fashion as described in (3.24).

Here it is worth noting that the simple forward-difference approximation scheme put forward to solve for n_c in (3.27) is by no means state of the art. However, it is robust enough for the purposes of this thesis and its ability to accurately solve for n_c has been directly compared against known analytical solutions (see Figure 6.2). That said, if a researcher is using MATLAB R2015a [84], a number of built-in functions can be used to solve (3.25) as it is a first order ordinary differential equation (ODE). For example, assuming that the right-hand side of (3.25) can be represented symbolically (as is the case when the surface deformation is a hemisphere and $R(\theta) = R$), then the function dsolve(eqn, cond) [85] solves the ODE 'eqn' with initial or boundary conditions 'cond.' Now in the case when $R(\theta)$ is not symbolically represented, a more general ODE solver that is available to MATLAB users, via the MuPAD [84] interface, can be used: numeric::odesolve(f, $x_0...x$, Y_0, method) [86]. This function returns a numerical approximation to the solution of $Y(x)$ of the first order ODE $\frac{dY}{dx} = f(x, Y)$, with $Y(x_0) = Y_0$. In the context of this function the term 'method' refers to one of the 36 different choices of single-step Runge-Kutta-type methods [87] including 'RK4' which

is the fourth order Runge-Kutta method.

Returning to the question of finding $R(\theta)$, a direct relationship between the sets, at least in this particular example, $0 \leq x \leq x_0$ and $0 \leq \theta \leq \frac{\pi}{2}$, can be established

$$x = [0, ..., x_0],\ z = e^{-3x^2},\ \tan(\theta) = \frac{x}{z}, \tag{3.28}$$

which implies

$$\theta = \tan^{-1}\left(\frac{x}{z}\right). \tag{3.29}$$

In doing so, the problem of not being able to express $R(\theta)$ in a closed form in (3.22), is dealt with by instead populating $R(\theta)$ 'along-side' $R(x)$, with

$$R(x) = \sqrt{x^2 + z^2} = \sqrt{x^2 + \left(e^{-3x^2}\right)^2}. \tag{3.30}$$

Combining these two techniques it is possible to iteratively solve for $n_{c,i+1}$ in (3.27).

In conclusion, a generalized analytical approach is derived for cloaking rotationally symmetric surface deformations whose profiles, γ are represented in a close-form via $R(\theta)$. For the cases where $R(\theta)$ can not be solved for in a closed form, a numeric solution is put forward. Between these two methods it is possible, to cloak any smooth rotationally symmetric surface deformation from an incident surface wave, as is demonstrated via full-wave EM solver results in the next section.

3.4 Simulations

Though, any solution borne out of Fermat's principle explicitly relies on geometrical optics, it is always best, when computationally feasible, to validate a proposed design via a full-wave EM solver. In doing so, it is possible to see if the proposed design is in fact operating within the acceptable region (electrically large devices relative to wavelength) where the wave behavior of the EM wave becomes negligible. This is an important feature to keep in mind because as was demonstrated in all of the previous derivations for n_c there are no f_0 or λ_0 terms, which means it is up to the user to ensure this condition is met.

3.4.1 Simulation setup

To start a few details involving the specifications of the simulation must be understood. First, and perhaps most importantly, the behavior of a surface wave is modeled using a parallel plate waveguide method [88], where the refractive index is effectively sandwiched between two perfect electric conductor (PEC) sheets (normal to the Z-axis)

that are separated by a distance of $\lambda_0/10$. This electrically small separation between the two PEC sheets ensures that $\underline{E}$ always remains normal to surface deformation. Next, the remaining edges of the surface are bounded by a $1\lambda_0$ thick perfectly matched layer (PML), and the method of excitation is a bounded space wave with $\underline{E}$ oriented along the Z-direction, and $\underline{k}$ oriented in the XY-plane. Finally, as a finite element method (FEM) EM solver is used for these simulations (COMSOL 4.4) the mesh configuration is set to where no tetrahedral edge length (in the entire model) is greater than $\lambda_0/15$, which practically ensures a convergent solution will be reached.

As was mentioned before, due to the inherent requirements of GO to be satisfied, the deformation itself must be electrically large. Put another way, the phase of the impinging wave front must vary more rapidly (in the direction of $\underline{k}$) than n_c (also in the direction of $\underline{k}$). To some extent, this allows the lower limit of the operating frequency (via the dispersion relation) of a design to be determined, as is done for the case of a hemispheric deformation below. First, the GO conditional relating to curvature in an an isotropic medium that was introduced in Chapter 2 is restated

$$|R_{ij}|\,\lambda_m^2 \ll 1, \tag{3.31}$$

where R_{ij} is the Ricci tensor and λ_m is the wavelength of light in an isotropic medium. In order to solve for R_{ij}, first the metric tensor needs to be determined, followed by the non-vanishing Christoffel symbols (see Appendix), and then lastly the Riemann tensor. As a hemispheric deformation is the surface of interest in this derivation the spherical coordinate system is utilized and the line element for a sphere is found to be

$$ds^2 = r^2 d\theta^2 + r^2 \sin^2(\theta)\, d\phi^2, \tag{3.32}$$

where r is the constant radius of the hemisphere. Next, the metric tensor, g_{ij}, is populated as the coefficients of the line element with

$$g_{\theta\theta} = r^2, \quad g_{\phi\phi} = r^2 \sin^2(\theta), \quad g_{\theta\phi} = g_{\phi\theta} = 0. \tag{3.33}$$

Then, the non-vanishing Christoffel symbols are found

$$\Gamma^{\theta}{}_{\phi\phi} = -\frac{1}{2}\sin(2\theta), \quad \Gamma^{\phi}{}_{\theta\phi} = \Gamma^{\phi}{}_{\phi\theta} = \cot(\theta), \tag{3.34}$$

and using

$$R^{i}{}_{jlm} = \Gamma^{i}{}_{mj,l} - \Gamma^{i}{}_{lj,m} + \Gamma^{k}{}_{mj}\Gamma^{i}{}_{lk} - \Gamma^{k}{}_{lj}\Gamma^{i}{}_{km}, \tag{3.35}$$

it is easy to calculate for the Riemann tensor. As a two-dimensional surface is under

investigation the Riemann tensor has only one independent component, which in this example can be taken to be $R_{\theta\phi\theta\phi}$ and is

$$\begin{aligned} R_{\theta\phi\theta\phi} &= g_{\theta i} R^{i}{}_{\phi\theta\phi} \\ &= g_{\theta\theta} R^{\theta}{}_{\phi\theta\phi} \\ &= r^2 \left(\Gamma^{\theta}{}_{\phi\phi,\theta} - \Gamma^{\theta}{}_{\theta\phi,\phi} + \Gamma^{k}{}_{\phi\phi} \Gamma^{\theta}{}_{\theta k} - \Gamma^{k}{}_{\theta\phi} \Gamma^{\theta}{}_{k\phi} \right) \\ &= r^2 \left(-\cos(2\theta) - 0 + 0 - \Gamma^{\phi}{}_{\theta\phi} \Gamma^{\theta}{}_{\phi\phi} \right) \\ &= r^2 \left(\sin^2(\theta) - \cos^2(\theta) + \cos^2(\theta) \right) \\ &= r^2 \sin^2(\theta). \end{aligned} \tag{3.36}$$

The Ricci tensor, R_{ij}, can then be solved via

$$R_{ij} = g^{ab} R_{aibj}, \tag{3.37}$$

and because the metric is diagonal and g^{ab} is the inverse of g_{ab}

$$g^{\theta\theta} = \frac{1}{r^2}, \quad g^{\phi\phi} = \frac{1}{r^2 \sin^2(\theta)}. \tag{3.38}$$

Then using the symmetries of the Riemann tensor, the components of the Ricci tensor can be solved for by

$$\begin{aligned} R_{\theta\theta} &= g^{ab} R_{a\theta b\theta} && (3.39) \\ &= g^{\phi\phi} R_{\phi\theta\phi\theta} \\ &= \frac{1}{r^2 \sin^2(\theta)} r^2 \sin^2(\theta) \\ &= 1, && (3.40) \\ R_{\phi\phi} &= g^{ab} R_{a\phi b\phi} \\ &= g^{\theta\theta} R_{\theta\phi\theta\phi} \\ &= \sin^2(\theta), && (3.41) \\ R_{\theta\phi} &= R_{\phi\theta} = 0. && (3.42) \end{aligned}$$

As the purpose of this derivation is to relate the wavelength in an isotropic medium, which is a scalar, to the curvature of a manifold, the curvature itself must also appear as a scalar. This means that (3.31) now appears as

$$|R| \lambda_m^2 \ll 1, \tag{3.43}$$

where R is the scalar curvature and is defined by

$$R = g_{ij} R^{ij}. \tag{3.44}$$

The second term on the right-hand side of (3.44) can be solved for by raising the indices of R_{ij}

$$\begin{aligned} R^{\theta\theta} &= g^{\theta i} g^{\theta j} R_{ij} \\ &= g^{\theta\theta} g^{\theta\theta} R_{\theta\theta} \\ &= \frac{1}{r^4} \end{aligned} \tag{3.45}$$

$$\begin{aligned} R^{\phi\phi} &= g^{\phi\phi} g^{\phi\phi} R_{\phi\phi} \\ &= \frac{1}{r^4 \sin^2(\theta)}. \end{aligned} \tag{3.46}$$

Then the scalar curvature, which is related to the Gaussian curvature, K, in two dimensions via $R = 2K$, is

$$\begin{aligned} R &= g_{ij} R^{ij} \\ &= r^2 \frac{1}{r^4} + r^2 \sin^2(\theta) \frac{1}{r^4 \sin^2(\theta)} \\ &= \frac{2}{r^2}. \end{aligned} \tag{3.47}$$

This means that

$$\lambda_m \ll \frac{r}{\sqrt{2}}, \tag{3.48}$$

which is in agreement with the general notion of an object needing to be electrically large for the GO approximation to be valid. For the surface deformations investigated in this chapter, and in this thesis in general, it was empirically determined that $\lambda_0 \approx R_0/10$ was an acceptable central operating wavelength, where R_0 would correspond to the largest dimension of a deformation.

3.4.2 Simulation results for surfaces under investigation

The first structure investigated in this study is a hemispherical deformation, whose material profile, n_c, is displayed in Figure 3.2(b). Here it is important to emphasize once again that the refractive index profile of the cloak is directly related to the refractive index of the approach plane, and $n_c < 1$ can be addressed by simply increasing the refractive index of the approach plane. In this study the refractive index of the approach plane is kept at unity purely for illustration purposes and a realizable design that has

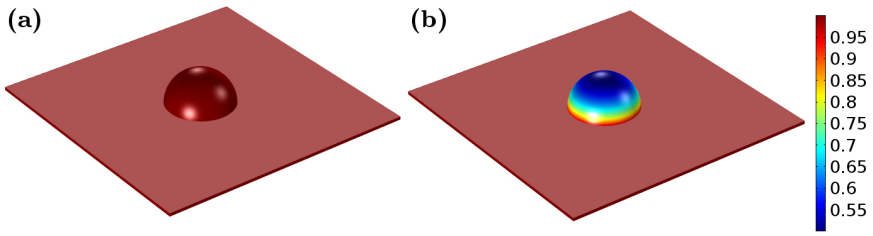

Figure 3.2: n_c for an (a) uncloaked hemispheric deformation and (b) cloaked hemispheric deformation.

an approach plane with a refractive index of $\sqrt{15}$ is examined later on in this chapter. Moving on, the result of exciting this structure with a plane wave is displayed in Figure 3.3. It is important to note that the results from this simulation as well as those found

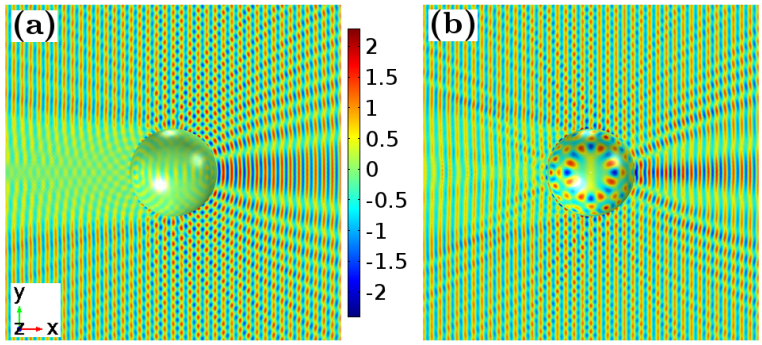

Figure 3.3: Incident plane wave is propagating in the -X-direction (from right to left). In (a) the homogeneous, uncloaked hemispheric deformation and (b) the cloaked hemispheric deformation. Both results are for E_z.

through out this thesis are for the total field which is defined as the summation of the incident and scattered fields. Inspection of Figure 3.3(a) reveals a minor level of backscattering, as well as a severe shadowing effect, in the forward scattering region, where the term shadowing is a means of describing the net effect of the phase delay of phase fronts traversing different path lengths. When a cloak is preforming properly, no shadowing and minimal, if any, backscattering is expected. That said, it should be noted that depending upon the particular application that a designer may have in mind, a certain level of backscattering may be acceptable. Moving on, the proposed cloak, does appear to greatly reduce the level of forward-scattering, but still has a noticeable level of backscattering. This undesirable scattering is a result of the proposed design methodology not taking into account the curvature mismatch between the flat approach plane and the hemisphere which is addressed in Chapter 5. Having identified that this curvature mismatch was a problem, a surface deformation whose slope could be controlled at will was investigated: the conic deformation.

Plotting (3.19) along a cone whose height is less than its radius (or in this case whose height is half that of its radius) produces the material profile displayed in Figure 3.4(b). It should be noted that due to a material singularity ($n_c = 0$) at the peak of the cone, the

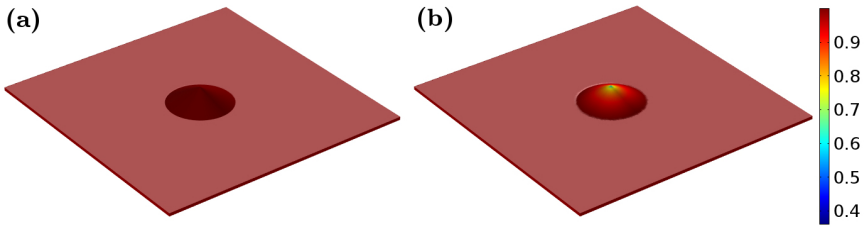

Figure 3.4: n_c for an (a) uncloaked conic deformation and (b) cloaked conic deformation.

implemented solution is a slight approximation to this, and was achieved by making the refractive index arbitrarily small, but never entirely zero, at this singularity. In Figure 3.5(a) there is a pronounced shadowing effect, but very little backscattering when compared to the hemispherical case, which demonstrates that a curvature matching of sorts at the interface of the approach plane and the cone has not occurred. Though in Figure 3.5(b) the forward and backscattering performance is better (on the whole) than that of the hemispheric cloak, there is a still a small amount of scattering that is preventing this from being, at least qualitatively, a perfect cloak. The cause of this

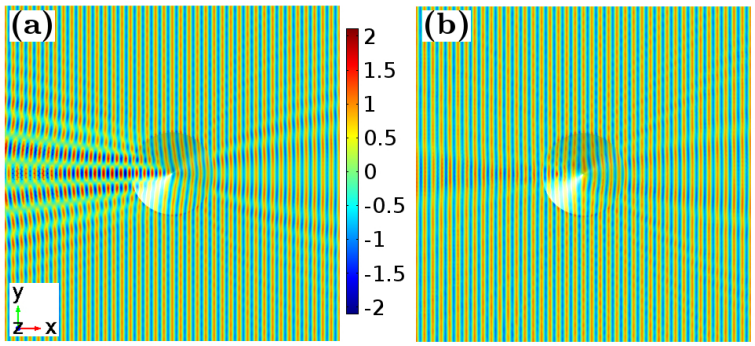

Figure 3.5: Incident plane wave propagating in the -X-direction. In (a) the homogeneous uncloaked conical deformation (b) the cloaked conical deformation. Both results are for E_z.

scattering, is due to EM solver's inability to faithfully reproduce a refractive index of zero at the point of the cone. In order to solve this problem, a surface that has a smooth transition from the approach plane to itself, and is void of any material singularities is investigated.

One such surface that meets both of these criteria is a Gaussian deformation which

is represented parametrically as

$$z(r) = e^{-3r^2}, \tag{3.49}$$

where, z is the height of the surface as a function of its distance from the origin. Through varying r from 0 to 1, one is able to trace a space curve, and then revolve said curve around the Z-axis to create a surface. In order to solve for the appropriate cloaking design, (3.27) was used and the resulting refractive index is displayed in Figure 3.6(b). Next, exciting the deformation in the same fashion as the previous two cases

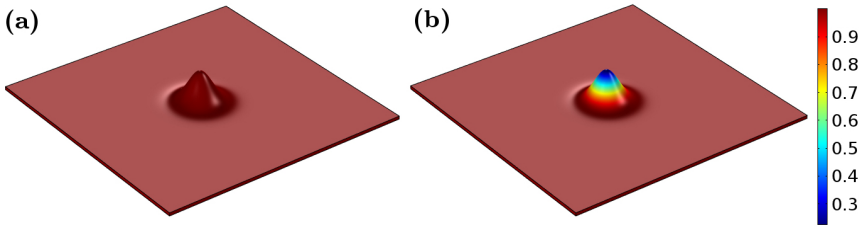

Figure 3.6: n_c for an (a) uncloaked Gaussian deformation and (b) cloaked Gaussian deformation.

produces the field displayed in Figure 3.7. Here virtually no forward, back and even side-scattering scattering is observed as one expects after successfully removing any material and geometrical singularities that were present in the previous cloaks.

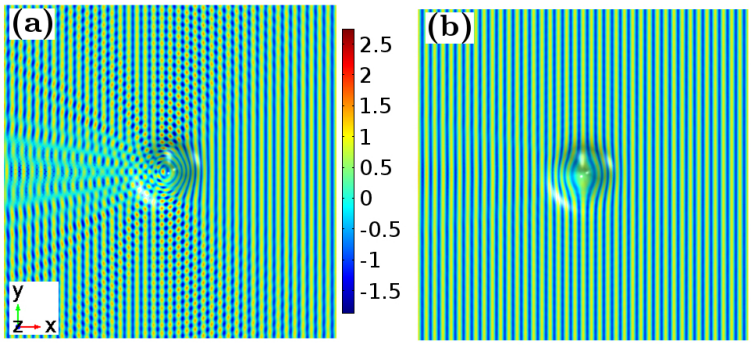

Figure 3.7: Incident plane wave propagating in the -X-direction. In (a) the homogeneous uncloaked Gaussian deformation and (b) the cloaked Gaussian deformation. Both results are for E_z.

In order to quantify just how well the proposed surface wave cloaks operate a sample line is placed in the shadow region (see Figure 3.8) of each cloak. First the results for the hemispheric deformation from Figure 3.3 are examined (see Figure 3.9). Now, in the context of this thesis if a proposed surface wave cloaking device is to function properly, it must successfully emulate the behavior (both amplitude and phase) of a

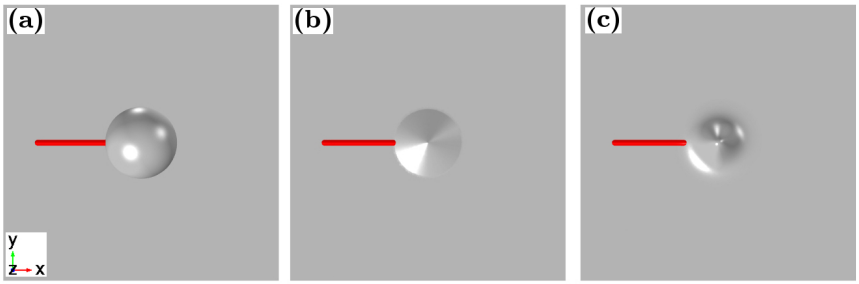

Figure 3.8: Sampling line (red line) used to quantify cloak performance. For a (a) hemispheric deformation (b) conic deformation, and (c) Gaussian deformation.

surface wave traveling along a flat surface. From Figure 3.9 it is clear that though the

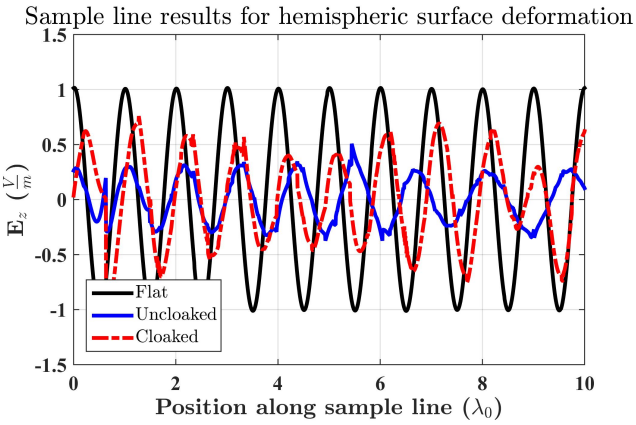

Figure 3.9: E_z along sample line in shadow region of a hemispheric deformation.

proposed cloak (red dashed curve) does not entirely emulate the behavior of a surface wave along a flat plane (black curve), it does provide a level of improvement over the uncloaked deformation (blue dashed-curve) in terms of amplitude and phase agreement. However, as was pointed out in the commentary on Figure 3.3 this is not a result of n_c being incorrect or the optical limit not being reached as much as it is due to the curvature mismatch between the hemisphere and the approach plane. With that being said the sample line results for the conic deformation are now studied.

In Figure 3.10 one notes a far better level of agreement between the surface waves along a flat surface (black curve) and the surface waves passing along the cloaked cone itself (red dashed curve). However, this particular cloak can be improved upon in the sense that there is a slight disagreement in the amplitude levels between the flat and cloaked results, which is a result of the material singularity of n_c on the point of the cone. In terms of the behavior of the field in the shadow region of the uncloaked surface deformation it is noted that it has an amplitude greater than the incident field of 1

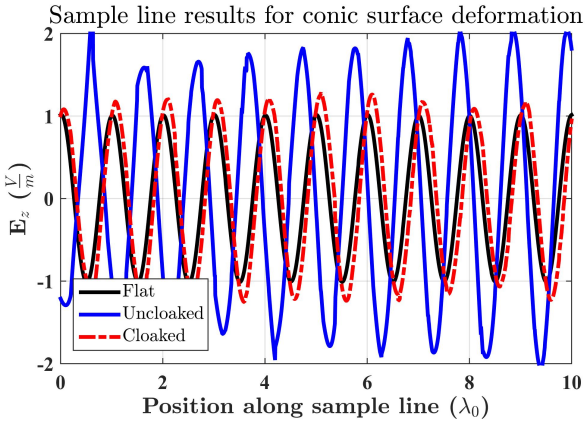

Figure 3.10: E_z along sample line in shadow region of a conic deformation.

V/m which simply indicates the creation of a constructive (as opposed to destructive in the case of the hemisphere) interference pattern. Next, the Gaussian deformation as it relates to this sample line study is investigated (see Figure 3.11). Here it is apparent

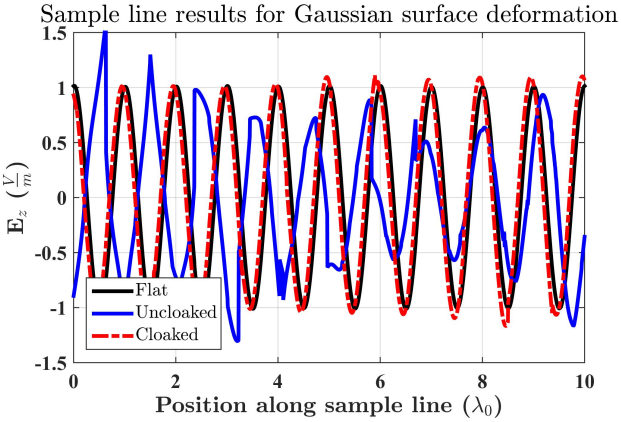

Figure 3.11: E_z along sample line in shadow region of a Gaussian deformation.

that the proposed cloak (dashed red curve) performs exceptionally well in terms of level of agreement with respect to the amplitude and phase of a plane wave traveling along a flat plane (black curve). Finally, the cloaking results for all three surface deformations are plotted together (see Figure 3.12), and it is apparent that in terms of correctly emulating the behavior of a surface wave along a flat plane the Gaussian cloak (owing to its lack of material and geometrical singularities) is the superior design.

Therefore, a number of conclusions can be drawn from the simulation results. First, from the hemisphere surface deformation simulations (Figure 3.3 and Figure 3.9) it is clear that if a surface deformation is to be cloaked it must not possess any curvature discontinuities between the flat approach plane and the deformation itself. Second,

from the conic surface deformation simulations (Figure 3.5 and Figure 3.10) it was demonstrated that discontinuities in the form of sharp cusps or points on the surface deformation itself, which though not as detrimental as a curvature discontinuity between the flat approach plane and the curved surface, still produce undesirable scattering behavior, also need to be avoided. Taking both of these facts into consideration, if the proposed cloaking technique from this chapter is to be used on a surface deformation, the surface itself must be void of these two discontinuities. In this study, that surface was a simple Gaussian deformation (3.49) which allowed for a virtually perfect surface wave cloak (Figure 3.7 and Figure 3.11).

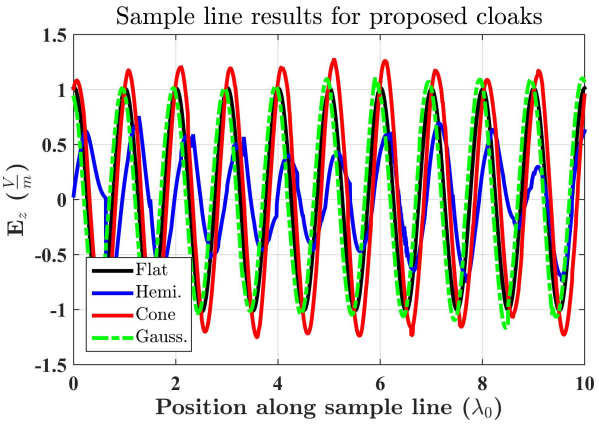

Figure 3.12: E_z along sample line for different cloak designs.

3.5 Realizable surface wave cloak

Having demonstrated that the proposed analytic and numeric solutions do in fact work via full-wave EM simulations, a real-world implementation of the proposed technique using a deformation structurally similar to the Gaussian deformation (whose exact profile can be found in the Appendix) is studied. The following design and simulation results (namely Figure 3.13–3.15) were originally produced by Dr. Oscar Quevedo-Teruel and later adapted by the author to be included in this thesis. Here, a graded dielectric placed on top of a curved metallic surface is considered. In an attempt to achieve the same propagation characteristics as seen in the sandwiched PEC waveguide simulation, it is necessary to alter the required ε_r, for a predetermined slab thickness, which has PEC below and air above. In other words a curved dielectric waveguide with a PEC ground plane is called for. First, a central operating frequency of 10 GHz and an approach plane thickness of 4.5 mm ($0.15\lambda_0$) is chosen. Then, an eigenmode solver (CST Microwave Studio 2014 [89]) was used to calculate the amount of modal confinement ($|E_z|$) within the substrate for various dielectric constants (ε_r equal to 2, 7, 11 and 15) as displayed in Figure 3.13.

Here it is important to realize that how one plans on exciting the surface waves will to some extent effect the design of the cloak itself. For example, in the coming simulations an idealized port is used, but in reality if this design were ever to be fabricated and experimentally validated, one would have to ensure proper coupling (namely in the form of impedance matching) between a waveguide or horn antenna and the refractive index chosen from Figure 3.13. This is done to maximize the amount of transmitted energy (in the form of surface waves) to the device, which would prove beneficial when trying to establish good levels of agreement between the simulation and experimental results. That said, as the cloak is meant to interact with surface waves, it is necessary to confine as much energy as possible to the surface of the structure, meaning that according to the insets found in Figure 3.13, for this particular surface, ε_r should range from 9 through 15. The insets themselves are separated into two regions with the entire region below the horizontal line (and bounded by PEC) being the dielectric and the entire region above the line being air, as it is labeled. As a final design step, the cloak is radially discretized into seven distinct layers to reduce the fabrication complexity with the boundaries between different layers oriented normal to the surface (see Figure 3.14). Finally, the proposed design is simulated using the time domain solver in CST Microwave Studio 2014 with the following setup. First, a minimum cell edge length of $\lambda_0/15$ is chosen to ensure a convergent and in turn accurate solution (an accuracy level of -30 dB is selected) is reached. Then the entire structure is bounded by air above and below, and a λ_0 thick PML at its remaining

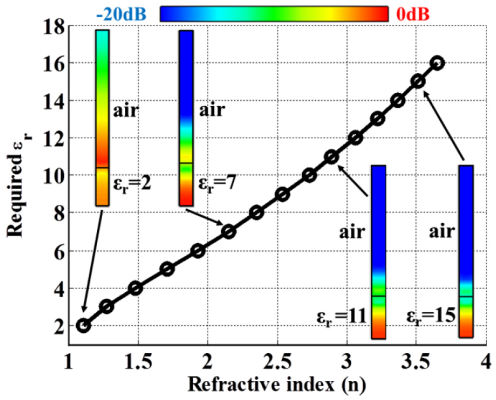

Figure 3.13: Required ε_r for a 4.5 mm slab as a function of refractive index at 10 GHz. All insets are $|E_z|$ field component and demonstrate the confinement of modes within the slab.

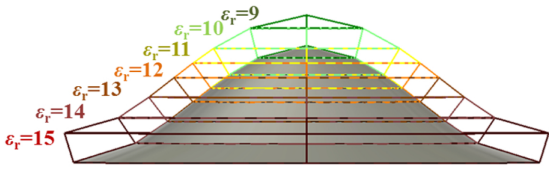

Figure 3.14: Cross section of discretized cosine-shaped cloak, with the grey area representing a PEC ground plane.

four sides. Lastly the surface is excited (over a frequency band) by an idealized port at its edge which produces the field patterns displayed in Figure 3.15. Here there is a pronounced level of shadowing when the deformation is uncloaked (the material overlay is homogeneous) in Figure 3.15(a), but the cloak implementation seen in Figure 3.15(b), completely corrects this.

In Figure 3.15(c, d) the frequency scanning performance of the cloak is validated, which is worth commenting on in that it demonstrates that as long as the GO approximation is not violated, the device functions properly. Furthermore this bandwidth (here of 4 GHz) means that this device (owing to its all-dielectric fabrication) does not suffer from one of the primary limitations that plagued earlier metamaterial cloak designs, namely that of narrow bandwidth performance - a direct consequence of relying on the resonant properties of the metamaterial itself. This wideband performance could prove especially useful for surface wave antennas that are used for communication purposes. To ascertain how well the surface waves are in fact bound to the device (and not radiating into free-space), E_z along a cut plane for $f = 10$ GHz is displayed in Figure 3.16. Here the large dielectric constant used for the material overlay confines most of the energy to the surface regardless of whether or not it is cloaked. However the field enhancement displayed after the surface wave travels over the deformation in Figure

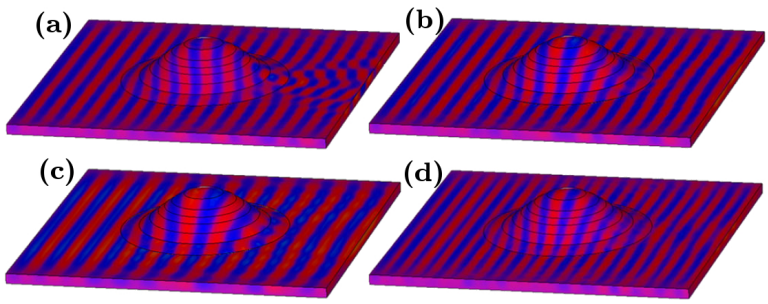

Figure 3.15: E_z of a surface wave propagating from left to right on the surface of the cosine-shaped cloak. (a) Homogeneous slab and (b-d) seven layered cloaking structure. Results for (a, b) are at the design frequency of 10 GHz, and (c) and (d) are at 8 GHz and 12 GHz, respectively.

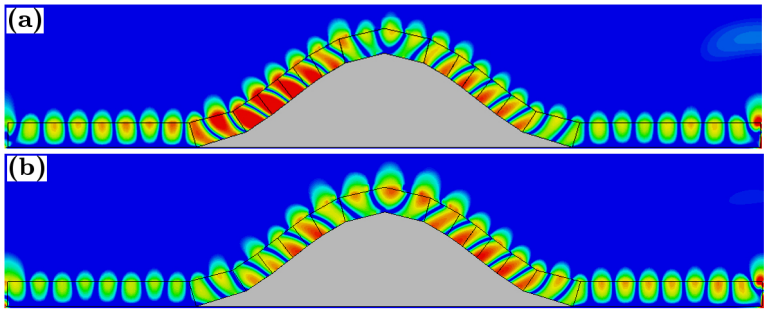

Figure 3.16: E_z along a cut plane for $f = 10$ GHz with a surface wave traveling from right to left for the (a) homogeneous material overlay ($\varepsilon_r = 15$) and (b) cloaking material overlay described in Figure 3.14. All results are normalized to the source

3.16(a) indicates that it is not emulating the modal behavior found in a flat dielectric waveguide. For this to occur the waveguide modes would have to be nearly symmetric (varying only due to their distance away from the source) about the center of the surface deformation as they are in Figure 3.16(b). Taking the simulation results found in Figure 3.15 and Figure 3.16 into consideration the efficacy of a realizable surface wave cloaking device is validated. In terms of a general application, such surface wave cloaks could prove useful to researchers who are trying to minimize (or remove entirely) the undesirable effects of surface curvature as it applies to antenna design (e.g. leaky wave antennas [90–96] on curved surfaces). Worth mentioning also, is that an actual device based on the design displayed in Figure 3.14 has been fabricated and is currently (as of October 2015) under testing at Queen Mary University of London.

3.6 Conclusions

In this chapter a new method (fundamentally different from previous methods proposed by transformation plasmonics [43, 80]), utilizing Fermat's principle, was used to create an omnidirectional, purely dielectric, electrically thin material overlay to cloak a finite, curved (i.e. non-Euclidean) surface deformation from surface waves in the microwave regime. First its derivation was produced and a number of sample surface deformations (hemispheric, conic and Gaussian) were studied. Then, a numerical solution was derived to account for any limitations found in the analytical approach when $R(\theta)$ (which is related to the profile of a given surface deformation) could not be expressed in a closed-form. Next, a parallel plate waveguide simulation technique was introduced and the performance of a hemispheric, conic and Gaussian cloak was investigated using a full-wave electromagnetic solver (COMSOL 5.0). Here it was demonstrated that the curvature, K, mismatch between the surface deformation and the flat approach plane would lead to undesirable scattering and because of this, particular focus was placed on surfaces that did not have this problem. To further quantify the performance of each cloak, a sampling line study was carried out and it was determined that the Guassian cloak most closely emulated the wave behavior of a plane wave traveling in a flat waveguide.

Next, to convert the proposed material solution from its parallel plate waveguide form into a real surface wave form, the required material parameters (i.e. ε_r) for a thin material on a PEC ground plane were determined via the use of an eigenmode solver in CST Microwave Studio 2014. These results where then used to design an all-dielectric material overlay of uniform thickness, that would cloak a cosine-shaped surface deformation (whose profile can be found in the Appendix) from a surface wave. The proposed device was then simulated using the time domain solver in CST Microwave Studio 2014 and it was demonstrated that the surface wave cloak design functioned properly in the desired frequency band and possessed a good level of modal confinement. The surface wave cloaking design recipe described in this chapter is novel because it leads to the creation of a thin, isotropic, all-dielectric material overlay that can be used to cloak a rotationally symmetric surface deformation for all angles of incidence and over a given frequency band.

Chapter 4

Rotationally symmetric surface wave lenses

4.1 Introduction

In this chapter an adaptation of the work described in Chapter 3 (which is a detailed account of a work by Mitchell-Thomas *et al.* [97]) is used to create all-dielectric, electrically thin material overlays that map rotationally symmetric (RS) surface wave lenses onto RS surface deformations. As the work detailed in this chapter is ultimately concerned with the manipulation of surface waves (via transformation optics (TO)) it does share a common heritage with the work of Huidboro *et al.* [43, 81], Liu *et al.* [80], Kadic *et al.* [44, 82] and Zhu *et al.* [60]. Of these works the ones that propose surface wave lenses (surface plasmon polaritons (SPPs) lenses to be exact) include Huidboro *et al.* [81], where an anisotropic and isotropic focusing lens were proposed and validated and Liu *et al.* [80] where a plasmon Luneburg lens is proposed and validated. Important to note, however, is that of these two [80, 81], the plasmon Luneburg lens designed in [80] is the only one that focuses on manipulating the SPPs across a curved (non-Euclidean) surface. Another effort that describe the use of surface waves via lenses, but on a flat surface and for antennas applications, was by Yang *et al.* [83].

Therefore, the work described in this chapter is new not only because it stems from the approach proposed in Chapter 3 [97], but also because very little work has been done in the TO community involving lenses on non-Euclidean (i.e. curved) surfaces. That said, the outline for this chapter is as follows. First, an analytical solution is derived that allows for the mapping of a rotationally symmetric (RS) flat lens onto a RS surface deformation, and a number of examples are discussed. Then, a numerical solution is detailed that accounts for the limitations encountered in analytical solution.

Afterwards, two different flat lenses are mapped onto three different surfaces, and there electromagnetic (EM) behavior is analyzed via full-wave simulations. Finally, a design methodology is proposed and validated were two different lens are mapped onto a cosine-shaped deformation via correctly manipulating the thickness of an isotropic, homogeneous material overlay.

Starting with the two equations (in Cartesian coordinates) that allowed for the creation of RS surface wave cloaks in the previous chapter:

$$\int_0^{\frac{\pi}{2}} n_c(\theta)\sqrt{(R(\theta))^2+(R'(\theta))^2}\,\mathrm{d}\theta = n\int_0^R \mathrm{d}r, \tag{4.1}$$

and

$$2\pi R(\theta)\sin(\theta)n_c(\theta) = 2\pi r n, \tag{4.2}$$

and noting that if n as it appears on the R.H.S. of both (4.1) and (4.2) was not a constant for all of r, but instead varied as $n(r)$ (as is the case for flat surface wave lenses), then by solving for $n_c(\theta)$ one would in effect be mapping a flat lens onto a RS surface whose profile would be defined by $R(\theta)$. To investigate this problem, first (4.1) is recast as

$$\int_0^{\frac{\pi}{2}} n_2(\theta)\sqrt{(R(\theta))^2+(R'(\theta))^2}\,\mathrm{d}\theta = \int_0^a n_1(r)\mathrm{d}r, \tag{4.3}$$

where, $n_1(r)$ is refractive index distribution of a RS flat lens, $n_2(\theta)$ is the refractive index along the curved surface, and a is the outer radius of the flat lens ($a = R_0$, unless otherwise noted). Then (4.2) appears as

$$2\pi R(\theta)\sin(\theta)n_2(\theta) = 2\pi r n_1(r). \tag{4.4}$$

The new relation between the two surfaces is illustrated in Figure 4.1, where the color gradient indicates that neither surface is of uniform refractive index. Just as was the

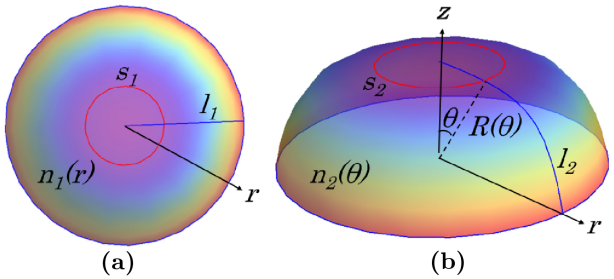

Figure 4.1: Ray paths for a RS flat system (a) and a RS curved surface (b), where $n_1(r)$ and $n_2(\theta)$ represent their refractive index distributions, respectively.

case with the design methodology proposed in Chapter 3, the only inherent limitations

on both the surface deformations and the flat lenses is that both of them are rotationally symmetric about a common axis. That said, the mapping of a set of flat lens profiles onto a set of surface deformations is now investigated.

4.2 Analytical solutions for mapping flat lenses onto surfaces

4.2.1 Mapping a black hole lens onto hemispheric surface deformation

The first case that is investigated is that of mapping a flat black hole lens (BHL) onto a hemispheric surface deformation. A BHL, in the simplest sense, is a lens that permits the entrance of light rays, regardless of angle of incidence, but does not allow them to escape. In this particular example, the BHL has a radial refractive index (using a simplified version of the profile from [98]) as

$$n_1(r) = n_0\left(\frac{R_0}{r}\right)^2, \tag{4.5}$$

where R_0 is the outer radius of the BHL and n_0 is the lens' background index (the refractive index at the boundary of the lens). Letting $n_0 = 1$, and plotting (4.5) (see Figure 4.2), reveals that as $r \to 0$, $n_1(r) \to \infty$, meaning a material singularity exists at the center of this particular flat lens, which simply needs to be kept in mind when analyzing the final mapped solution. Having defined $n_1(r)$, a technique to solve the

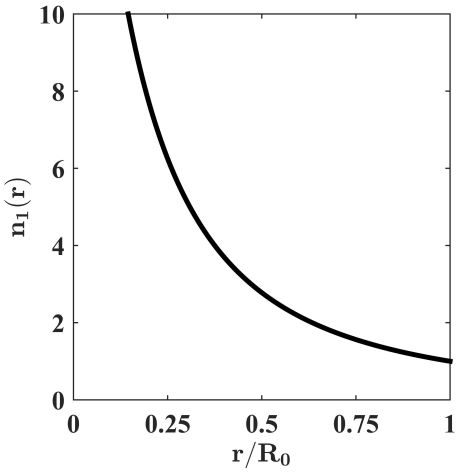

Figure 4.2: Refractive index profile of a black hole lens as defined by (4.5).

refractive index of the curved surface, $n_2(\theta)$ is investigated. Taking into account that

a hemispheric deformation is the surface of interest, (4.3) and (4.4) appears as

$$\int_0^{\frac{\pi}{2}} n_2(\theta) R_0 \, \mathrm{d}\theta = \int_0^a n_1(r) \mathrm{d}r, \tag{4.6}$$

and

$$2\pi R_0 \sin(\theta) n_2(\theta) = 2\pi r n_1(r), \tag{4.7}$$

respectively, because for a hemispheric surface deformation

$$R(\theta) = R_0, \tag{4.8}$$

where R_0 is the radius of the hemisphere. Solving for $n_2(\theta)$ in (4.7) reveals

$$\begin{aligned} n_2(\theta) &= \frac{r n_1(r)}{R_0 \sin(\theta)} \\ &= \frac{n_0 \left(\frac{R_0}{r}\right)^2}{R_0 \sin(\theta)} \\ &= n_0 \frac{R_0}{r \sin(\theta)}, \end{aligned} \tag{4.9}$$

because, as previously stated, the radius of the hemispheric deformation and the flat lens are equivalent. Ultimately however, $n_2(\theta)$ needs to be expressed solely in terms of θ which means r must be solved for in terms of θ. One way to do this, is to take advantage of a previously derived relation found when attempting to cloak a hemispheric deformation, namely

$$r = R_0 \tan\left(\frac{\theta}{2}\right). \tag{4.10}$$

Substituting (4.10) into (4.9) produces the necessary refractive index to make a hemispheric deformation behave, electrically speaking, as if it were a flat BHL

$$n_2(\theta) = \frac{n_0}{1 - \cos(\theta)}. \tag{4.11}$$

As a quick validity check, (4.5) and (4.11) can be substituted back into (4.3)

$$\int_0^{\frac{\pi}{2}} R_0 \frac{n_0}{1 - \cos(\theta)} \mathrm{d}\theta = \int_0^a n_0 \left(\frac{R_0}{r}\right)^2 \mathrm{d}r, \tag{4.12}$$

keeping in mind that $a = R_0$ and after a change of variables and a little algebra, can be recast as

$$\int_0^{\frac{\pi}{2}} \frac{n_0}{1-\cos(\theta)} \mathrm{d}\theta = \frac{1}{2} n_0 \int_0^{\frac{\pi}{2}} \csc^2\left(\frac{\theta}{2}\right) \mathrm{d}\theta, \tag{4.13}$$

which evaluates to

$$n_0 \cot\left(\frac{\theta}{2}\right)\Big|_0^{\frac{\pi}{2}} = n_0 \cot\left(\frac{\theta}{2}\right)\Big|_0^{\frac{\pi}{2}}, \tag{4.14}$$

as is required. Setting $n_0 = 1$ and plotting $n_2(\theta)$ (see Figure 4.3) reveals, as expected, a material singularity at $\theta = 0$ (the spatial analogue of $r = 0$ from the flat BHL material profile), but ultimately this problem can be dealt with using the transmutation technique proposed by Horsley *et al.* [71], as was reviewed in Chapter 3. Having

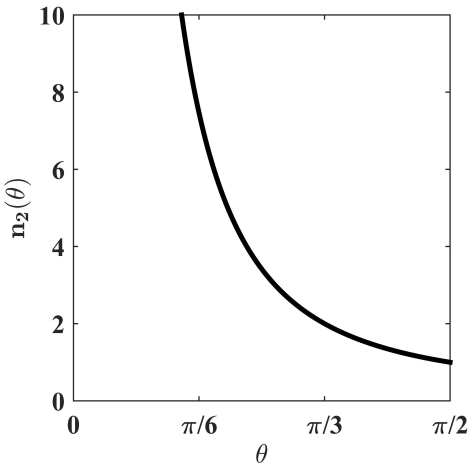

Figure 4.3: Refractive index profile of a hemispheric black hole lens as defined by (4.11).

derived and validated the proposed approach via mapping a flat BHL onto a hemispheric deformation, another lens/surface pairing is investigated: a flat Luneburg lens and a cone with radius a and height b, where $a > b$.

4.2.2 Mapping a Luneburg lens onto a conic surface deformation

A flat Luneburg lens [99, 100] in its simplest sense, is a lens that takes cylindrical wavefronts, emanating from a point source located on its outer radius, and effectively converts them into planar wavefronts at a point radially opposite the point source. The refractive index profile [101] of a flat Luneburg of outer radius R_0 and background refractive index of n_0 is

$$n_1(r) = n_0 \sqrt{2 - \frac{r}{R_0}}. \tag{4.15}$$

Setting $n_0 = 1$ and plotting (4.15) produces Figure 4.4, which unlike the BHL does not possess any inherent material singularities. Having defined $n_1(r)$ of the flat lens, a

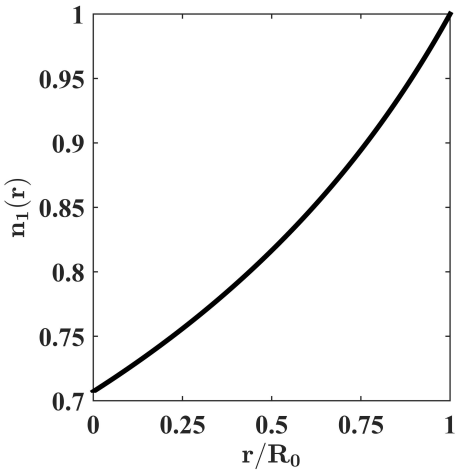

Figure 4.4: Refractive index profile of a Luneburg lens as defined by (4.15).

relation between the flat plane and the cone is established via the cloaking technique entailed in Chapter 3 as follows. First, the Euclidean distance between the origin and a point on the conic surface as a function of θ is found

$$R(\theta) = \frac{b}{\cos(\theta) + \frac{b}{a}\sin(\theta)}. \tag{4.16}$$

Next, (4.3) is introduced as

$$\int_0^{\frac{\pi}{2}} n_2(\theta)\sqrt{(R(\theta))^2 + (R'(\theta))^2}\,\mathrm{d}\theta = \int_0^a n_1(r)\mathrm{d}r. \tag{4.17}$$

Here, just as with the previous example, the solution for $n_2(\theta)$ needs to be expressed purely in terms of θ which can be accomplished by utilizing the relation between r and θ that was found when cloaking a conic surface deformation (with $n_0 = 1$) as is included here

$$r = R(\theta)\sin(\theta)n_c(\theta), \tag{4.18}$$

where

$$n_c(\theta) = \frac{e^{\int \chi(\theta)\mathrm{d}\theta}}{R(\theta)\sin(\theta)}, \tag{4.19}$$

and

$$\chi = \frac{\sqrt{(R(\theta))^2 + (R'(\theta))^2}}{R(\theta)\sin(\theta)}. \tag{4.20}$$

Substituting (4.19) into (4.18) produces

$$r = \frac{a \exp^{\int \chi(\theta) \mathrm{d}\theta}}{\int_0^{\frac{\pi}{2}} \left[\frac{\exp^{\int \chi(\theta) \mathrm{d}\theta}}{R(\theta)\sin(\theta)} \right] \mathrm{d}\theta}, \tag{4.21}$$

thereby solving for r purely in terms of θ. In turn, it is now possible to solve for $n_2(\theta)$ as it appears in (4.3). After equating the electrical path lengths along the circular paths on the cone and the flat plane

$$2\pi R(\theta)\sin(\theta) n_2(\theta) = 2\pi r n_1(r), \tag{4.22}$$

isolating $n_2(\theta)$

$$n_2(\theta) = \frac{r n_1(r)}{R(\theta)\sin(\theta)}, \tag{4.23}$$

and making the necessary substitution for r, the sought after result is obtained

$$n_2(\theta) = n_0 \frac{a \exp^{\int \chi(\theta) \mathrm{d}\theta}}{\int_0^{\frac{\pi}{2}} \left[\frac{\exp^{\int \chi(\theta) \mathrm{d}\theta}}{R(\theta)\sin(\theta)} \right] \mathrm{d}\theta} \sqrt{2 - \left[\frac{a \exp^{\int \chi(\theta) \mathrm{d}\theta}}{\int_0^{\frac{\pi}{2}} \left[\frac{\exp^{\int \chi(\theta) \mathrm{d}\theta}}{R(\theta)\sin(\theta)} \right] \mathrm{d}\theta} \right]^2}. \tag{4.24}$$

To validate this solution, the same procedure that was implemented for BHL on a hemispheric deformation is implemented, in that the R.H.S. and L.H.S. of (4.3) are found to be equivalent when (4.24) and (4.15) are substituted in. It is worth noting that though the refractive index of the flat Luneburg lens (4.15) does not possess any inherent material singularities, the surface that it is mapped onto does (the point at the top of the cone, located at $\theta = 0$). However, as mentioned earlier this can be dealt with using the technique derived in Horsley *et al.* [71].

4.2.3 Mapping a Luneburg lens onto a hemispheric surface deformation

From the above examples, it is apparent that if a flat lens is to be completely mapped onto a surface, without the aid of the transmutation technique, both the lens and the surface must be void of any material or geometric singularities, respectively. With this in mind, an example is put forward: mapping a flat Luneburg lens onto a hemispheric surface. Using what has already been derived, (4.3) and (4.4) can be recast as

$$\int_0^{\frac{\pi}{2}} n_2(\theta) R_0 \, \mathrm{d}\theta = \int_0^a n_1(r) \mathrm{d}r, \tag{4.25}$$

and

$$2\pi R_0 \sin(\theta) n_2(\theta) = 2\pi r n_1(r), \tag{4.26}$$

respectively, where, R_0 is the radius of the hemispheric deformation as well as the flat lens, and $n_1(r)$ is as defined by (4.15). Expressing $n_1(r)$ as it appears in (4.31) solely in terms of θ produces

$$2\pi R_0 \sin(\theta) n_2(\theta) = 2\pi R_0 \tan\left(\frac{\theta}{2}\right) n_0 \sqrt{2 - \left(\frac{R_0 \tan(\frac{\theta}{2})}{R_0}\right)^2}, \tag{4.27}$$

which after solving for $n_2(\theta)$ simplifies to

$$n_2(\theta) = \frac{n_0\sqrt{1+3\cos(\theta)}}{(1+\cos(\theta))^{\frac{3}{2}}}. \tag{4.28}$$

Letting $n_0 = 1$ and plotting (4.28) produces the curve displayed in Figure 4.5. Inspection

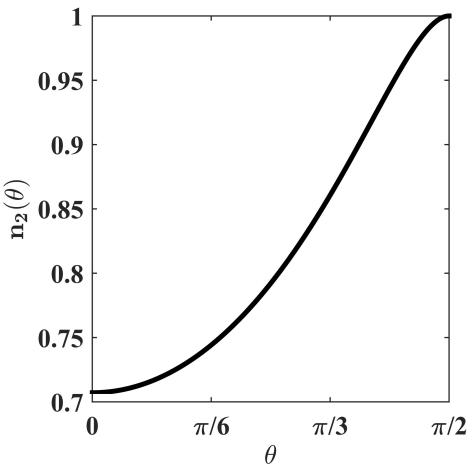

Figure 4.5: Refractive index profile of a Luneburg lens mapped onto a hemisphere as defined by (4.28).

of Figure 4.5 reveals that there are no material singularities within $n_2(\theta)$ as was initially anticipated. Continuing on in this vein another lens, also void of material singularities, is mapped onto a hemispheric surface.

4.2.4 Mapping Maxwell's fish-eye lens onto a hemispheric surface deformation

Following on from the previous idea of avoiding both geometric and material singularities, the mapping of a Maxwell's fish-eye (MFE) [99] lens onto a hemispheric surface

is studied. A flat MFE lens in its simplest sense is a lens that will focus a point source, located on its edge, to a point source radially opposite of it on the same surface. First, the refractive index profile [101] of a flat MFE lens is introduced

$$n_1(r) = \frac{2n_0}{1 + \left(\frac{r}{R_0}\right)^2}, \tag{4.29}$$

where n_0 is the background refractive index and R_0 is the outer radius of the lens. Letting $n_0 = 1$ and plotting (4.29) produces the curve displayed in Figure 4.6. For this

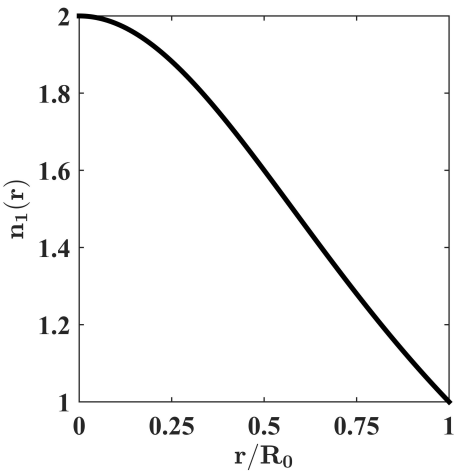

Figure 4.6: Refractive index profile of a flat MFE lens as defined by (4.29).

particular application (4.3) and (4.4) can be recast as

$$\int_0^{\frac{\pi}{2}} n_2(\theta) R_0 \, \mathrm{d}\theta = \int_0^a n_1(r) \mathrm{d}r, \tag{4.30}$$

and

$$2\pi R_0 \sin(\theta) n_2(\theta) = 2\pi r n_1(r), \tag{4.31}$$

where, R_0 is the radius of the hemispheric deformation as well as the flat lens, and $n_1(r)$ is as defined by (4.29). Substituting r as it is defined in (4.10) into (4.31) produces

$$2\pi R_0 \sin(\theta) n_2(\theta) = 2\pi R_0 \tan\left(\frac{\theta}{2}\right) \frac{2n_0}{1 + \tan^2\left(\frac{\theta}{2}\right)}, \tag{4.32}$$

which after simplification and rearrangement reveals an interesting solution of

$$n_2(\theta) = n_0. \tag{4.33}$$

Equation (4.33) implies that a hemispheric deformation of uniform refractive index will behave the same, electrically speaking, as a flat MFE lens. Put another way, the two systems are effectively 'equivalent surfaces'. The idea of equivalent surfaces for lenses is not entirely new, in that it has already been investigated by Berry *et al.* [102] and Tyc *et al.* [78], but with respect to space waves and not surface waves. That being said, a generalized mathematical technique to find the equivalent surface deformation given a flat lens' refractive index profile, is now investigated.

4.2.5 Determining the equivalent surface of a flat lens

Letting the refractive index of the surface deformation be a constant ($n_2 = n_0$) (4.3) and (4.4) are recast as

$$n_0 \int_0^{\frac{\pi}{2}} \sqrt{(R(\theta))^2 + (R'(\theta))^2}\, \mathrm{d}\theta = \int_0^a n_1(r)\mathrm{d}r, \tag{4.34}$$

and

$$2\pi R(\theta)\sin(\theta) n_0 = 2\pi r n_1(r), \tag{4.35}$$

respectively. Simplifying (4.35) and isolating $R(\theta)$ produces

$$R(\theta) = \frac{r n_1(r)}{n_0 \sin(\theta)}. \tag{4.36}$$

Ultimately for $R(\theta)$ to be found explicitly, a relation must be established between r and θ and this is truly the challenging aspect of this particular problem. For example, looking at the previous case of mapping a MFE lens onto a hemispheric deformation, $n_1(r)$ is defined by (4.29) and r by (4.10) which when substituted into (4.36) produces

$$\begin{aligned} R(\theta) &= \frac{R_0 \tan\left(\frac{\theta}{2}\right) 2n_0}{n_0 \sin(\theta)\left(1 + \tan^2\left(\frac{\theta}{2}\right)\right)} \\ &= R_0, \end{aligned} \tag{4.37}$$

which represents a hemispheric deformation of radius R_0 in traditional polar coordinates. This technique can be applied to other flat lenses to deduce their equivalent surfaces as long as the important relationship between r and θ can be established either analytically or numerically. For example, In the case of a flat Luneburg lens, (4.15), the geometric profile of its equivalent surface is found to be that of an ellipsoid (see Figure 4.7).

Returning to the primary goal of mapping flat lenses onto surface deformations,

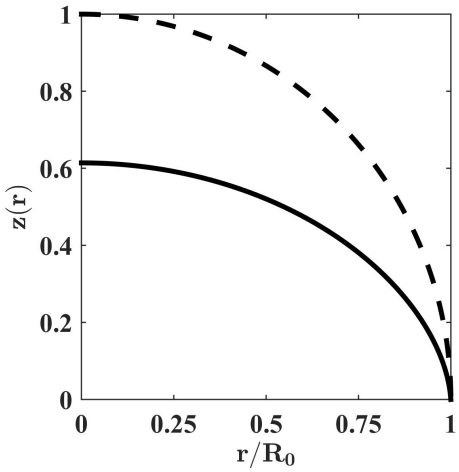

Figure 4.7: Profile of the equivalent surface of a flat Luneburg lens (solid line), and for perspective that of a hemisphere (dashed line).

it is important to keep in mind that there is an inherent geometric feature that can not be captured by (4.3): Gaussian curvature. This was a problem that effected the formalism proposed in Chapter 3 as well and it stems from the fact that it can not deal with the curvature, K, discontinuity between the surface deformation itself (whether it be hemispheric or conic) and the flat approach plane. As mentioned before, it effectively falls to the user to ensure that any surface deformation that is used in this technique possesses a smooth curvature transition from the deformation itself to the flat approach plane. Taking what has already been revealed in Chapter 3, such a surface comes in the form of a 'cosine-shaped' curve that is revolved around the Z-axis. Unfortunately it is not possible to analytically determine $R(\theta)$, which means a numerical version of (4.3) is needed.

4.3 Numerical solution for mapping lenses onto curved surfaces

Starting with (4.3) and a generalized form of (4.4) it is possible to solve for $\mathrm{d}r$ via implicit differentiation as

$$\mathrm{d}r = \frac{1}{n_1(r) + r n_1'(r)} \left[R'(\theta)\sin(\theta) n_2(\theta) + R(\theta)\cos(\theta) n_2(\theta) + R(\theta)\sin(\theta) n_2'(\theta) \right] \mathrm{d}\theta. \quad (4.38)$$

Substituting (4.38) into (4.3) and equating the integrands results in

$$\sqrt{(R(\theta))^2 + (R'(\theta))^2}n_2(\theta)\mathrm{d}\theta = \frac{n_1(r)\left[R'(\theta)\sin(\theta)n_2(\theta) + R(\theta)\cos(\theta)n_2(\theta) + R(\theta)\sin(\theta)n_2'(\theta)\right]\mathrm{d}\theta}{n_1(r) + rn_1'(r)}, \tag{4.39}$$

which after isolating $n_2(\theta)$ and $n_2'(\theta)$ can be recast as

$$\frac{n_2'(\theta)}{n_2(\theta)} = \frac{\left(1 + r\frac{n_1'(r)}{n_1(r)}\right)\sqrt{(R(\theta))^2 + (R'(\theta))^2} - R'(\theta)\sin(\theta) - R(\theta)\cos(\theta)}{R(\theta)\sin(\theta)}. \tag{4.40}$$

Once the necessary change of variable has taken place with respect to r, (4.40) can be solved using the same iterative numeric technique (based on the forward-difference approximation to solve first order differential equations) used in Chapter 3.

Thus far, a generalized analytic approach has been proposed to map RS flat lenses onto RS surface deformations, which is effectively an expansion of a method first introduced in Chapter 3. The technique is proven to be mathematically sound for a number of mappings of lenses (BHL, Luneburg, MFE) onto surface deformations (spherical and conic). In terms of physical limitations, the presence of singularities (owing to the flat lens or the deformation itself) are accounted for and avoided in the final examples to allow for an exact implementation of the proposed solution without having to make an appeal to transmutation [71]. Additionally, a generalized method to solve for the 'equivalent surface' of a flat lens is derived and verified. Lastly, a generalized numeric solution is proposed to allow for the technique to be applied to surfaces whose profile cannot not be explicitly defined in terms of $R(\theta)$. That said, the full-wave EM simulation results for a number of proposed structures that are borne out of these techniques are now studied.

4.4 Simulations

4.4.1 Simulation setup

The behavior of a surface wave is modeled using a parallel plate waveguide method [88], where the refractive index is effectively sandwiched between two perfect electric conductors (PEC) sheets (normal to the Z-axis) that are separated by a distance of $\lambda_0/10$. The remaining edges of the surface are bounded by a λ_0 thick perfectly matched layer (PML). The method of excitation is an electric dipole moment, n_p, with a magni-

tude of 1 $A \cdot m$ in the X, Y and Z-directions, and the mesh is constructed in such a way that no tetrahedron has an edge length greater than $\lambda_0/15$. As was mentioned first in Chapter 3, for the inherent requirements of geometrical optics (GO) to be satisfied, the surface wave lenses themselves must be electrically large (approximately equal to $10\lambda_0$ in diameter for this particular study). Also, just as was the case in the previous chapter, all field results are for the total field (the sum of the incident and scattered fields). Finally, the following COMSOL simulations where first produced by Dr. Rhiannon Mitchell-Thomas (namely, Figure 4.8 and Figure 4.11) and were later adapted by the author for use within this thesis.

4.4.2 Simulation result for surfaces under investigation

The mapping of a flat Luneburg lens (see Figure 4.8) onto a number of different surface deformations is now studied. First, is the flat Luneburg lens itself starting in Figure

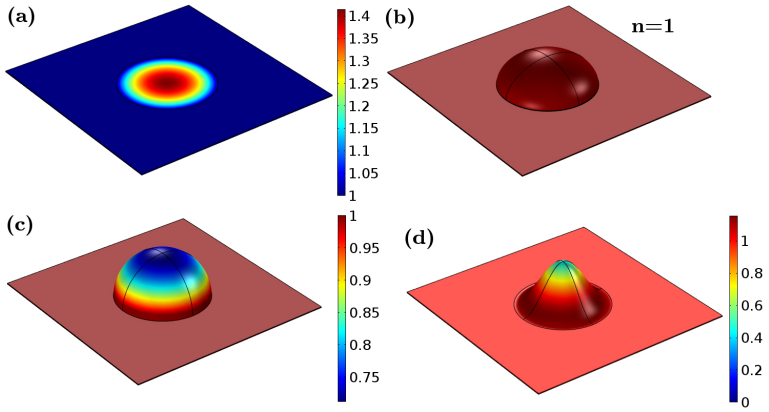

Figure 4.8: Refractive index profiles of a (a) flat Luneburg lens, (b) Luneburg lens' equivalent surface, (c) flat Luneburg lens mapped onto a hemisphere and (d) flat Luneburg lens mapped onto a cosine-shaped deformation.

4.8(a). This will serve as refractive index reference for the other three curved lenses. Next, the refractive index of the equivalent surface of a Luneburg lens is unity, due to the fact that this particular curved surface electrically emulates the material behavior of Figure 4.8(a), but in a purely geometrical manner. Moving on, and using (4.28) as a guide, the result of mapping a flat Luneburg lens profile onto a hemisphere of equivalent radius is displayed in Figure 4.8(c). Finally, in order to map the flat Luneburg lens profile onto a cosine-shaped deformation (whose profile is $z = 1/2\,(\cos(\theta\pi) + 1)$ where $0 \leq \theta \leq 1$ rad.), the numerical approach detailed in (4.40), is utilized and the result is displayed in Figure 4.8(d). Noting, as was mentioned earlier, owing to the fact that neither the surfaces nor the lens under evaluation possess any inherent singularities, the resulting mapped refractive index profiles themselves are also free of material

singularities.

First, following the simulation setup mentioned above the EM behaviour of a plane wave in a flat, empty waveguide is compared to that of a flat waveguide loaded with the Luneburg lens profile (see Figure 4.9). As anticipated, the flat Luneburg lens' refractive

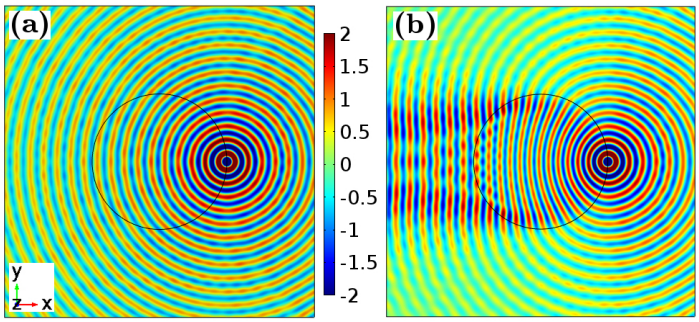

Figure 4.9: Wave behavior of (a) an empty flat surface and (b) a flat surface loaded with a Luneburg lens profile. Both results are for E_z.

index profile effectively converts the cylindrical wave fronts (emanating from the line source) on its right side to a planar wave front on its left side (see Figure 4.9(b)). This specific field pattern will serve as the reference result that the remaining three surface wave lenses will be compared against. Starting with the pattern formed by the Luneburg lens' equivalent surface (see Figure 4.10(b)) the cylindrical-to-planar wave front conversion is witnessed, but with a mild level of shadowing on the left side of Figure 4.10(b), compared to Figure 4.10(a). The reason for this shadowing is the curvature, K, mismatch between the deformation itself and the flat approach plane, where the E-field needs to effectively go from being parallel to the flat plane (whilst inside the curved waveguide) to perpendicular to it (immediately after exiting the curved waveguide), in a very short distance. This same general behavior of cylinderical-to-planar wave front conversion, coupled with a slight level of shadowing, is also displayed for the case of mapping a Luneburg lens onto a hemispheric deformation (see Figure 4.10(c)). Lastly, the results of mapping a Luneburg lens onto a cosine-shaped deformation are analyzed. Here the same wave front conversion is witnessed, but this time the minor level of shadowing is not due to the geometry, but arises as a result of the employed numerical solution. More precisely the surface deformation itself is loaded with the result of a numerical solution that is then acted upon by the FEM mesh of COMSOL 5.0. This means the material implementation is susceptible to numerical approximations imposed by the EM solver during the meshing process. To correct this a finer mesh along the deformation itself along with a finer numerical solution (4.40) is required.

Next, a flat MFE lens is mapped onto three different surfaces. Using (4.3) and (4.40) the required refractive refractive indices along the surfaces as a function of r can

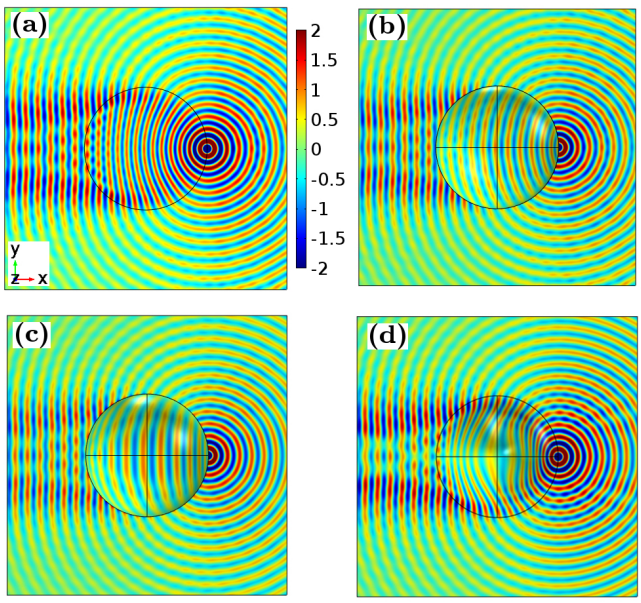

Figure 4.10: Pattern formed by (a) a flat Luneburg lens profile (b) a Luneburg lens' equivalent surface (c) a flat Luneburg lens mapped onto a hemisphere and (d) a flat Luneburg lens mapped onto a cosine-shaped deformation. All results are for E_z.

be determined (see Figure 4.11). Using the same excitation method as was used for the Luneburg lens, the flat MFE lens focuses a dipole moment located on the edge of its surface to a point radially opposite of it on the same surface (see Figure 4.12(b)). This result will serve as the reference pattern for the remaining three surface wave lenses. Starting with the MFE lens' equivalent surface, which is a hemisphere, it is noted that a line-source is 'imaged' on the other side of the hemisphere, with only a slight difference in amplitude of E_z, which is once again caused by how the hemisphere is attached to the flat approach plane (see Figure 4.13(b)). Moving on to the results for mapping a flat MFE lens onto a 'Luneburg surface' (the equivalent surface of a Luneburg lens) the same general pattern behavior is witnessed, but with a minor difference in how the fields are scattered on the right-hand of Figure 4.13(c). Lastly, a flat MFE lens is mapped onto a surface deformation that is void of any curvature mismatch problems, the cosine-deformation, and the greatest level of agreement (relative to the flat MFE results) in terms of both image forming and backscattering is observed. Taking into consideration the full-wave simulation results for the mapping of a Luneburg lens and MFE lens onto different surfaces (Figure 4.10 and Figure 4.13, respectively) using a parallel plate waveguide method, a more realistic device implementation is now investigated.

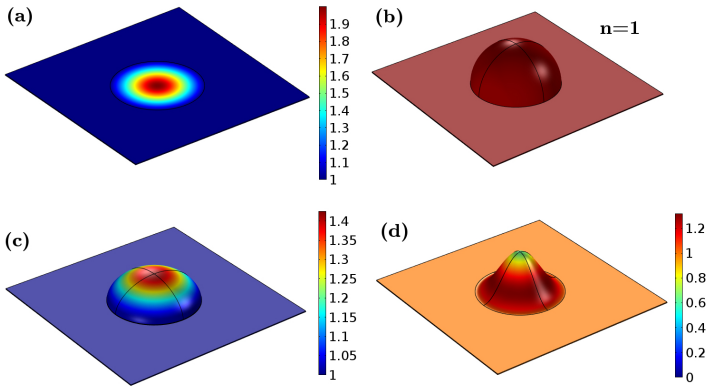

Figure 4.11: Refractive index profiles of a (a) flat MFE lens, (b) MFE lens' equivalent surface, (c) flat MFE lens mapped onto a Luneburg lens' equivalent surface and (d) flat MFE lens mapped onto a cosine-shaped deformation.

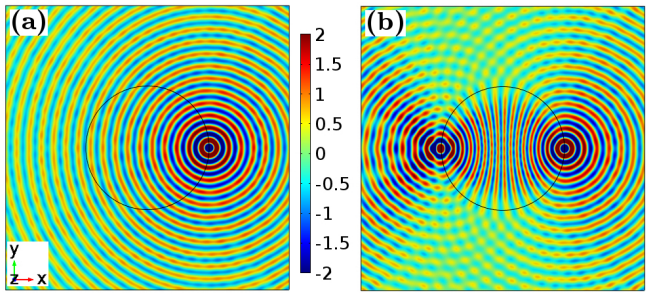

Figure 4.12: Wave behavior of (a) an empty flat surface and (b) a flat MFE lens. Both results are for E_z.

4.5 Realizable rotationally symmetric surface wave lenses

In order to demonstrate the validity of the proposed method for surface waves a 'dielectric-slab-over-a-PEC-ground-plane' implementation is chosen due to its simplistic fabrication requirements. This is different than the approach used in Chapter 3 where the thickness of the overlay was kept constant, and the dielectric constant was varied. In this particular solution, the thickness of a homogeneous dielectric slab is varied in order to obtain the required mode index. This design technique is particularly attractive because it can take advantage of the increasingly accessible technology of 3D printing which has already been used to create a number of EM devices [103–107]. Figure 4.14 illustrates this process where a ε_r of 15 is chosen for the substrate (placed over a metallic surface), where by varying its thickness between 2 and 6 mm, it is possible to obtain mode indices ranging from 1.75 through 3.6 for a central operating frequency of 10 GHz. This is a direct extension of the modal confinement study conducted in Chapter 3. Using this relation, two lenses (MFE lens and a Luneburg lens) are mapped

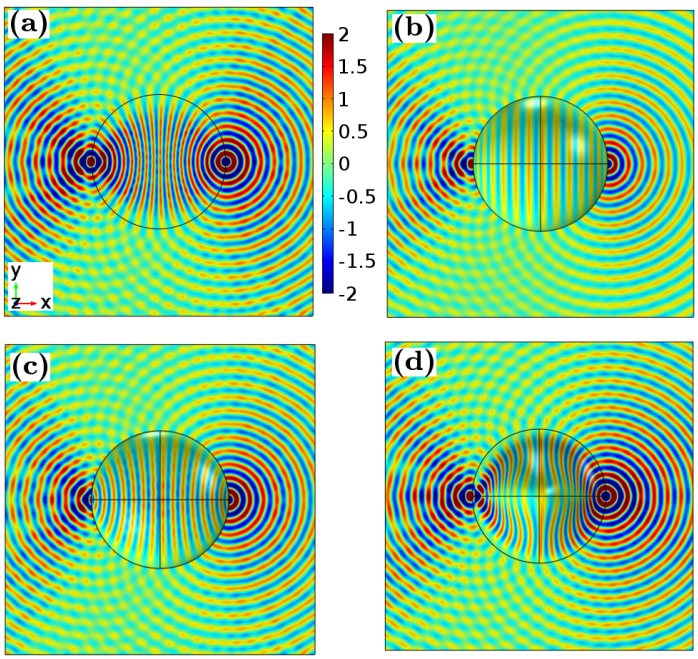

Figure 4.13: Pattern formed by (a) a flat MFE lens (b) a MFE lens' equivalent surface (c) a flat MFE lens mapped onto a 'Luneburg-surface' and (d) a flat MFE lens mapped onto a cosine-shaped deformation. All results are for E_z.

onto the cosine-deformation (see Figure 4.15).

The following CST Microwave Studio simulations were originally conducted by Dr. Oscar Quevedo-Teruel (namely Figure 4.14–4.16) and later adapted by the author for use within this thesis. For these simulations the time domain solver in CST Microwave Studio 2014 [89] is used with the following configuration. First, the mesh is created in such a way to ensure that no cell edge length is greater than $\lambda_0/15$ which helps accurately capture the behvaior the EM fields in the entire model and in turn lead to a convergent solution (which is set to -30 dB). The method of excitation is a discrete port (50 Ω) located on the right edge of both lenses (see Figure 4.16) which is meant to emulate the dipole moment used in the preceding COMSOL simulations. In the case of the Luneburg lens (Figure 4.16(a,c,e)) it is demonstrated, that the device successfully transforms what is effectively a line source (on the right) in to a planar wave on the left. In the case of the MFE lens (Figure 4.16(b,d,f)), the device transforms a point source on its right edge to another point source on its left edge. It is worth noting that though the initial design frequency of the proposed lenses was 10 GHz, a shift in the optimal frequency was ultimately required. The cause of this is that the underlying theory of (4.3) assumes that EM waves are perfectly confined to the surface deformation, but this is no longer strictly the case when the substrate thicknesses are varied (Figure 4.15).

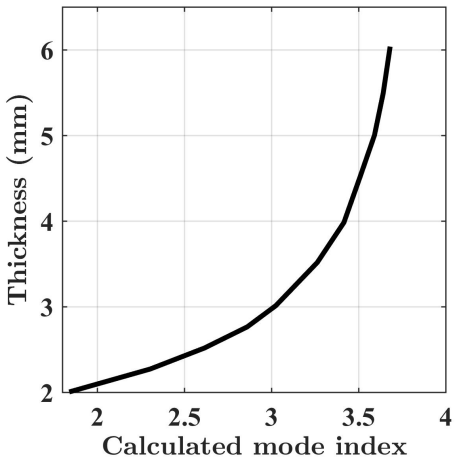

Figure 4.14: Obtained refractive indices for varying thicknesses of a dielectric slab with $\varepsilon_r = 15$, placed over a metallic surface for an operating frequency of 10 GHz.

This designed thickness variation causes the waves propagating farther from the ground plane to have a slightly longer path length than those closer to it, resulting in a minor difference in the optimum frequency of operation. This means that it is important to keep the substrate thickness as thin as possible (relative to design frequency) so as to minimize these deviations.

To gain a better understanding of the level of modal confinement afforded by both of the surface wave lens devices, the cut plane results for the frequencies of interest are included. Starting with Luneburg lens results (see Figure 4.17) we see an excellent level of modal confinement with no waves being radiated into free-space for all frequencies of interest. Figure 4.17 also reveals that the field mapped onto the left side of the surface deformation is of uniform peak distribution and lacking any noticeable interference patterns, which means that the surface wave lens is performing as designed. Moving onto the results for the mapped MFE lens (see Figure 4.18) it is clear that it does not have the same level of modal confinement witnessed in the mapped Luneburg lens. The reason for this is that its material overlay thickness is, on the whole, greater than that of the Luneburg lens design (see Figure 4.15), and this means that it is more difficult to ensure that the modes within the substrate itself behave properly (i.e. the E-field is oriented normal to the PEC ground plane as well as the dielectric-air interface). This does not affect the overall performance of the device however, and it can be seen that a mapping of a line source from the right-edge of the cosine-shaped deformation to its left-edge does occur for all frequencies of interest. Figure 4.17 and Figure 4.18, taken in conjunction with Figure 4.16 demonstrate that the proposed curved surface wave lens design methodology does work for the frequencies of interest.

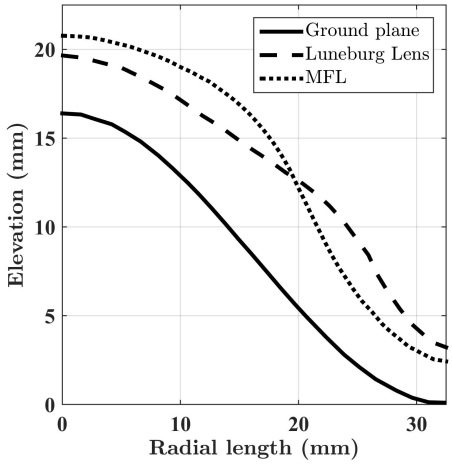

Figure 4.15: Cross-section of the required profile for the MFE and Luneburg lenses placed on a cosine-shaped ground plane.

4.6 Conclusions

In this chapter, a realizable method for mapping flat, isotropic, surface wave lens onto rotationally symmetric surface deformations was proposed. The design recipe first used in Chapter 3 was expanded to allow for the mapping of flat refractive index profiles onto rotationally symmetric surfaces. To demonstrate how one does this, a number of analytical examples were gone through step-by-step which included the mapping of: a black hole lens onto a hemispheric deformation, a Luneburg lens onto a conic deformation, a Luneburg lens onto a hemispheric deformation and a MFE lens onto a hemisphere. The final case of attempting to map a MFE lens onto a hemispheric surfaces lead to the idea of an 'equivalent surface', which in its simplest sense was a curved homogeneous surface that behaved, electrically speaking, in the same fashion as its flat, inhomogeneous analogue. A general method for obtaining the equivalent surface of a flat lens was then derived and the relation between a hemispheric deformation and a MFE lens was used to check its validity. A numerical solution for mapping lenses onto curved surfaces was later derived for instances where $R(\theta)$ of a given rotationally symmetric surface was not expressible in closed-form. Moving on, the parallel plate waveguide simulation technique introduced in Chapter 3 was implemented again. Here the performances of a Luneburg lens and a MFE lens in a number of configurations were investigated using a full-wave electromagnetic solver (COMSOL 5.0). It was demonstrated (as was also witnessed in Chapter 3) that the curvature, K, mismatch between the surface deformation and the flat approach plane lead to undesirable pattern characteristics. Of all the curved surface lens configurations those that

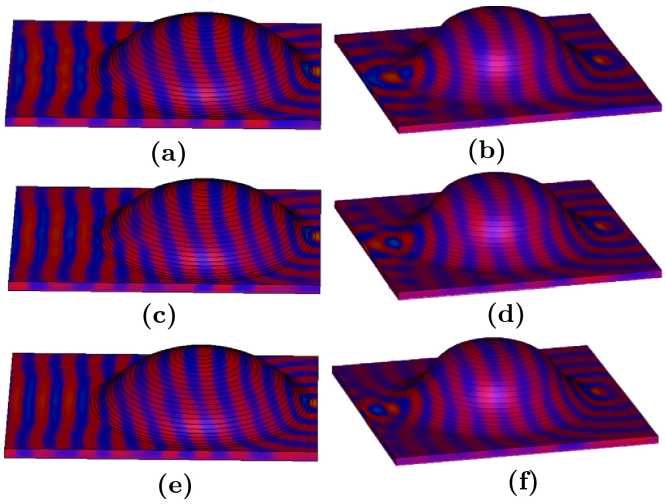

Figure 4.16: Surface wave propagation along the Luneburg lens (a,c,e) and MFE lens (b,d,f) mapped onto a cosine-shaped ground plane. Operating frequencies of (a,b) 10.5 GHz, (c,d) 11 GHz, and (e,f) 11.5 GHz. All results are for E_z.

avoided these curvature discontinuities functioned (emulated the behavior of their flat lens analogues) the best.

Finally, in an attempt to convert the proposed material solution from its parallel plate waveguide form into a real surface wave form, the required material properties for a thin material overlay on a PEC ground plane were determined. Here instead of maintaining the thickness of the material overlay and varying ε_r as was done in Chapter 3, the opposite was done were ε_r is maintained ($\varepsilon_r = 15$) and the thickness of the material overlay was varied according to a calculated relation between material thickness and modal refractive index. This design strategy is particularly interesting as it can be realized via the increasingly accessible rapid fabrication technique of 3D printing. To demonstrate the efficacy of the proposed designs they were simulated using the time domain solver in CST Microwave Studio 2014. Here it was demonstrated that the material realizations of the Luneburg lens and the MFE lens on a cosine-shaped surface deformation functioned properly within a desired frequency band. These simulation results also revealed a good level of modal confinement across said band as well. The curved surface wave lens design recipe described in this chapter is novel in that it calls for the creation of a thin, isotropic, homogeneous material overlay that can be used to control the propagation of surface waves along nearly any smooth rotationally symmetric PEC surface deformation.

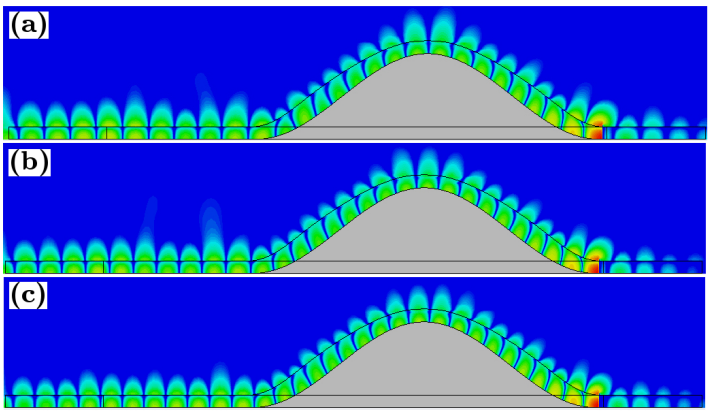

Figure 4.17: Surface wave propagation (from right to left) along a Luneburg lens mapped onto a cosine-shaped surface deformation for (a) 10.5 GHz, (b) 11 GHz and (c) 11.5 GHz. All results are for E_z and are normalized to the source.

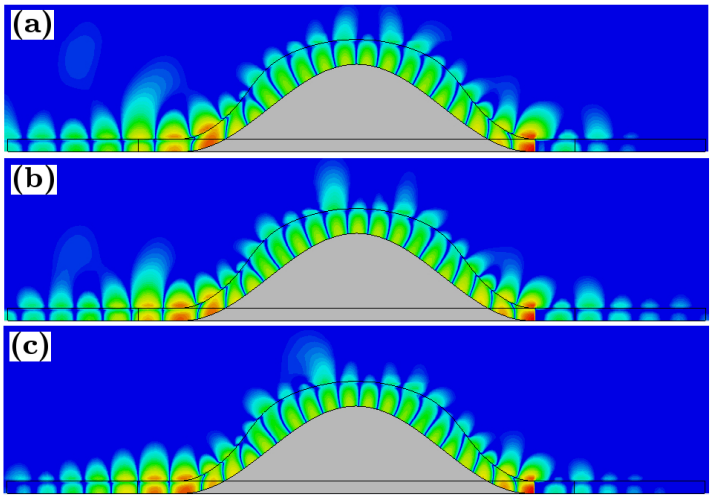

Figure 4.18: Surface wave propagation (from right to left) along a MFE lens mapped onto a cosine-shaped surface deformation for (a) 10.5 GHz, (b) 11 GHz and (c) 11.5 GHz. All results are for E_z and are normalized to the source.

Chapter 5

Cloaking and illusion devices for general surfaces

5.1 Introduction

In this chapter the structural limitations found in Chapter 3 [97] and Chapter 4 (which is a detailed review of [108]), namely the required rotational symmetry of the surface deformation, are addressed. In order to do so, a fundamentally different approach is derived to create both cloaks and illusion devices (devices that make a flat surface behave, electrically speaking, as if it were curved). This technique is closely related to, but independently derived from the approaches that were first proposed by Huidobro *et al.* [43] and Liu *et al.* [80] which collectively form the foundation of transformation plasmonics (TP). As this work deals with the application of TO to surface waves, it also builds upon the works of Kadic *et al.* [44, 82] and Zhu *et al.* [60]. However, what sets the method detailed in this chapter apart is that it explicitly focuses on surface deformations that are not only rotationally asymmetric , but that are also truly general (the meaning of which will become apparent later on in this chapter.)

The outline of this chapter is as follows. First, a new approach for manipulating surface waves along curved (non-Euclidean), rotationally asymmetric surface (RAS) deformations is derived for both cloaks and illusion devices. Afterwards, step-by-step examples of creating a cloak and an illusion device for a RAS deformation are presented. In order to further generalize the utility of this approach, the idea of a 'general surface' is introduced and a numerical technique is proposed to solve for the required material parameters to either create a surface wave cloak or surface wave illusion device. Finally, the same simulation technique used in Chapter 3 is implemented and both the analytically defined and general surfaces are simulated using a full-wave electromagnetic (EM) solver. A quantitative study is also included to further validate the efficacy of

the proposed devices.

5.2 Analytical solutions for general illusion devices and cloaks

As was discussed in Chapter 3 and Chapter 4, a limiting factor of the proposed techniques is that the surface/lens under study must be rotationally symmetric (RS), as detailed in

$$\int_0^{\frac{\pi}{2}} n_c(\theta)\sqrt{(R(\theta))^2+(R'(\theta))^2}\,\mathrm{d}\theta = n\int_0^R \mathrm{d}r, \tag{5.1}$$

and

$$2\pi R(\theta)\sin(\theta)n_c(\theta) = 2\pi r n, \tag{5.2}$$

for cloaking RS deformations, as well as for the mapping of RS lenses onto RS surfaces:

$$\int_0^{\frac{\pi}{2}} n_2(\theta)\sqrt{(R(\theta))^2+(R'(\theta))^2}\,\mathrm{d}\theta = \int_0^a n_1(r)\mathrm{d}r, \tag{5.3}$$

and

$$2\pi R(\theta)\sin(\theta)n_2(\theta) = 2\pi r n_1(r). \tag{5.4}$$

In both instances, the profile (γ) of the surface must be parameterized by a single variable, normally θ. If this limitation is to be overcome then (in the instance of the cloak), (5.1) and (5.2) need to be amended in such a way that they are no longer solely defined by θ in the curved space and r in the flat space (the L.H.S and R.H.S of (5.1) and (5.2) respectively). Additionally, (5.2) would need to be corrected to no longer describe electrical path lengths along a circle, but instead along a more complex space curve, that would ultimately be defined by the asymmetric deformation itself. Cumulatively, these two alterations lead to a more complex (if soluble at all) solution for n_c, and because of this, a different method that does not rely on an application of Fermat's principle, is investigated.

5.2.1 Illusion devices for RAS deformations

In order to deal with the problem of creating surface wave devices for RAS deformations, an entirely new formalism (which was developed in collaboration with Dr. Simon Horsley) for relating two curved spaces in two dimensions is needed. Starting

with the geometrical optics (GO) approximation to Maxwell's equations

$$\nabla \cdot \boldsymbol{\varepsilon} \cdot \underline{E} = 0, \tag{5.5a}$$
$$\nabla \cdot \underline{B} = 0, \tag{5.5b}$$
$$\nabla \times \underline{E} = i\omega \underline{B}, \tag{5.5c}$$
$$\nabla \times \boldsymbol{\mu}^{-1} \cdot \underline{B} = -i\omega \boldsymbol{\varepsilon} \cdot \underline{E}, \tag{5.5d}$$

where ω is frequency, $\boldsymbol{\varepsilon}$ is the permittivity of the media, $\boldsymbol{\mu}$ the permeability of the media, and with the units being chosen in such a way that c, the speed of light, is unity. The electric field $\underline{E}$ is written as

$$\underline{E} = \underline{a} e^{i\underline{S}}, \tag{5.6}$$

and the phase of the wave, $\underline{S}$, is assumed to vary more rapidly than the amplitude, $\underline{a}$, or electrical properties of the medium. These particular conditions ($\nabla \underline{S} \gg \nabla \underline{a}$ and $\nabla \underline{S} \gg \nabla n$) occur when a scatterer (surface deformations in this thesis) is electrically large when compared to the wavelength of the impinging field. The non-trivial solutions to (5.5) are

$$\nabla \underline{S} \cdot \boldsymbol{\varepsilon} \cdot \underline{a} = 0, \tag{5.7a}$$
$$\frac{1}{\omega} \left(\nabla \underline{S} \times \underline{a} \right) e^{i\underline{S}} = \underline{B}, \tag{5.7b}$$
$$\nabla \underline{S} \times \boldsymbol{\mu}^{-1} \cdot \left(\nabla \underline{S} \times \underline{a} \right) + \omega^2 \boldsymbol{\varepsilon} \cdot \underline{a} = 0. \tag{5.7c}$$

Noting that the media under considerations is effectively an electrically thin waveguide, meaning that the fundamental mode is uniform for the cavity, and that $\underline{E}$ is always normal to the top and bottom of the parallel plat waveguide, then $\varepsilon_{zi} = \delta_{zz}$ and $\underline{a} = a\hat{\boldsymbol{z}}$. This then implies that $\nabla \underline{S}$ lies exclusively in the XY-plane, meaning that (5.7c) is now

$$\left(\frac{\partial \underline{S}}{\partial x} \hat{\boldsymbol{x}} + \frac{\partial \underline{S}}{\partial y} \hat{\boldsymbol{y}} \right) \times \left(-\frac{\partial \underline{S}}{\partial x} \boldsymbol{\mu}^{-1} \cdot \hat{\boldsymbol{y}} + \frac{\partial \underline{S}}{\partial y} \boldsymbol{\mu}^{-1} \cdot \hat{\boldsymbol{x}} \right) = -\omega^2 \hat{\boldsymbol{z}}, \tag{5.8}$$

which after a little algebraic manipulation can be recast as

$$\frac{1}{\det\left(\tilde{\boldsymbol{\mu}}\right)} \left[\mu_{xx} \left(\frac{\partial \underline{S}}{\partial x} \right)^2 + 2 \left(\frac{\partial \underline{S}}{\partial x} \right) \left(\frac{\partial \underline{S}}{\partial y} \right) \mu_{xy} + \mu_{yy} \left(\frac{\partial \underline{S}}{\partial y} \right)^2 \right] = \omega^2, \tag{5.9}$$

where

$$\tilde{\boldsymbol{\mu}} = \begin{pmatrix} \mu_{xx} & \mu_{xy} \\ \mu_{yx} & \mu_{yy} \end{pmatrix}, \tag{5.10}$$

and is related to $\boldsymbol{\mu}$ by

$$\boldsymbol{\mu} = \begin{pmatrix} \tilde{\boldsymbol{\mu}} & 0 \\ 0 & 1 \end{pmatrix}. \tag{5.11}$$

In order to relate $\boldsymbol{\mu}$ to the geometry of an general surface deformation (whose parameterization is of the form $x^3 = \sigma(x^1, x^2)$), the eikonal equation in a general 2D coordinate system

$$\tilde{g}^{ln} \frac{\partial S}{\partial x^n} \frac{\partial S}{\partial x^l} = \omega^2 \tag{5.12}$$

is considered. Expanding (5.12) reveals

$$\tilde{g}_{11} \frac{\partial S}{\partial x^1} \frac{\partial S}{\partial x^1} + \tilde{g}_{12} \frac{\partial S}{\partial x^2} \frac{\partial S}{\partial x^1} + \tilde{g}_{21} \frac{\partial S}{\partial x^2} \frac{\partial S}{\partial x^1} + \tilde{g}_{22} \frac{\partial S}{\partial x^2} \frac{\partial S}{\partial x^2}. \tag{5.13}$$

Comparing like coefficients between (5.9) and (5.13), the following relationship between the material properties in the waveguide and an equivalent 2D metric tensor is established

$$\frac{\tilde{\boldsymbol{\mu}}}{\det(\tilde{\boldsymbol{\mu}})} = \tilde{\boldsymbol{g}}^{-1}. \tag{5.14}$$

Taking the determinant of both sides of (5.14) and using the fact that $\tilde{\boldsymbol{\mu}}$ is a 2×2 matrix, the following relation is established

$$\frac{1}{\det(\tilde{\boldsymbol{\mu}})} = \frac{1}{\det(\tilde{\boldsymbol{g}})}, \tag{5.15}$$

which, after rearrangement leads to the sought after equivalence of

$$\tilde{\boldsymbol{\mu}} = \det(\tilde{\boldsymbol{g}})\, \tilde{\boldsymbol{g}}^{-1}. \tag{5.16}$$

When the surface is parameterized in Cartesian 3-space ($z = \sigma(x, y)$), (5.16) appears as

$$\begin{pmatrix} \mu_{xx} & \mu_{xy} \\ \mu_{xy} & \mu_{yy} \end{pmatrix} = \begin{pmatrix} g_{yy} & -g_{xy} \\ -g_{xy} & g_{xx} \end{pmatrix} = \begin{pmatrix} 1 + \left(\frac{\partial \sigma}{\partial y}\right)^2 & -\frac{\partial \sigma}{\partial x}\frac{\partial \sigma}{\partial y} \\ -\frac{\partial \sigma}{\partial x}\frac{\partial \sigma}{\partial y} & 1 + \left(\frac{\partial \sigma}{\partial x}\right)^2 \end{pmatrix}. \tag{5.17}$$

Equation (5.17) in its 3×3 matrix form appears as

$$\begin{pmatrix} \mu_{xx} & \mu_{xy} & \mu_{xz} \\ \mu_{xy} & \mu_{yy} & \mu_{yz} \\ \mu_{xz} & \mu_{zy} & \mu_{zz} \end{pmatrix} = \begin{pmatrix} 1 + \left(\frac{\partial \sigma}{\partial y}\right)^2 & -\frac{\partial \sigma}{\partial x}\frac{\partial \sigma}{\partial y} & 0 \\ -\frac{\partial \sigma}{\partial x}\frac{\partial \sigma}{\partial y} & 1 + \left(\frac{\partial \sigma}{\partial x}\right)^2 & 0 \\ 0 & 0 & 1 \end{pmatrix}. \tag{5.18}$$

Inspection of (5.18) reveals a very important feature that must occur for any flat illusion device to function properly, in that all values of $\left(\frac{\partial \sigma}{\partial y}\right)^2$ and $\left(\frac{\partial \sigma}{\partial x}\right)^2$, and in turn

μ_{xx} and μ_{yy}, respectively, must be greater than or equal to unity, that is assuming the approach plane has a refractive index of unity. Generally speaking, μ_{xx} and μ_{yy} (on the deformation), must be greater than or equal to the material surrounding the deformation (μ_{xx} and μ_{yy} in the flat approach plane). Only once this condition is met, is the flat, loaded illusion device able to correctly emulate its curved unloaded, isotropic analogue, with regards to the behavior of light rays.

To gain an idea of the potential values for $\boldsymbol{\varepsilon}$ and $\boldsymbol{\mu}$ using this technique, a rotationally asymmetric illusion device is considered. An illusion device, as considered herein, is a device that produces the same total scattering characteristics of another surface, though the two surfaces are physically different. More specifically, the total scattering characteristics of a RAS deformation, comprised of $\boldsymbol{\mu} = \boldsymbol{\varepsilon} = 1$ are recreated by a flat, inhomogeneous surface. The archetypal RAS deformation used in this study is the Gaussian deformation

$$\sigma(x, y) = e^{-\left(\alpha x^2 + \beta y^2\right)}, \tag{5.19}$$

where as long as $\alpha \neq \beta$, rotationally asymmetry is assured. In this particular example, $\alpha = 3$ and $\beta = 1$. Substituting (5.19) into (5.17) produces

$$\begin{pmatrix} \mu_{xx} & \mu_{xy} \\ \mu_{xy} & \mu_{yy} \end{pmatrix} = \\ \begin{pmatrix} 1 + \left(\frac{\partial}{\partial y}\left(e^{-\left(3x^2+y^2\right)}\right)\right)^2 & -\frac{\partial}{\partial x}\left(e^{-\left(3x^2+y^2\right)}\right)\frac{\partial}{\partial x}\left(e^{-\left(3x^2+y^2\right)}\right) \\ -\frac{\partial}{\partial x}\left(e^{-\left(3x^2+y^2\right)}\right)\frac{\partial}{\partial x}\left(e^{-\left(3x^2+y^2\right)}\right) & 1 + \left(\frac{\partial}{\partial x}\left(e^{-\left(3x^2+y^2\right)}\right)\right)^2 \end{pmatrix}, \tag{5.20}$$

which reduces to

$$\begin{pmatrix} \mu_{xx} & \mu_{xy} \\ \mu_{xy} & \mu_{yy} \end{pmatrix} = \begin{pmatrix} 1 + 4y^2 e^{-2\left(3x^2+y^2\right)} & -12xye^{-2\left(3x^2+y^2\right)} \\ -12xye^{-2\left(3x^2+y^2\right)} & 1 + 36x^2 e^{-2\left(3x^2+y^2\right)} \end{pmatrix}. \tag{5.21}$$

Finally, substituting (5.21) into (5.11) produces the entire required material tensor for both $\boldsymbol{\mu}$

$$\begin{pmatrix} \mu_{xx} & \mu_{xy} & \mu_{xz} \\ \mu_{xy} & \mu_{yy} & \mu_{yz} \\ \mu_{xz} & \mu_{yz} & \mu_{zz} \end{pmatrix} = \begin{pmatrix} 1 + 4y^2 e^{-2\left(3x^2+y^2\right)} & -12xye^{-2\left(3x^2+y^2\right)} & 0 \\ -12xye^{-2\left(3x^2+y^2\right)} & 1 + 36x^2 e^{-2\left(3x^2+y^2\right)} & 0 \\ 0 & 0 & 1 \end{pmatrix} \tag{5.22}$$

and $\boldsymbol{\varepsilon}$, because as mentioned earlier $\boldsymbol{\mu} = \boldsymbol{\varepsilon}$. Now in order for any potential material loading to have a chance at working as an illusion device, μ_{xx} and μ_{yy} (and by extension, ε_{xx} and ε_{yy}) must be greater than or equal to unity (assuming the deformation is bounded by free-space) for all of x and y, which by inspection of (5.22) proves to be

the case. This of course does not immediately mean that the proposed loading will function properly (for this a full-wave simulation is necessary, as is done later in this chapter), but it does provide a means to rapidly identify any erroneous solutions.

5.2.2 Cloaks for RAS deformations

Starting from (5.5) a scheme for a cloaking a simple parametrically defined surface $z = \sigma(x, y) = \alpha x$ (i.e. a rotated plane) is studied. For this particular system the eikonal equation (5.7c) takes on the form

$$\nabla \underline{S} \cdot \left[\boldsymbol{a} \times \boldsymbol{\mu}^{-1} \times \boldsymbol{a} \right] \cdot \nabla \underline{S} + k_0^2 a^2 = 0, \tag{5.23}$$

where it is assumed that

$$\boldsymbol{\mu} = \begin{pmatrix} 1 & 0 & 0 \\ 0 & \mu_{yy} & 0 \\ 0 & 0 & 1 \end{pmatrix} \rightarrow \boldsymbol{\mu}^{-1} = \begin{pmatrix} 1 & 0 & 0 \\ 0 & \mu_{yy}^{-1} & 0 \\ 0 & 0 & 1 \end{pmatrix} \tag{5.24}$$

and that the electric field polarization is pointing normal to the waveguide,

$$\boldsymbol{a} = a \left(\frac{\hat{\boldsymbol{z}} - \alpha \hat{\boldsymbol{x}}}{\sqrt{1+\alpha^2}} \right), \tag{5.25}$$

where (5.23) then becomes

$$\nabla \underline{S} \cdot \left[\left(\frac{\hat{\boldsymbol{z}} - \alpha \hat{\boldsymbol{x}}}{\sqrt{1+\alpha^2}} \right) \times \boldsymbol{\mu}^{-1} \times \left(\frac{\hat{\boldsymbol{z}} - \alpha \hat{\boldsymbol{x}}}{\sqrt{1+\alpha^2}} \right) \right] \cdot \nabla \underline{S} + k_0^2 = 0. \tag{5.26}$$

Expanding the terms in the square brackets of (5.26) produces

$$\left[\left(\frac{\hat{\boldsymbol{y}}}{\sqrt{1+\alpha^2}} \right) \otimes \hat{\boldsymbol{x}} + \left(\frac{\alpha \hat{\boldsymbol{y}}}{\sqrt{1+\alpha^2}} \right) \otimes \hat{\boldsymbol{z}} - \mu_{yy}^{-1} \left(\frac{\hat{\boldsymbol{x}} + \alpha \hat{\boldsymbol{z}}}{\sqrt{1+\alpha^2}} \right) \otimes \hat{\boldsymbol{y}} \right] \times \left(\frac{\hat{\boldsymbol{z}} - \alpha \hat{\boldsymbol{x}}}{\sqrt{1+\alpha^2}} \right)$$

$$= \left[-\hat{\boldsymbol{y}} \otimes \hat{\boldsymbol{y}} - \mu_{yy}^{-1} \frac{(\hat{\boldsymbol{x}} + \alpha \hat{\boldsymbol{z}}) \otimes (\hat{\boldsymbol{x}} + \alpha \hat{\boldsymbol{z}})}{1+\alpha^2} \right], \tag{5.27}$$

which then means that

$$\left(\frac{\partial \underline{S}}{\partial y} \right)^2 + \frac{1}{\mu_{yy}} \left(\frac{\partial \underline{S}}{\partial n} \right)^2 = k_0^2, \tag{5.28}$$

where $\partial \underline{S} / \partial n$ is the component of the wave vector oriented along the direction of the slope,

$$\frac{\partial \underline{S}}{\partial n} = \hat{\boldsymbol{n}} \cdot \nabla \underline{S}, \tag{5.29}$$

where

$$\hat{\boldsymbol{n}} = \frac{\hat{\boldsymbol{x}} + \alpha\hat{\boldsymbol{z}}}{\sqrt{1+\alpha^2}}, \tag{5.30}$$

which is to be expected because in this example a rotated plane is under investigation. Calculating the elemental distance along the $\hat{\boldsymbol{n}}$-axis, relate to the $\hat{\boldsymbol{x}}$-axis is

$$\mathrm{d}n = \mathrm{d}x^2 + \mathrm{d}z^2 = \sqrt{1+\alpha^2}\mathrm{dx}, \tag{5.31}$$

meaning that (5.28) is

$$\left(\frac{\partial \underline{S}}{\partial y}\right)^2 + \frac{1}{\mu_{yy}\left(1+\alpha^2\right)}\left(\frac{\partial S}{\partial x}\right)^2 = k_0^2. \tag{5.32}$$

Then, assuming that the slope is changing slowly, (5.32) can be generalized to

$$\left(\frac{\partial \underline{S}}{\partial y}\right)^2 + \frac{1}{\mu_{yy}\left(1+\left(\frac{\partial \sigma}{\partial x}\right)^2\right)}\left(\frac{\partial S}{\partial x}\right)^2 = k_0^2, \tag{5.33}$$

which implies that in order to mimic the behavior of a flat plane,

$$\boldsymbol{\mu} = \begin{pmatrix} 1 & 0 & 0 \\ 0 & \frac{1}{1+\left(\frac{\partial \sigma}{\partial x}\right)^2} & 0 \\ 0 & 0 & 1 \end{pmatrix}. \tag{5.34}$$

Finally, allowing σ to be a function of both x and y, and not just a flat plane, (5.34) appears as

$$\boldsymbol{\mu} = \frac{1}{1+(\nabla\sigma)^2}\left[\mathbb{1}_2 + \nabla\sigma \otimes \nabla\sigma\right] + \hat{\boldsymbol{z}} \otimes \hat{\boldsymbol{z}}, \tag{5.35}$$

where $\mathbb{1}_2$ is the identity matrix in two dimensions. After manipulation, the elements of $\boldsymbol{\mu}$ are populated as

$$\begin{pmatrix} \mu_{xx} & \mu_{xy} & \mu_{xz} \\ \mu_{xy} & \mu_{yy} & \mu_{yz} \\ \mu_{xz} & \mu_{yz} & \mu_{zz} \end{pmatrix} = \frac{1}{1+(\nabla\sigma)^2}\begin{pmatrix} 1+\left(\frac{\partial \sigma}{\partial x}\right)^2 & \frac{\partial \sigma}{\partial x}\frac{\partial \sigma}{\partial y} & 0 \\ \frac{\partial \sigma}{\partial x}\frac{\partial \sigma}{\partial y} & 1+\left(\frac{\partial \sigma}{\partial y}\right)^2 & 0 \\ 0 & 0 & 1+(\nabla\sigma)^2 \end{pmatrix}, \tag{5.36}$$

where just as before in the case of the illusion device $\boldsymbol{\mu} = \boldsymbol{\varepsilon}$. Using (5.19) as a candidate surface (5.36) is populated as

$$\begin{pmatrix} \mu_{xx} & \mu_{xy} & \mu_{xz} \\ \mu_{xy} & \mu_{yy} & \mu_{yz} \\ \mu_{xz} & \mu_{yz} & \mu_{zz} \end{pmatrix} = \\ \frac{1}{1+(\nabla\sigma)^2} \begin{pmatrix} 1+36x^2e^{-2\left(3x^2+y^2\right)} & 12xye^{-2\left(3x^2+y^2\right)} & 0 \\ 12xye^{-2\left(3x^2+y^2\right)} & 1+4y^2e^{-2\left(3x^2+y^2\right)} & 0 \\ 0 & 0 & 1+(\nabla\sigma)^2 \end{pmatrix}, \tag{5.37}$$

where

$$\nabla\sigma = -2e^{-\left(3x^2+y^2\right)}\left(3x+y\right). \tag{5.38}$$

A rapid validity check of the proposed material loading for a cloaking device, μ_{xx} and μ_{yy} must be less than or equal to unity (or more generally less than or equal to value of the background material surrounding the surface deformation itself), which by inspection of (5.37) is the case.

5.3 Numerical solutions for general illusion devices and cloaks

5.3.1 CAD surfaces

As mentioned earlier, the techniques from preceding chapters implicitly relied on knowing the profile of the surface deformation in some parametric form. In the case of using a generalization of Fermat's principle, this required that the space curve γ, which was then swept around a central axis to produce a rotationally symmetric surface deformation, to be known a priori either in the form of $\gamma(\theta)$ or $\gamma(r)$, where θ and r, represent the polar angle and radial length, respectively. This necessity does not appear in the technique proposed in this chapter where a two-dimensional surface deformation is defined via a parameterization of $\sigma(x, y)$ (when operating in Cartesian coordinates) which means any smooth surface that can be parameterized in this form, can in theory be operated upon. This is particularly useful if the surface is not explicitly given is the form of $z = \sigma(x, y)$ but is instead in the form of an appropriately meshed surface created using computer-aided design (CAD). With this in mind, a generalized numeric technique is developed and tested to take advantage of this feature.

Using the central difference approximation method to solve for a partial derivative,

the metric tensor component g_{xx} can be solved via

$$g_{xx}(i,j) = 1 + \left(\frac{\partial \sigma_{i,j}}{\partial x_{i,j}}\right)^2 \tag{5.39a}$$

$$= 1 + \left(\frac{\partial z_{i,j}}{\partial x_{i,j}}\right)^2 \tag{5.39b}$$

$$\approx 1 + \left(\frac{z_{i+1,j} - z_{i-1,j}}{x_{i+1,j} - x_{i-1,j}}\right)^2 + O\left((\Delta x)^3\right). \tag{5.39c}$$

Similarly, g_{xy} and g_{yy} are calculated numerically as

$$g_{yy} \approx 1 + \left(\frac{z_{i,j+1} - z_{i,j-1}}{x_{i,j+1} - x_{i,j-1}}\right)^2 + O\left((\Delta x)^3\right), \tag{5.40a}$$

$$g_{xy} \approx \left(\frac{z_{i+1,j} - z_{i-1,j}}{x_{i+1,j} - x_{i-1,j}}\right)\left(\frac{z_{i,j+1} - z_{i,j-1}}{x_{i,j+1} - x_{i,j-1}}\right) + O\left((\Delta x)^3\right). \tag{5.40b}$$

where O is the truncation error, which can be made arbitrarily small by limiting the distance between points, Δx, of a mesh (or equivalently increasing the number of points that constitute a mesh), as is explored in detail later in the chapter.

A traditional finite-difference mesh in a generalized coordinate system (x^1, x^2, x^3), with linear spacing between points in the x^1 and x^2 directions is displayed in Figure 5.1. The Cartesian coordinate system (out of convenience and utility), is primarily utilized

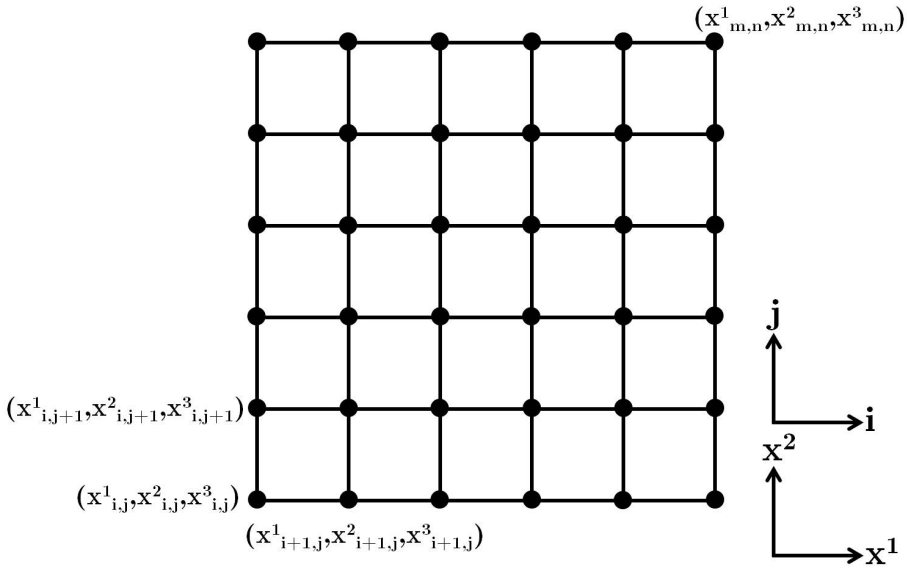

Figure 5.1: A general coordinate system and indexing scheme for use in conjunction with the finite-difference method.

in this study, in which case Figure 5.1 takes on the familiar form displayed in Figure 5.2.

Inspection of the central difference approximation found in (5.39c) reveals that in order

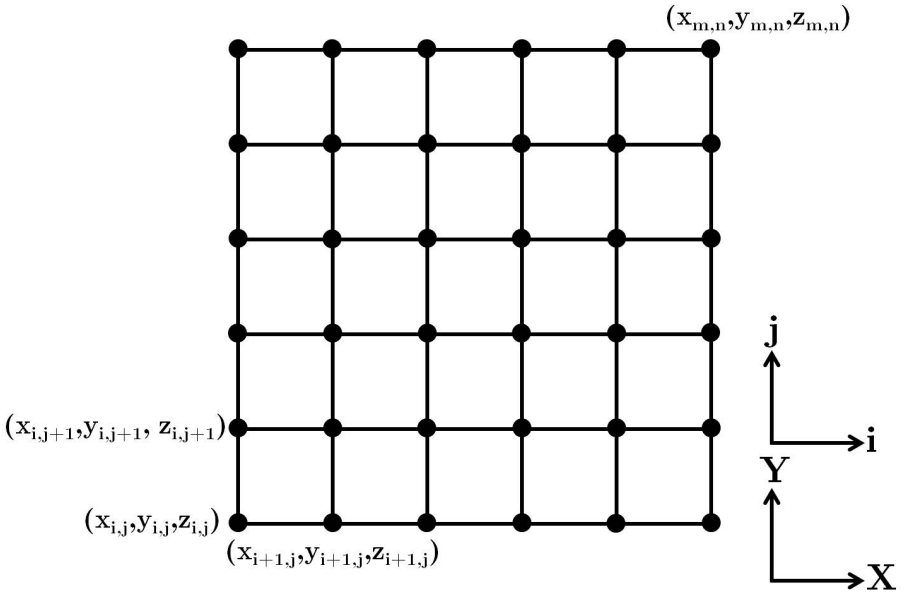

Figure 5.2: Cartesian coordinate system and indexing scheme for use in conjunction with the finite-difference method.

for a derivative to be determined at a point $p(i, j)$, information about a point to the 'left', $p(i-1, j)$ and 'right', $p(i+1, j)$ of it must be known a priori. The same restriction applies to (5.40a) with g_{yy}, but with respect to having to know information about a point 'above', and 'below' $p(i, j)$, which are $p(i, j+1)$ and $p(i, j-1)$, respectively. The cumulative effect of this is that at the boundaries of a mesh, the derivatives can not be directly calculated. These point are colored red in Figure 5.3.

This problem can be solved by extrapolating new mesh points outside of a given mesh. For example, if a researcher is working with MATLAB R2015a [84], this can be accomplished by using fnxtr(f,o) [109]. This function returns the spline (a continuous curve that passes through a set of points and has a certain number of continuous derivatives) that agrees with the spline of 'f' (the function that one wants to extrapolate across) and is a polynomial of order, 'o' outside of the domain of 'f'. However, as one would imagine, this process has the potential to be computationally intensive if the mesh is very large (e.g. many orders of magnitude larger than Figure 5.4). Ultimately this problem can be dealt with much more easily by simply ensuring that any surface deformation that is studied is effectively 'centered' in a mesh. By ensuring that the deformation (the part of the surface where the Gaussian curvature, $K \neq 0$,) does not occur at the edges of a mesh, one can confidently assume that at the edges, solutions to the partial derivatives are approximately equivalent among neighboring points (or

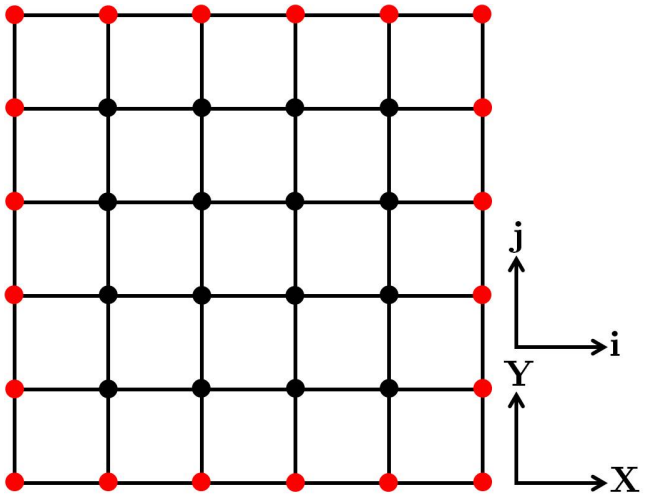

Figure 5.3: Structured mesh with red colored points indicating locations on the mesh where it is not possible to directly implement the central difference approximation to determine a partial derivative.

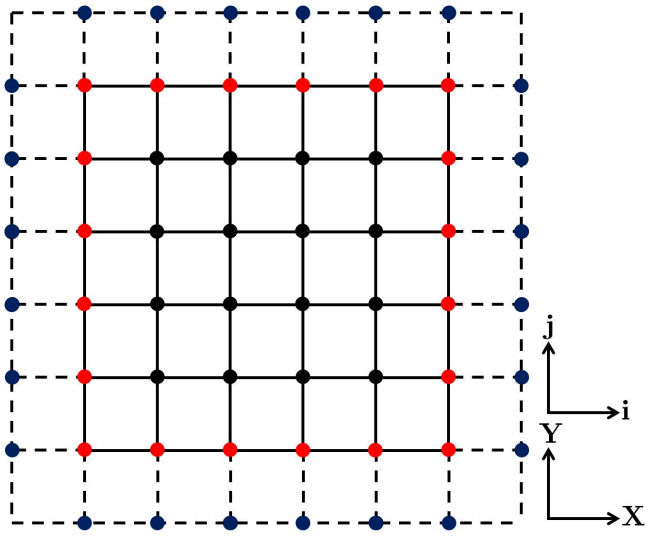

Figure 5.4: Creation of virtual points (blue) in order to evaluate partial derivatives at boundary points of a mesh (red).

are more precisely approximately zero as they are on a flat plane). In doing so, the outermost edges can essentially be ignored as they have no direct impact on calculations on the curved part of the surface - the area of the device that will have a non-trivial material solution. In short, by positioning the deformation of a surface in the center of a mesh, the central difference approximation can be directly implemented without any loss in precision to the solution of partial derivatives, and in turn material parameters in the curved region of interest.

Returning to the question of approximation error, O, the test surface from before, $\sigma(x,y) = e^{-\left(\alpha x^2+\beta y^2\right)}$, is considered, where $\alpha = 3$ and $\beta = 1$. In particular, two different space curves, both of which reside on the surface $\sigma(x,y)$ are studied. The first, is $\sigma(x,y_0)$ and the second is $\sigma(x_0,y)$ where $x_0 = y_0 = 0$, $-3 \leq x \leq 3$ and $-3 \leq y \leq 3$. The reason -3 and 3 are chosen to be the lower and upper bounds, respectively for both x and y, is because at these points, $\frac{\partial\sigma(x,y)}{\partial x} = \frac{\partial\sigma(x,y)}{\partial y} \approx 0$, which means that the deformation is effectively centered in the middle of this ad hoc one-dimensional mesh and there is no need to generate the virtual points seen in Figure 5.4. Figure 5.5 displays the spaces curves $\sigma(x,0)$ and $\sigma(0,y)$ as well as their analytically

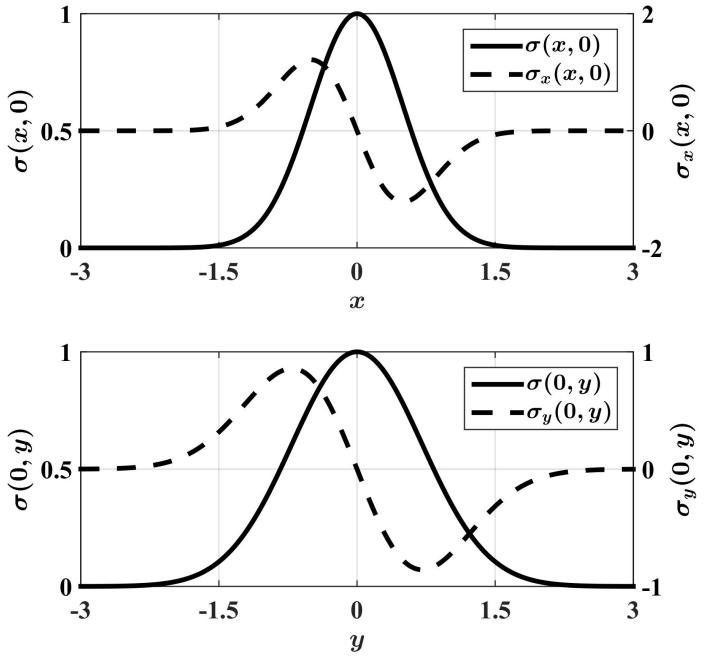

Figure 5.5: $\sigma(x,0)$ and analytically determined $\sigma_x(x,0)$ (top). $\sigma(0,y)$ and analytically determined $\sigma_y(0,y)$ (bottom).

determined partial derivatives. In an attempt to quantify the approximation error, O, the absolute error is used, which is defined as

$$\mathrm{AE} = |\alpha_0 - \alpha|\,, \tag{5.41}$$

where in this context, α_0 is the numerically calculated partial derivative and α is the analytically calculated partial derivative. The main reason this method is employed

over say the traditional relative error calculation,

$$\delta\alpha = \frac{\mathrm{AE}}{\alpha}, \tag{5.42}$$

is because the surfaces investigated in this study have partial derivatives that will evaluate to zero or numbers that are infinitesimally small at a majority of points, and owing to α existing in the denominator of (5.42), this will inevitably lead to undefined solutions or inaccurately large error levels. The distribution of the peaks for σ_x and σ_y

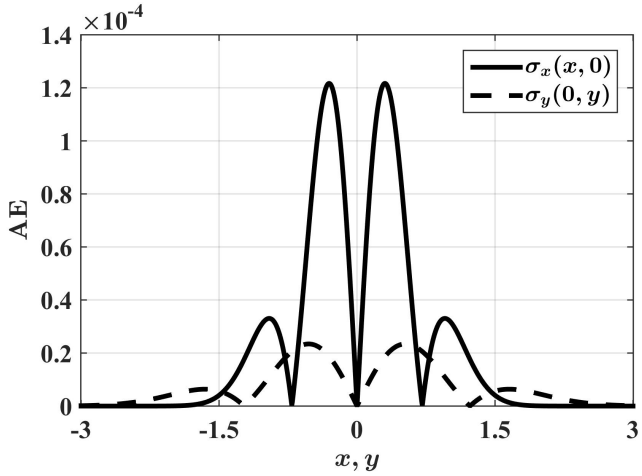

Figure 5.6: Absolute error of numerically determined $\sigma_x(x,0)$ and $\sigma_y(0,y)$ for $n_p = 999$.

in Figure 5.6 are a consequence of the fact that x and y are linearly spaced, and in turn the numerically determined partial derivatives will possess higher levels of disagreement in area with much greater slopes. Ultimately however, as was pointed out earlier, the approximation error, O, can be made arbitrarily small by decreasing the spacing between x and y, as is demonstrated in Figure 5.7. Here a different metric is used to gauge the level of error found in each sampling case: the mean absolute error, which is appears as

$$\mathrm{MAE} = \frac{1}{n_p}\sum_{i=1}^{n_p} \left|\alpha_{0,i} - \alpha_i\right|, \tag{5.43}$$

where n_p is the number of sampling points used in the calculation. Worth mentioning from an applications perspective as well, is that ultimately, at least to date, the vast majority of manufacturable ε_r and μ_r values are only precise to within a tenth of a whole relative unit, which means such small approximation errors from above would not manifest themselves in any final, fabricated design.

As the whole purpose of this chapter is to study two-dimensional surfaces and cal-

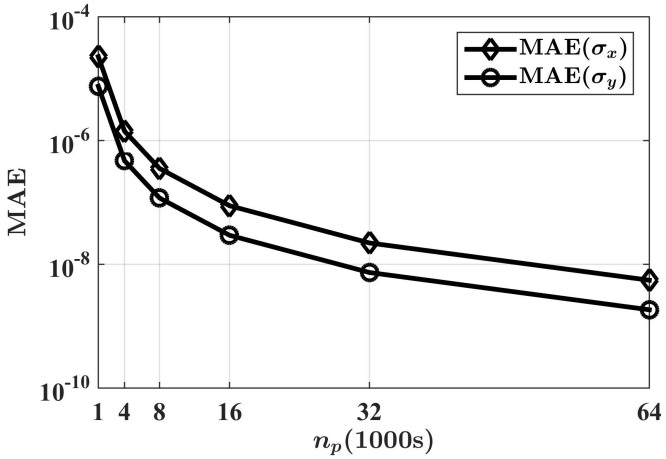

Figure 5.7: Mean absolute error (MAE) for σ_x and σ_y as a function of n_p.

culate their required materials properties (either to create a cloak or an illusion device), what follows is a validation study involving the aforementioned numerical approach as it relates to a shoe surface (see Figure 5.9). First a suitable mesh is generated for this surface using a commercially available mesh generation tool Pointwise [110]. Pointwise, in a basic sense, takes the .stl file (the CAD file of the surface of interest), and creates a suitable structured mesh based upon conditions set by the user including the size of the mesh, mesh cell anisotropy and point placement along the bounding edges of the surface. These inputs are then treated as the initial conditions to a hyperbolic partial differential equation (which is dependent upon the surface encapsulated in the aforementioned .stl file) that Pointwise solves for, the result of which is a structured mesh. The result of meshing an asymmetric Gaussian deformation is displayed in Figure 5.8. Worth highlighting is that unlike other previous techniques that used Pointwise (or

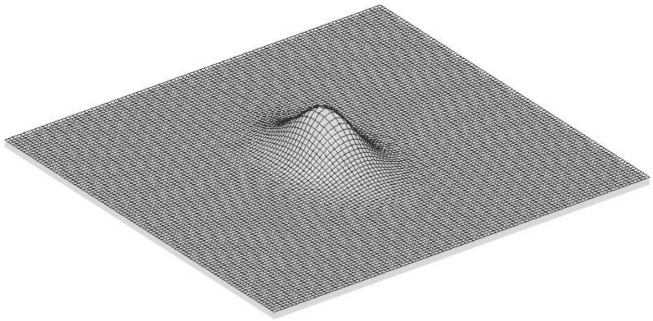

Figure 5.8: Structured mesh placed on top of an asymmetric Gaussian deformation in Pointwise.

other mesh generating software) as a means of implementing a quasi-conformal trans-

formation optics, namely those of Tang [46] and Bao [47], Pointwise in this case is simply populating a given surface with points, and not trying to enforce any conformality.

In order to make sure that the proposed central difference approximation method is behaving correctly a shoe surface [6, 111]

$$z = \sigma(x, y) = \frac{1}{3}x^3 - \frac{1}{2}y^2, \tag{5.44}$$

is studied (see Figure 5.9). The metric tensor components g_{ij} along (5.44) can be

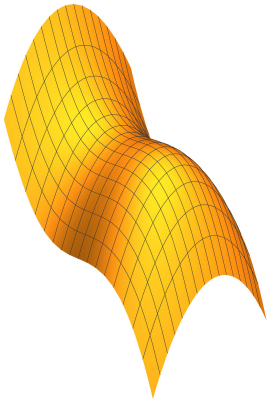

Figure 5.9: Non-Euclidean test surface (shoe surface) used to validate numeric solution.

analytically determined as

$$\begin{aligned} g_{xx} &= 1 + \left(\frac{\partial \sigma}{\partial x}\right)^2 = 1 + x^4, \\ g_{xy} &= \frac{\partial \sigma}{\partial x}\frac{\partial \sigma}{\partial y} = -x^2 y, \\ g_{yy} &= 1 + \left(\frac{\partial \sigma}{\partial y}\right)^2 = 1 + y^2, \end{aligned} \tag{5.45}$$

which effectively constitute the elements of $\tilde{\boldsymbol{\mu}}$ from the previous derivation. The equations in (5.45) provide the 'true' values for the metric tensor components against which the numerically determined values (which will invariably have some level of truncation error) are compared. Here once again, the mean absolute error (MAE) will gauge the level of agreement between the two solutions.

In this study the MAE is calculated for seven different patch configurations with the mesh fineness ranging from $2^8 = 256$ patches (16 x 16 mesh) to $2^{20} = 1048576$ patches (1024 x 1024 mesh) (see Figure 5.10). The main feature that stands out in Figure 5.10 is that the MAE for g_{xx} is the largest (relative to MAE for g_{xy} and g_{yy})

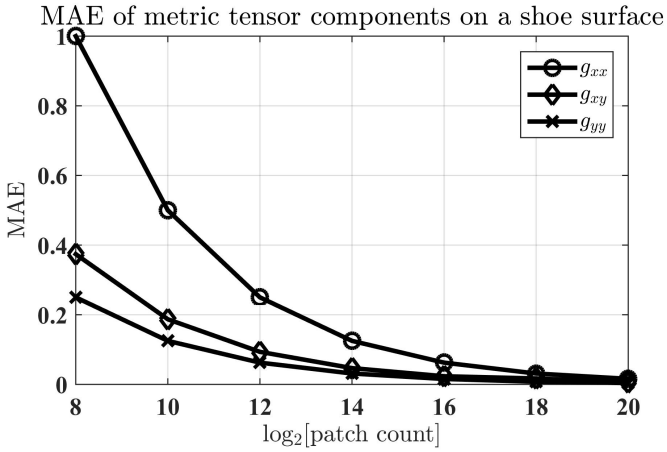

Figure 5.10: MAE study for numerically determining the metric tensor components on a shoe surface.

for all patch counts. The reason for this is because g_{xx} varies the greatest along the shoe surface (see g_{xx} in (5.45)). This inverse relationship between the range of a metric tensor components and its MAE value is demonstrated also by the results for g_{xy} and g_{yy} in Figure 5.10. Ultimately, Figure 5.10 indicates that it is not until around a patch count of 2^{16} (256 x 256 mesh), that there is a negligible difference between the MAE of g_{xx}, g_{xy} and g_{yy}. This minimum meshing value is a very important parameter to keep in mind as all three components play a role in the material solutions for the cloaking and illusion devices found in this chapter. That said, one is not solely looking to make the MAE of a single metric tensor component as close to zero as possible, but also to make sure that the MAE of all of the metric tensor components are as close to zero as possible. Numerically calculating g_{xx}, g_{xy} and g_{yy} using a central difference approximation method operating on a 256 x 256 mesh generated in Pointwise produces the contour plots seen in Figure 5.11–5.13. Inspection of (5.45) as it relates to g_{xx}, reveals that as expected all values in Figure 5.11 are greater than or equal to unity. Also, from Figure 5.11 it is apparent that g_{xx} is solely a function of x as is predicted by the analytic solution for g_{xx} in (5.45). Moving onto g_{xy} as it appears in (5.45) one expects to see a negative value for g_{xy} when $y > 0$, and a positive one for when $y > 0$, as is reproduced in Figure 5.12. Moreover, it is possible to quickly validate that the correct range of values for g_{xy} are being calculated for numerically by substituting $x = 2$ and $y = 2$ into g_{xy} in (5.45) and noting that in fact the minimal value of -8 is produced (see Figure 5.12). Similar agreement can be established between g_{yy} in (5.45) and the numerically calculated value for g_{yy} that is displayed in Figure 5.13. Once again all values for g_{yy} are greater than or equal to unity and as called for in (5.45), g_{yy} is purely a function of y. Having demonstrated that the proposed numerical method

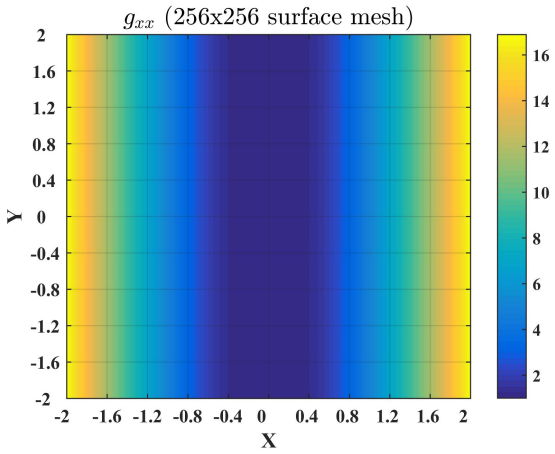

Figure 5.11: Numerically calculated g_{xx} for a shoe surface.

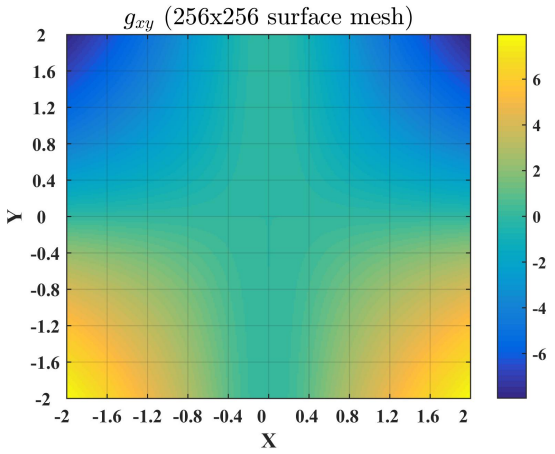

Figure 5.12: Numerically calculated g_{xy} for a shoe surface.

can correctly solve the metric tensor on a surface, it will be used later in this chapter to create an illusion device for a far more complex structure.

5.4 Simulations

5.4.1 Simulation setup

To simulate the proposed rotationally asymmetric cloaking and illusion devices, a full-wave electromagnetic solver (COMSOL 5.0 [112]) is used. The behavior of a surface wave is modeled using a parallel plate waveguide method [88], where the prescribed $\boldsymbol{\varepsilon_r}$ and $\boldsymbol{\mu_r}$ are sandwiched between two perfect electric conductor (PEC) sheets (normal to the Z-axis) that are separated by a distance of $\lambda_0/10$. The remaining edges of the surface are bounded by a perfectly matched layer (PML) that is λ_0 thick. The method

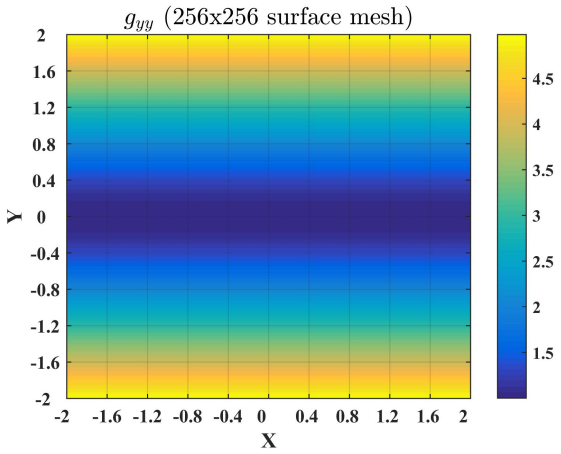

Figure 5.13: Numerically calculated g_{yy} for a shoe surface.

of excitation is a plane wave (originating from one of the bounding edges) with $\underline{E}$ (with an amplitude of 1 V/m) oriented along the Z-direction and $\underline{k}$ oriented in the XY-plane. Also, the mesh is configured in such a way that no tetrahedral edge length is greater than $\lambda_0/15$ so as to ensure the likelihood of a convergent solution. As anticipated, due to the inherent requirements of GO to be satisfied, the following surface wave cloaks and illusion devices themselves must be electrically large.

5.4.2 Simulation results for surfaces under investigation

Having constructed a relationship between the constitutive parameters of a flat surface, and an equivalent deformed surface, the proposed illusion device is tested. The first surface is a skewed Gaussian deformation (see Figure 5.14(a)) that has a height profile describe by $z_1 = \sigma(x, y) = e^{-\left(3x^2+y^2\right)}$ that acts as the archetypal, rotationally asymmetric surface in this study. In terms of size, the footprint of the surface deformation (the area of the surface where $K \neq 0$) is approximately $10\lambda_0 \times 20\lambda_0 \times 5\lambda_0$ in the X, Y and Z-directions, respectively. Applying the equivalence given in (5.17), produces the required $\boldsymbol{\varepsilon_r}$ and $\boldsymbol{\mu_r}$ (see Figure 5.14(b-d)) that will make a flat waveguide loaded with an anisotropic material appear (electrically speaking) to a plane wave as if it were in fact a curved, empty waveguide with a profile described by z_1. In Figure 5.15(a-d) the excellent agreement in terms of scattering for the curved and flat surfaces is displayed. Though traditionally more emphasis is placed on the forward-scattering behavior with regards to illusion devices, the near-perfect reproduction of backscattering should not be overlooked if for no other reason, than as a performance metric to gauge the fidelity of the proposed technique.

In order to fully appreciate the illusion device's ability to reproduce the forward-

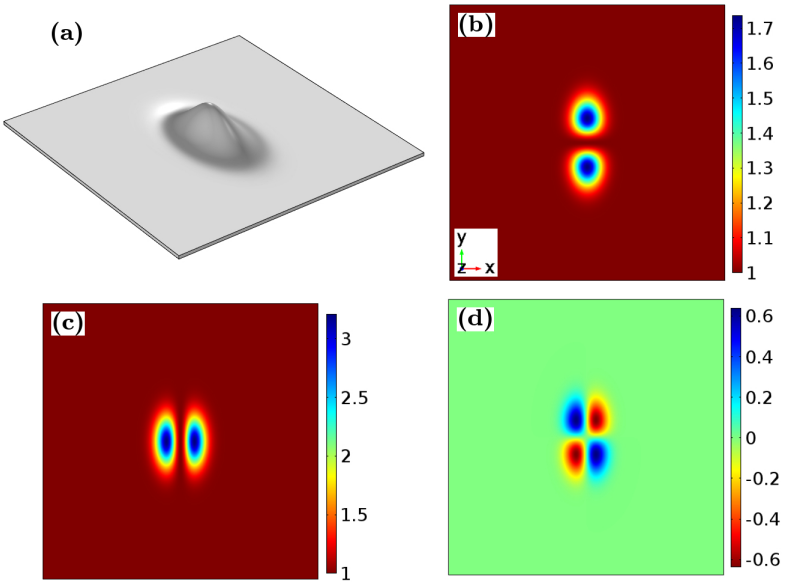

Figure 5.14: (a) Isometric view of $z_1 = \sigma_1(x, y) = e^{-\left(3x^2+y^2\right)}$. (b) $\varepsilon_{r,xx}, \mu_{r,xx}$. (c) $\varepsilon_{r,yy}, \mu_{r,yy}$. (d) $\varepsilon_{r,xy}, \mu_{r,xy}$.

scattering characterstics of its curved analogue, Figure 5.15 is supplemented with a quantitative study. To do so, two probe lines (see Figure 5.16(a)), each $15\lambda_0$ in length are centered $15\lambda_0$ away from the origin of the deformation, and oriented parallel to the incident plane wave. In the first instance, θ_i is set to zero, and the amplitude of E_z along the red probe line is plotted (Figure 5.17). Here exceptional agreement between the curved surface and the illusion device is displayed. Next, the angle of incidence of the surface wave is set to $\theta_i = \frac{\pi}{4}$ and the amplitude of E_z along the blue probe line (Figure 5.16(a)) is recorded. Once again, an excellent level of agreement between the curved surface and the illusion device (Figure 5.18)is demonstrated. This behavior is exhibited for all angles of incidence, which means that this illusion device is omnidirectional. Taking these results, and those in Figure 5.15 into consideration, it is apparent that the illusion device faithfully recreates the surface wave scattering characteristics of its curved analogue.

Next, a CAD surface that lacks any rotational or axial symmetry (see Figure 5.19(a)) is considered, and the numerical solution described in the previous section is used to solve for $\boldsymbol{\mu_r}$ and $\boldsymbol{\varepsilon_r}$. As was the case of the previous illusion device, once the flat, metallic surface is loaded with the prescribed material properties (see Figure 5.19(b-d)) it effectively reproduces both the forward and backscattering characteristics of its empty, curved analogue (see Figure 5.20 and Figure 5.21). The simulation results displayed in Figure 5.20 and Figure 5.21 are particularly important because not only do they show

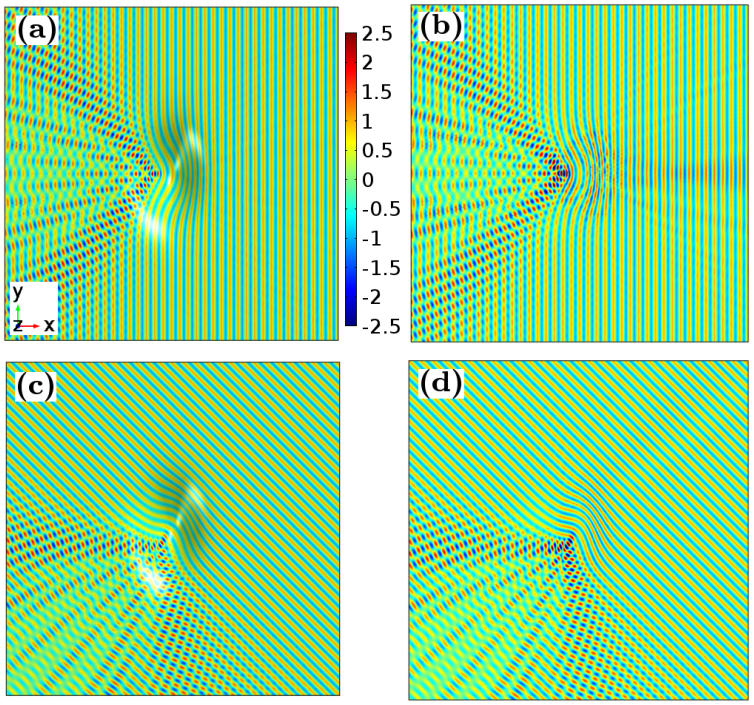

Figure 5.15: Plane wave propagating from right to left ($\theta_i = 0$), through a curved isotropic medium (a) and a flat anisotropic medium (b). Plane wave propagating at $\theta_i = \frac{\pi}{4}$ through a curved isotropic medium (c) and a flat anisotropic medium (d). All results are for E_z.

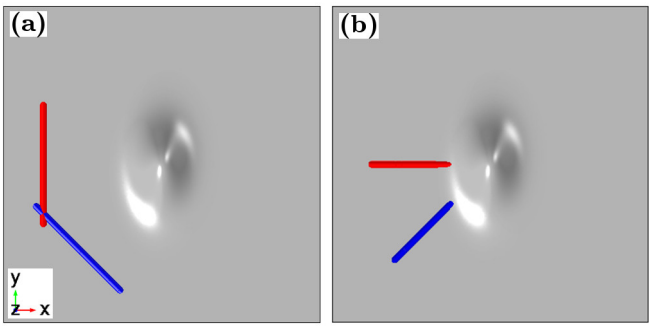

Figure 5.16: Probe line locations for illusion device (a) and cloaking device (b) validation. The red lines are meant to validate performance for $\theta_i = 0$, and the blue lines for $\theta_i = \frac{\pi}{4}$.

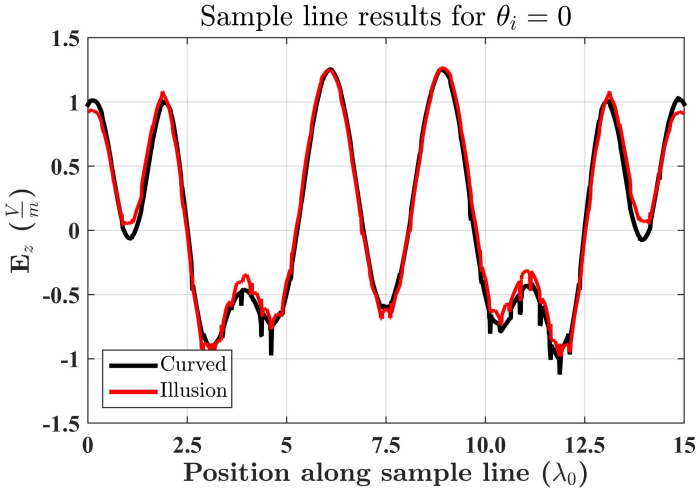

Figure 5.17: Quantitative validation of proposed illusion device for $\theta_i = 0$.

that an illusion device can create the scattering characteristics of a truly arbitrarily curved surface, but that it can do so for multiple angles of incidence. In conclusion, according to the above simulations it is apparent that it is possible to create illusion devices for both simple singular rotationally asymmetric surface deformations as well as CAD defined surfaces. In terms of general applications, an electromagnetic illusion device would prove useful if a designer needed to recreate the scattering characteristics of a curved surface whilst simultaneously trying to minimize (flatten) the space that which this device occupied, as might occur in the design of a surface wave antenna. Moving on from the illusion device, the simulation results for the proposed cloaking device are now studied.

The test surface used to validate the proposed cloaking formalism (5.36) is once again an asymmetric Gaussian deformation (Figure 5.22(a)) whose profile is identical to the one used in the illusion device example. The material parameters to cloak such

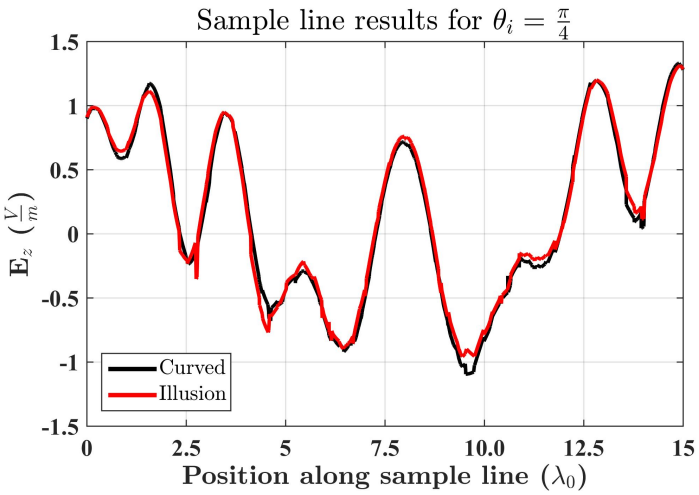

Figure 5.18: Quantitative validation of proposed illusion device for $\theta_i = \frac{\pi}{4}$.

a deformation, appear in Figure 5.22(b-d). As previously anticipated the prescribed $\boldsymbol{\varepsilon_r}$ and $\boldsymbol{\mu_r}$ are less than unity, which allow the phase fronts to traverse the deformation at a faster rate than their flat-space analogues, thereby giving rise to planar wave fronts in the forward scattering region. The method of excitation and simulation for the cloak is identical to that of the illusion device, the results of which can be seen in Figure 5.23(a-d). Initially, a plane wave is launched across the deformation at $\theta_i = 0$, for both the 'uncloaked' (see Figure 5.23(a)) and the 'cloaked' (see Figure 5.23(b)) case. As desired, the cloak completely renders the deformation electrically flat as is demonstrated by the total scattering (both forward and backward) in Figure 5.23(b). This process is repeated for $\theta_i = \frac{\pi}{4}$ (see Figure 5.23 (c,d)), and once again a practically perfect cloaking performance is demonstrated. The minor amplitude variations of E_z in the 'shadow-region' of Figure 5.23(d) are due to the underlying GO approximation employed in the proposed solution. Such an approximation places limitations on how fast the phase of a wave can change relative to the material parameters of the media in which the wave is propagating. The operating frequency is held constant through both of the aforementioned simulations, but the path at which the wave traverses now changes depending on the angle of incidence of the surface wave (owing to the rotationally asymmetric nature of the surface). Keeping this in mind, the minor shadowing displayed in Figure 5.23(d) can be accounted for by the rate of change of the material parameters on the cloak exceeding the allowable limit set by GO. To quantify the performance of the proposed cloak, the method used to validate the illusion device is adapted (see Figure 5.16(b)). Here two probe lines, each $10\lambda_0$ in length, whose centers are $15\lambda_0$ away from the origin of the deformation, are oriented as shown in Figure 5.16(b). In the first instance, $\theta_i = 0$, and the amplitude of E_z along the red probe line is recorded

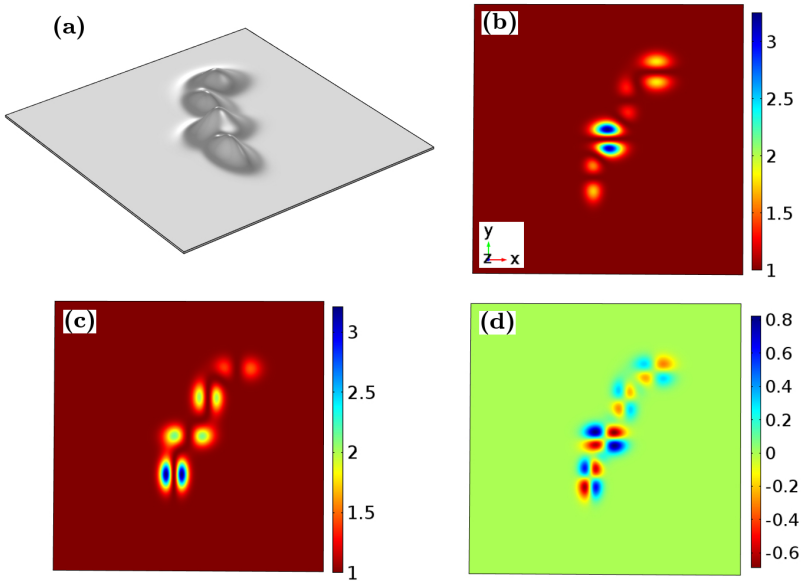

Figure 5.19: (a) Isometric view of CAD surface (b) $\varepsilon_{r,xx}, \mu_{r,xx}$. (c) $\varepsilon_{r,yy}, \mu_{r,yy}$. (d) $\varepsilon_{r,xy}, \mu_{r,xy}$.

(see Figure 5.24). Here, due to the interference pattern created in the wake of the uncloaked surface deformation, the amplitude of E_z varies as it travels down the probe-line (black curve in Figure 5.24). The cloaked surface deformation, however, perfectly reproduces the characteristics of a plane wave (red curve in Figure 5.24), as is required for the cloak to function properly. Next, $\theta_i = \frac{\pi}{4}$ and the amplitude of E_z along the blue probe line (see Figure 5.16(b)) is plotted. Once again, an interference pattern created in the wake of the uncloaked deformation (black curve in Figure 5.25) is displayed, while the cloaked deformation perfectly recreates the behavior of a plane wave (red curve in Figure 5.25). This behavior is exhibited for all angles of incidence, which means that this cloaking device is omnidirectional. Taking the sample line results and those in Figure 5.23 into account, it can be concluded that the proposed cloaking device faithfully cloaks a rotationally asymmetric surface deformation from bounded plane waves for multiple angles of incidence to an exceptionally high degree.

5.4.3 Potential device realization schemes

As was first stated in the beginning of this section, these devices (both the cloak and illusion) are modeled in a PEC-material-PEC waveguide form, which means they do not directly represent the behavior of a true surface wave. In order to do so, the top PEC layer needs to be removed, as was done in Chapter 3 and Chapter 4, and material with prescribed refractive index (most likely in the form of a metasurface) applied to

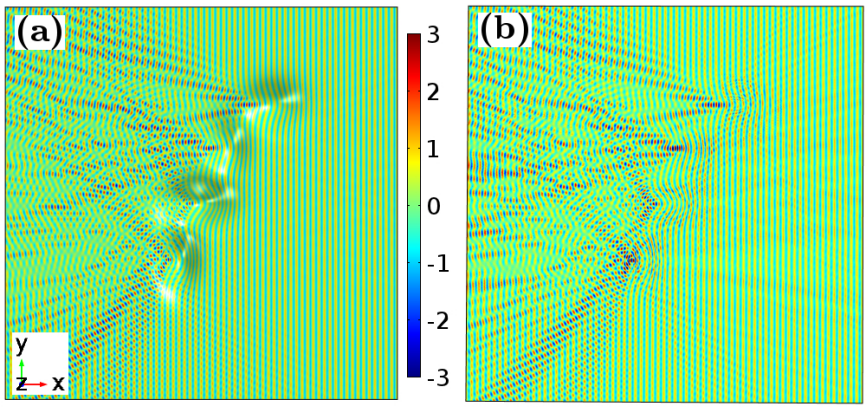

Figure 5.20: Plane wave propagating from right to left ($\theta_i = 0$), for curved isotropic medium (a) and flat anisotropic medium (b). Both results are for E_z.

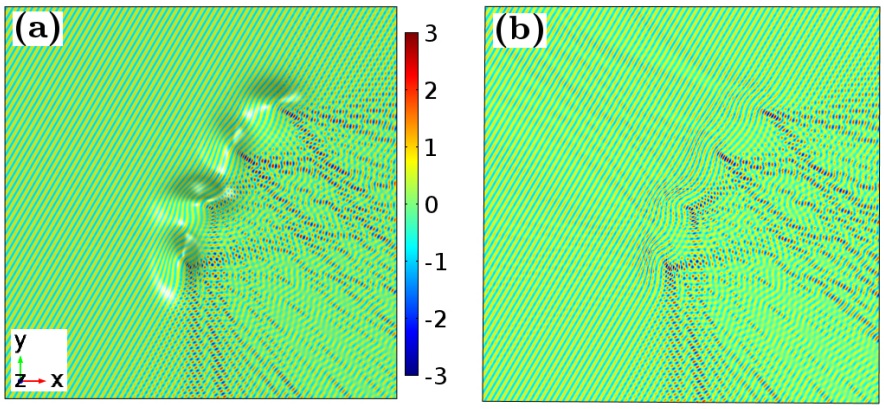

Figure 5.21: Plane wave propagating at $\theta_i = \frac{5\pi}{6}$ for a curved isotropic medium (a) and a flat anisotropic medium (b). Both results are for E_z.

the bottom PEC surface. Such a design process falls outside of the domain of this thesis which is focused on the derivation and validation of new TO design recipes as they relate to surface waves. However, a number of recent research efforts focusing on metasurfaces as reviewed by Maci *et al.* [113] and Yu *et al.* [114] could serve as a guide for how to realize a cloak or illusion device borne out of the technique derived in this chapters. Other works that focus on ways to realize material anisotropy for surfaces include, but are not limited to, Patel *et al.* [115], Martini *et al.* [116], Zedler *et al.* [117], Quarfoth *et al.* [118], Kwon *et al.* [57] and Gok *et al.* [119, 120]. That being said, there are two possible applications of the technique developed in this chapter. First, with respect to the illusion device, it can be used to recreate surface wave patterns of otherwise large curved surfaces in a small, compact form (i.e. in a flat plane). Second, the cloaking device can be used to counter the negative effects of surface curvature encountered in surface wave antenna [92] applications where the surface deformation is

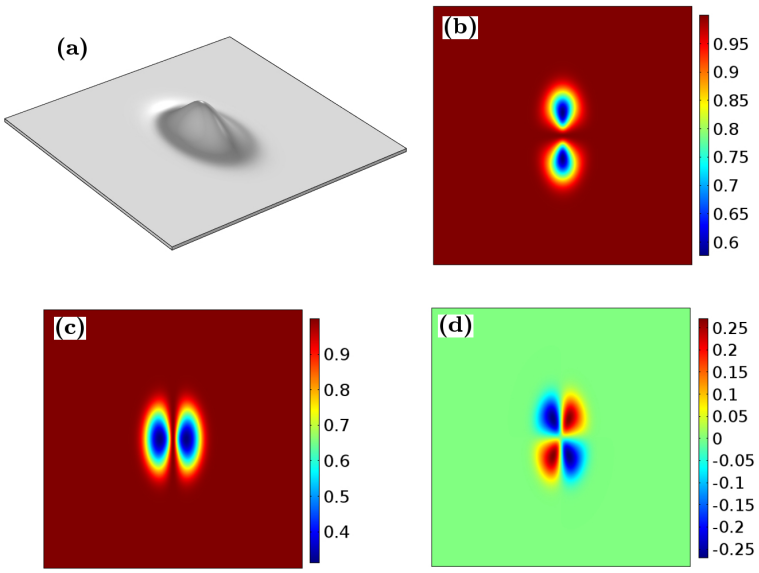

Figure 5.22: Isometric view of $z_1 = \sigma_1(x, y) = e^{-\left(3x^2+y^2\right)}$. (b) $\varepsilon_{r,xx}, \mu_{r,xx}$. (c) $\varepsilon_{r,yy}, \mu_{r,yy}$. (d) $\varepsilon_{r,xy}, \mu_{r,xy}$.

inherently asymmetric which would often occur in aerodynamic systems.

5.5 Conclusions

In this chapter the structural limitations found in Chapter 3 and Chapter 4, namely the required rotational symmetry of the surface deformation, were addressed. In order to do so, a fundamentally different approach needed to be considered that could deal with rotationally asymmetric surfaces (RASs) . First, in the case of the illusion device (a flat materially inhomogeneous device that emulates the scattering characteristics of a curved homogeneous device), a ground-up derivation was developed and the prescribed material properties for a sample surface (an asymmetric Gaussian deformation) were discussed. Then, moving onto the cloaking of a RAS, where to start a rotated plane was considered, another ground-up derivation was provided to cloak smooth surface deformations. Afterwards, a numerical solution is put forward to handle computer-aided design (CAD) surfaces, and the validity of the proposed technique is tested in both one and two dimensions.

In order to validate that the prescribed material loadings borne out of the proposed techniques do in fact create the desired devices, the parallel plate waveguide simulation technique used in Chapter 3 was implemented in a full-wave electromagnetic solver (COMSOL 5.0). Here it was demonstrated that the scattering characteristics of the RAS could be faithfully recreated by an illusion device. To quantify just how well the

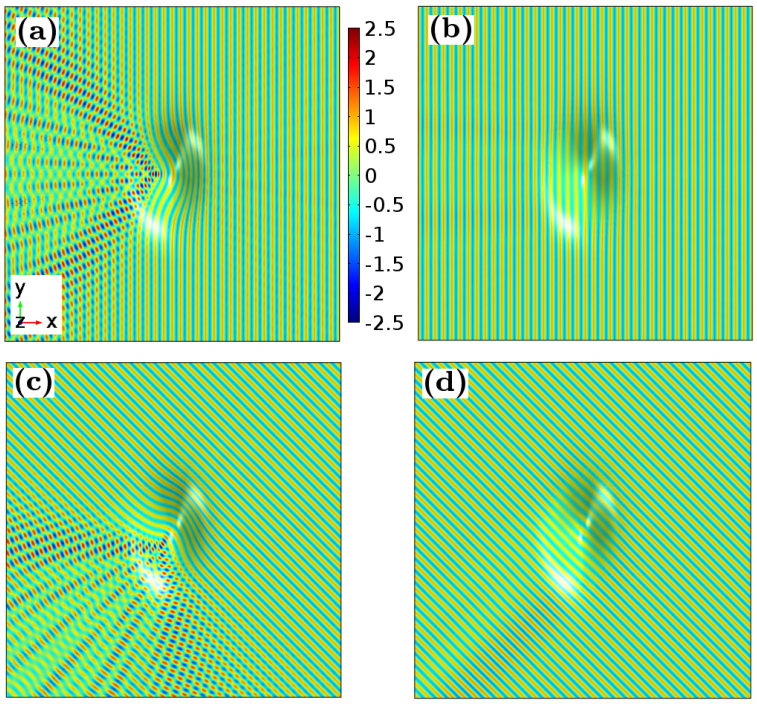

Figure 5.23: Plane wave propagating from right to left ($\theta_i = 0$), through a curved isotropic medium (a) and a curved, loaded, anisotropic medium (b). Plane wave propagating at $\theta_i = \frac{\pi}{4}$ through a curved isotropic medium (c) and a curved, loaded, anisotropic medium (d). All results are for E_z.

illusion device was functioning a sample line study was conducted and it was found that an excellent level of agreement existed between the curved RAS and the flat illusion device. Next, the numerical technique developed within this chapter was used to calculate the required material properties to create an illusion device for a CAD surface, and it was demonstrated that it successfully recreated the scattering characteristics of its curved analogue for two different angles of incidence. Lastly, the same RAS used in the analytically defined illusion device case study was shown to be completely cloaked for two different angles of incidence and the efficacy of cloak itself was quantified by analyzing the field distribution along two different sample lines (one for each angle of incidence). Owing to the material complexity of the proposed devices in this chapter, it is noted that obtaining a true surface wave device, though outside the domain of this thesis, may be possible using a variety of different techniques that are currently proposed within the metasurface community. The surface wave illusion and cloaking design recipe described in this chapter is novel because it can be directly applied to nearly any smooth surface (whether its form is known analytically or in the form of a CAD file, hence the term 'general'), as well as the fact that all the devices borne out of it are omnidirectional.

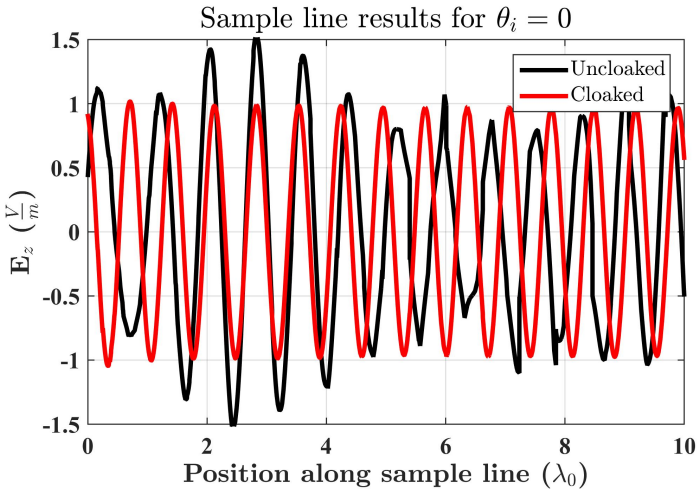

Figure 5.24: Quantitative validation of proposed cloaking device for $\theta_i = 0$.

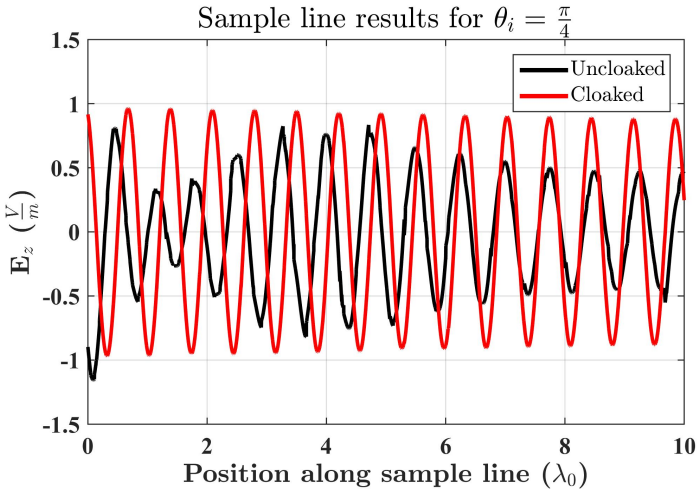

Figure 5.25: Quantitative validation of proposed cloaking device for $\theta_i = \frac{\pi}{4}$.

Chapter 6

Quantitative study of proposed cloaking techniques

6.1 Introduction

In this chapter a direct, comparative study between the surface wave cloaking techniques introduced in Chapter 3 and Chapter 5 is conducted. This chapter fits into the larger transformation optics (TO) community in two ways. First, as it deals with TO as it relates to surface waves, it builds upon other fundamental works that were alluded to in Chapters 3, 4 and 5, namely that of Huidobro *et al.* [43, 81], Liu *et al.* [80], Kadic *et al.* [44, 82] and Zhu *et al.* [60]. Secondly, it adds to a number of other studies within TO that compare different design methodologies (e.g. quasi-conformal mappings and linear geometrical transformations) such as those by Junqueira *et al.* [74], Wu *et al.* [64] and Huidobro *et al.* [81]. Worth noting also, is a quantitative study by Bao *et al.* [121] which used a correlation coefficient to quantitatively analyze the performance of two experimental demonstrations of a carpet cloak. Of these, the closest to the work found in this chapter is that of Huidobro *et al.* [81] where a one-to-one comparison in terms of transmittance (which they define as the ratio of incident power flow to transmitted power flow) of different mapping techniques (i.e. conformal and quasi-conformal) is studied. However, all of the surfaces of interest in the comparative study conducted in [81] where Euclidean (flat) and the ones that are of interest in this chapter are non-Euclidean (curved).

In this chapter the cloak from Chapter 3 is refereed to as an isotropic surface wave cloak (ISC) and the cloak from Chapter 5 is referred to as an anisotropic surface wave cloak (ASC), due to the material properties called for in the two techniques. Owing to the limiting factor of rotational symmetry inherent to the ISC approach, a surface deformation that can be handled by both techniques is studied. The simulation

method used in Chapter 3 and Chapter 5 is then implemented and the performance of both of the cloaks for multiple angles of incidence is analyzed. As the two cloaks behave virtually identically when inspecting the amplitude of their scattered E-field, focus is instead put on the performance of their scattered magnitude and phase. In doing so, clear distinctions can be made between the design methods. To aid in the quantification of the surface wave cloaks performance, the idea of a 'bounding ring' is introduced which is designed to capture the omnidirectional scattering of the surface deformations. Lastly, in an attempt to quantify the performance of a surface wave cloak with a single value, a mean absolute error calculation is performed and the results for the different cloaking techniques are analyzed.

In Chapters 3 and 5, two different approaches to cloaking a surface deformation (SD) were presented. In Chapter 3 it was shown that as long as the SD was rotationally symmetric, and differentiable everywhere (smooth), a unique generalization of Fermat's principle could be applied to solve for the correct material loading, $n_c(\theta)$, as it appears in

$$\int_0^{\frac{\pi}{2}} n_c(\theta)\sqrt{(R(\theta))^2+(R'(\theta))^2}\,\mathrm{d}\theta = n\int_0^R \mathrm{d}r \tag{6.1a}$$

$$2\pi R(\theta)\sin(\theta)n_c(\theta) = 2\pi r n, \tag{6.1b}$$

To solve for SDs were $R(\theta)$ could not be analytically determined, a numerical approximation to determine $n_c(\theta)$ as it appears in (6.1), was derived were it was found that

$$n_{c,i+1} = n_{c,i} - \Delta\theta\Big[\csc(\theta_i) - \frac{R'(\theta_i)}{R(\theta_i)} + \cot(\theta_i)\Big]. \tag{6.2}$$

For clarity, the material solutions borne out of (6.1) and (6.2) are hereon forward referred to as isotropic surface wave cloaks (ISC). Moving on, as was also pointed out in Chapter 3, if the SD is rotationally asymmetric about its origin, it is not possible to use (6.1) to solve for $n_c(\theta)$ and because of this, it was necessary to derive a new cloaking method as was done in Chapter 5. In order to implement the proposed solution, it was shown that the SD must be representable in the Monge form ($z=\sigma(x,y)$), and be differentiable everywhere (smooth). Having satisfied these conditions it is then possible to directly solve for the sought after material properties via

$$\begin{pmatrix}\mu_{xx} & \mu_{xy} & \mu_{xz}\\ \mu_{xy} & \mu_{yy} & \mu_{yz}\\ \mu_{xz} & \mu_{yz} & \mu_{zz}\end{pmatrix} = \frac{1}{1+(\nabla\sigma)^2}\begin{pmatrix}1+\left(\frac{\partial\sigma}{\partial x}\right)^2 & \frac{\partial\sigma}{\partial x}\frac{\partial\sigma}{\partial y} & 0\\ \frac{\partial\sigma}{\partial x}\frac{\partial\sigma}{\partial y} & 1+\left(\frac{\partial\sigma}{\partial y}\right)^2 & 0\\ 0 & 0 & 1+(\nabla\sigma)^2\end{pmatrix}, \tag{6.3}$$

where $\boldsymbol{\mu}=\boldsymbol{\varepsilon}$. Cloaks borne out of this technique, are hereon forward refereed to as

anisotropic surface wave cloaks (ASC). Having developed two distinct methods to cloak SDs it is natural to try and determine which one is effectivly 'better at cloaking.' The question of gauging a surface wave cloaks performance was attempted in Chapter 3, and then again in Chapter 5, where a probe line was placed in the 'shadow region' of the cloak and the resulting amplitude of the total field (sum of the incident and scattered fields), of E_z was measured. If the field was in agreement (in terms of amplitude and frequency) with an unperturbed plane-wave traveling in the same direction, it was concluded that that cloak was behaving as expected. This was an improvement over simply inspecting a contour plot of total E_z along the surface and ensuring that the phase fronts were behaving as required, but it does not completely quantify a cloaks performance, which is ultimately the first step in answering the question of, 'which one is better at cloaking.' Therefore, a more encompassing and thorough performance metric needs to be put forward, such as the one proposed in this chapter.

6.2 Isotropic vs. anisotropic cloaks

In order to attempt a direct one-to-one comparison between the ISC and ASC techniques, a SD that can be acted upon by both methods needs to be selected. As alluded to earlier this means that the SD must be rotationally symmetric and smooth (as was determined in Chapter 3), which makes the now familiar Gaussian deformation, $\sigma(x, y) = e^{-(\alpha x^2+\beta y^2)}$ an ideal candidate. In order to ensure rotational symmetry, one simply sets $\alpha = \beta$ as is done in Figure 6.1. To validate that the ISC technique, namely

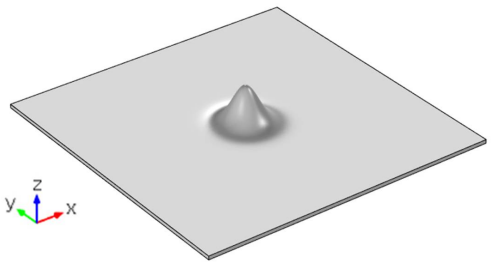

Figure 6.1: Surface deformation, $z = \sigma(x, y) = e^{-5(x^2+y^2)}$, used to compare the ISC and ASC techniques.

(6.2), is being properly implemented its output is compared with known analytical solutions for both hemispheric (with a radius of unity) and conic (also with a radius of unity) surface deformations (see Figure 6.2). Here the obtained $\varepsilon_r(r)$ is expressed as a function of radial length, and not θ, as this is the format in which the material parameters are imported into the full-wave electromagnetic solver (COMSOL 5.0). The curves in Figure 6.2, demonstrate that there is an exceptional level of agreement between the

numerical and analytical solutions for both of the surface deformations, which means it is safe to assume that (6.2) is being correctly implemented. A top-down view of

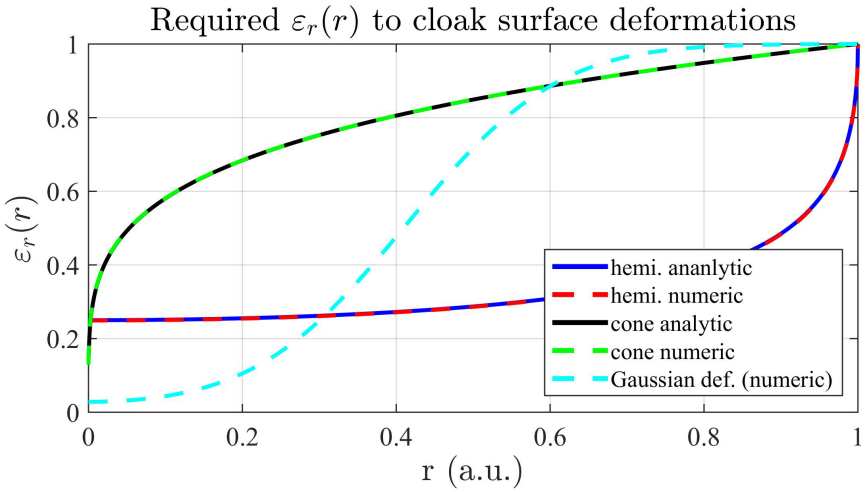

Figure 6.2: ε_r used by an ISC as determined by (6.2).

the required material properties as determined by (6.2) for the ISC are displayed in Figure 6.3. In order to determine the required material properties for the ASC tech-

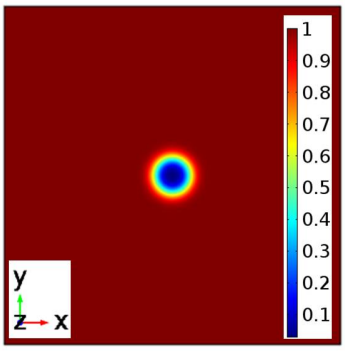

Figure 6.3: Obtained ε_r using the ISC technique. $\mu_r = 1$ for this method.

nique, $\sigma(x, y) = e^{-5\left(x^2+y^2\right)}$ is substituted into (6.3) and the necessary calculations are performed (see Figure 6.4).

6.3 Simulations

6.3.1 Simulation setup

The simulation setup for the comparative study is identical to the one used in Chapter 3 and Chapter 5. Just as before, the surface wave behavior is modeled using a parallel plate waveguide method, where the material is effectively sandwiched between

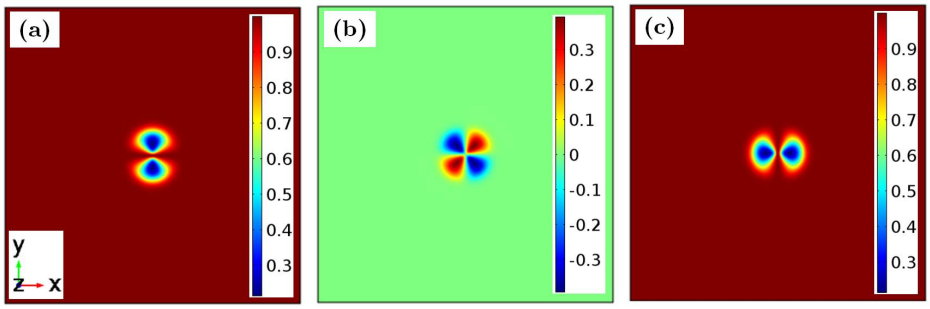

Figure 6.4: Obtained $\boldsymbol{\varepsilon_r}$ and $\boldsymbol{\mu_r}$ using the ASC technique with (a) $\varepsilon_{r,xx} = \mu_{r,xx}$, (b) $\varepsilon_{r,xy} = \mu_{r,xy}$ and (c) $\varepsilon_{r,yy} = \mu_{r,yy}$. Note that $\varepsilon_{r,zz} = \mu_{r,zz} = 1$.

two perfect electric conductor (PEC) sheets (normal to the Z-axis) that are separated by a distance of $\lambda_0/10$. This electrically small separation between the two PEC sheets ensures that $\underline{E}$ always remains normal to surface deformation. Next, the remaining edges of the surface are bounded by a λ_0 thick perfectly matched layer (PML), and the method of excitation is a bounded space wave with $\underline{E}$ (with an amplitude of 1 V/m) oriented along the Z-direction, and $\underline{k}$ oriented in the XY-plane. The mesh configuration used in these simulations is the same as those used in Chapter 3 and Chapter 5, namely no tetrahedral edge length is greater than $\lambda_0/15$ to increase the likelihood of a reaching a convergent solution. Also, due to the inherent requirements of geometrical optics (GO), the SD must be electrically large. Put another way, the phase of the impinging wave front must vary more rapidly (in the direction of $\underline{k}$) than n_c (also in the direction of $\underline{k}$). This is an important feature to keep in mind when analyzing the following results because unlike in the previous chapters, there are two different material gradients (one for the ISC and the other for the ASC), in any given direction of $\underline{k}$.

6.3.2 Simulation results

Though the simulation setup may be identical to the one employed in previous chapters, the measurements of interest pertaining to E_z are different. Earlier, the focus was on inspecting the amplitude of E_z as this was the most immediate way of determining whether or not a proposed surface wave device was functioning properly (via inspection of phase fronts). This value however, encapsulates two quantities that when separated, allow for a deeper understanding of a surface wave device's behavior: $|\mathrm{E}_z|$ and $\phi(\mathrm{E}_z)$, which are the magnitude and phase of E_z, respectively. By inspecting these two values, one sets out to observe and quantify previously unknown surface wave cloaking characteristics of the ISC and ASC techniques. To start, $|\mathrm{E}_z|$ is calculated for two different angles of incidence ($\theta_i = 0, \frac{\pi}{4}$). In terms of the uncloaked SD's scattering characteristics, Figure 6.5(a,d) reveals pronounced destructive and constructive inter-

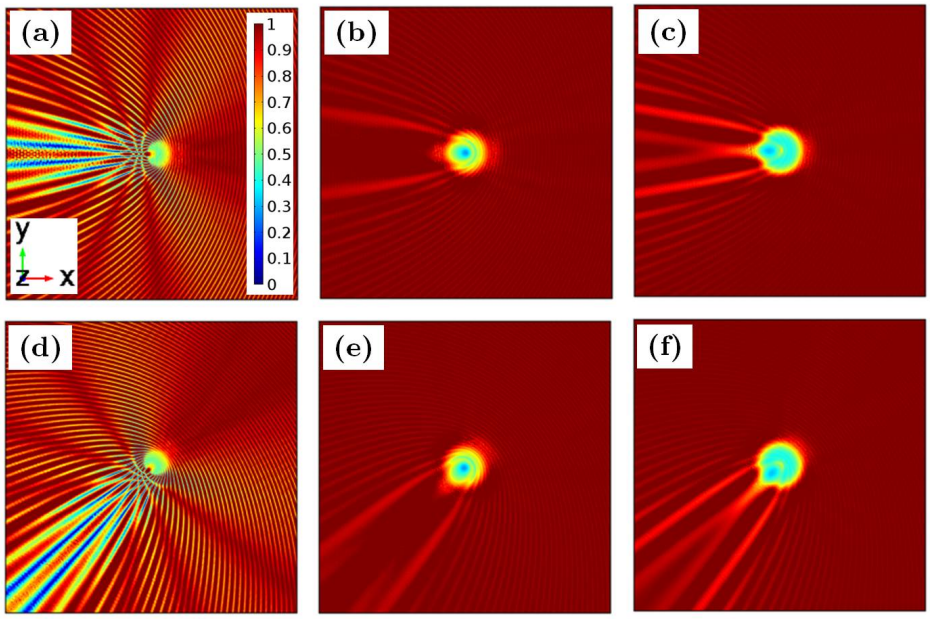

Figure 6.5: $|E_z|$ of (a) uncloaked, (b) ISC and (c) ASC for $\theta_i = 0$ and $|E_z|$ of (d) uncloaked, (e) ISC and (f) ASC for $\theta_i = \frac{\pi}{4}$.

ference patterns in both the forward surface wave scattering (FSWS) and backward surface wave scattering (BSWS) directions. Here, as in Chapters 3 and 5, the term surface wave scattering is effectively commenting on the behavior of the bounded plane wave inside the loaded waveguide structures that are designed to emulate the behavior of a surface wave. That said, this should come as no surprise, considering the 'smooth' curvature of the SD, which provides a continuous transition from the flat approach plane to the SD itself. With regards to the cloaks behavior, Figure 6.5(b,c,e,f) reveals that both cloaks offer a substantial amount of cloaking in all directions, but with a significant improvement in the forward direction. At this point, it is important to remember that both of these techniques rely on GO which means that they are inherently unable to account for phenomena such as smooth body diffraction, which is predominately the cause for the wave fronts witnessed in Figure 6.5 (b,c,e,f). Focusing solely on how the ISC and ASC relate to one another in the FSWS-direction, the ISC appears to be functioning slightly better in that it does not possess the 'forking-beam' that appears in the shadow region of the ASC (see Figure 6.5(c,f)). Ultimately this difference may be a consequence of incident plane wave not having a high enough frequency to ensure that the GO limit is met for the ASC. The main reason for thinking this is because, as is displayed in Figure 6.3 and Figure 6.4, the material properties of the ASC vary more rapidly (along the same paths) than their counterparts in the ISC. Further quantification of how detrimental this forking beam actually is to the cloaks overall

performance is quantified later on in this chapter. Continuing on, $|E_z|$ is calculated for $\theta_i = \frac{\pi}{2}$. In Figure 6.6 the same disparity between the ISC and ASC as seen in Figure

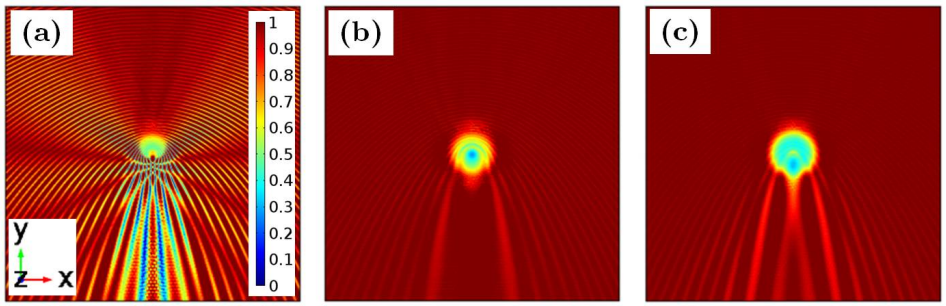

Figure 6.6: $|E_z|$ of (a) uncloaked, (b) ISC and (c) ASC for $\theta_i = \frac{\pi}{2}$.

6.5 is witnessed, as is expected considering that the surface deformation under study is rotationally symmetric. Worth noting, however, is that though the ISC is rotationally symmetric in terms of material loading the ASC cloak is not, and that is why it is essential to test both devices for multiple angles of incidence. In conclusion, from Figure 6.5 and Figure 6.6 it is apparent that both the ISC and ASC offer noticeable improvements with regards to minimizing the omnidirectional scattering of $|E_z|$, but the ISC appears to functioning slightly better, owing to the detrimental interference pattern ('forking-beam') setup in the shadow region of the ASC.

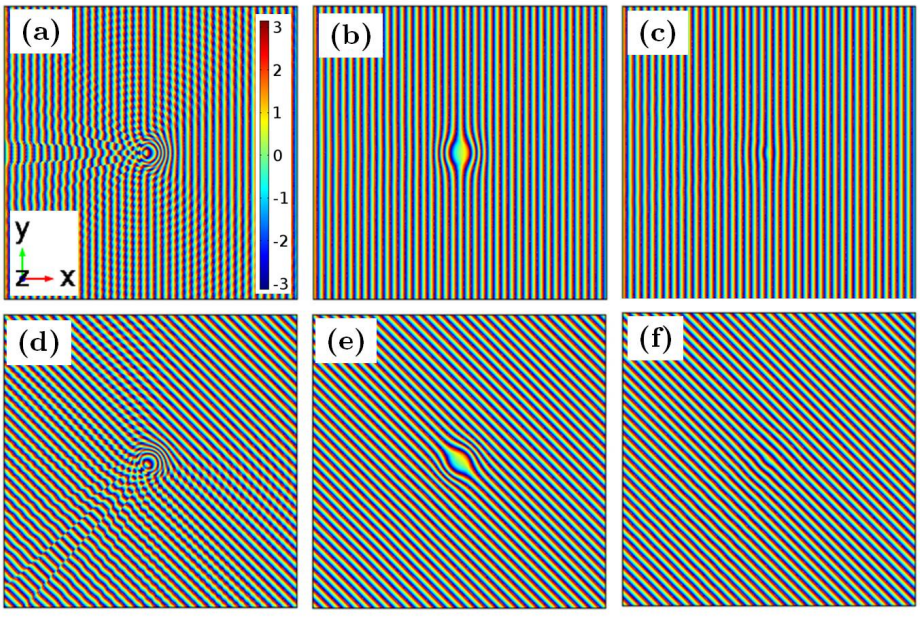

Figure 6.7: $\phi(E_z)$ of (a) uncloaked, (b) ISC and (c) ASC for $\theta_i = 0$ and $\phi(E_z)$ of (d) uncloaked, (e) ISC and (f) ASC for $\theta_i = \frac{\pi}{4}$.

The second quantity of interest in this study is the phase of E_z (denoted herein as $\phi(E_z)$) which is calculated for in Figure 6.7 for two different angles of incidence. Just as was the case for $|E_z|$, $\phi(E_z)$ is highly disrupted for the uncloaked SD case (Figure 6.7(a,d)), but with minimal interference in the BSWS-direction. In terms of the cloaks behaviors, both the ISC and ASC offer an excellent level of performance in terms of reproducing the scattering characteristics of a surface wave traveling along a flat surface (see Figure 6.7(b,c,e,f)). Next, $\phi(E_z)$ is calculated for when $\theta_i = \frac{\pi}{2}$ (Figure 6.8), and once again both cloaks perform exceptionally well. Based on the results shown in Figure 6.7 and Figure 6.8, both cloaks, with respect to $\phi(E_z)$, offer a vast improvement in all scattering directions and angles of incidence, when compared to their uncloaked SD counterpart. However, just as was the case for $|E_z|$, in order to truly quantify the

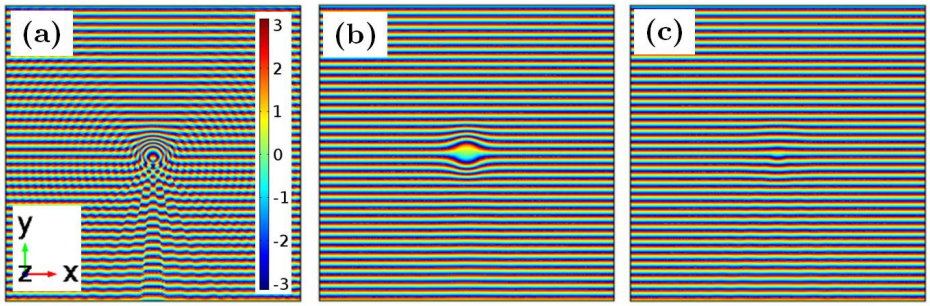

Figure 6.8: $\phi(E_z)$ of (a) uncloaked, (b) ISC and (c) ASC for $\theta_i = \frac{\pi}{2}$.

ISC and ASC scattering behavior with respect to $\phi(E_z)$, another method needs to be employed as is described in the next section.

6.4 Proposed performance metrics

In an attempt to quantify the performance of the two cloaks a unique sampling line, in the shape of an ring, is placed around the surface deformation (see Figure 6.9). In doing so, the omnidirectional surface wave scattering (OSWS) characteristics of the cloaks can be analyzed. As the name implies, the purpose of this sampling line is to capture the scattering of an incident surface wave in all directions. The radius of the sampling ring is determined by taking two features into consideration. First, the ring should be on a flat (Gaussian curvature, $K = 0$) part of the surface (not on the bump itself) as this is the region of interest in this study. Second, the ring should not have a radius that is too far from the scatterer so as to unnecessarily increase the size, and in turn complexity, of the model itself. For this particular study, the nominal radius of the ring is $r_a = 15\lambda_0$ and is displayed with the SD in Figure 6.9.

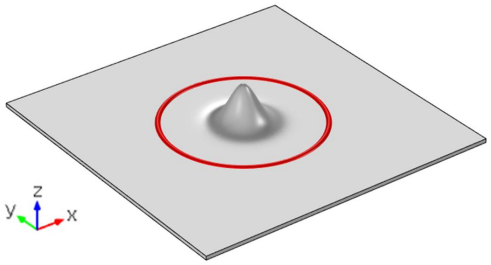

Figure 6.9: Bounding ring surrounding $\sigma(x, y) = e^{-5\left(x^2+y^2\right)}$.

Just as was done previously, the first quantity of interest is $|\mathrm{E}_z|$ for various scatterer configurations(i.e. an isotropic cloak, an anisotropic cloak, no cloak and the ideal flat surface). Figure 6.10 displays the results of a wave (with unity amplitude) impinging on the SDs at $\theta_i = 0$. Now it is possible to fully appreciate how well the ISC and ASC techniques cloak the surface deformation, a feature that was hinted at in Figure 6.5(b,c). Starting with the most prominent feature of Figure 6.10, the scattering behavior of the uncloaked deformation (black curve), it is noted how varied $|\mathrm{E}_z|$ is along the bounding ring, ranging from approximately 1.6 V/m at $\theta_a = \frac{\pi}{3}$ to approximately 0.1 V/m at θ_a close to π. On the whole, the black curve helps quantify the interference pattern seen in Figure 6.5(a). Moving on to the flat surface (red curve in Figure 6.10) it should be pointed out that, as the name implies, this surface is void of any scatterer (SD) and in turn its total field is simply the incident field. Lastly, the substantial improvement with regards to emulating the surface wave behavior provided by the ISC (green curve) and ASC (blue curve) in Figure 6.10 is observed. In terms of the superior performer in this instance, it can be seen in Figure 6.10 that the ISC (green curve) deviates less from the flat surface (red curve), than the ASC (blue curve), especially in the FSWS region (when $\theta_a \approx \pi$), but to what extent it deviates is analyzed later on. As a side note, it is important to keep in mind that θ_a represents a points location on the bounding ring whereas θ_i represents the angle of incidence of an incoming plane wave. Both conventions, however, define θ as the angle formed relative to the X-axis as it is swept into the Y-axis as seen in Figure 6.9.

To focus on the scattering characteristics of the ISC and ASC, the results for the uncloaked SD are removed (see Figure 6.11). Here it is quite clear that the ISC performs better (in terms of emulating the behavior of a flat surface) than the ASC for all points along the bounding ring, except at $\theta_a = 0, 2\pi$, implying that the ASC may be better at scattering in the BSWS-direction. Another apparent feature of Figure 6.11 is that the two cloaking techniques appear to have the same spatial frequency along the sampling ring, something that is not too surprising considering Figure 6.5(a,b). Lastly regarding the scattering characteristics of the flat surface (red curve), one expects this value to be

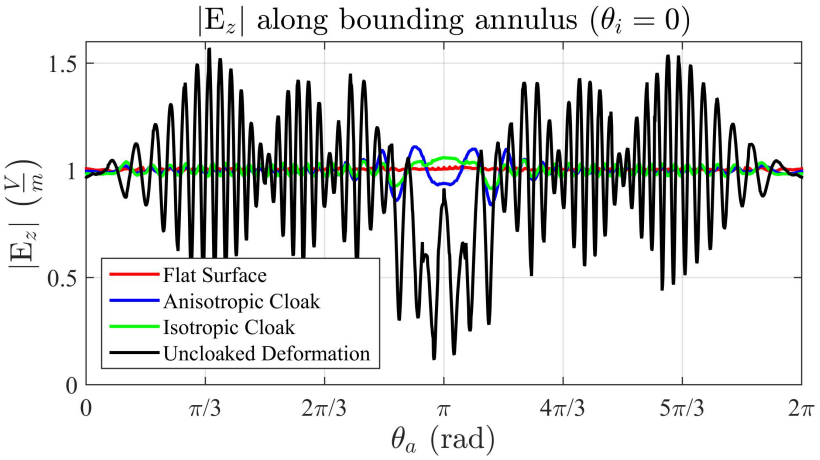

Figure 6.10: $|E_z|$ along the bounding ring for different scatterer configurations with $\theta_i = 0$.

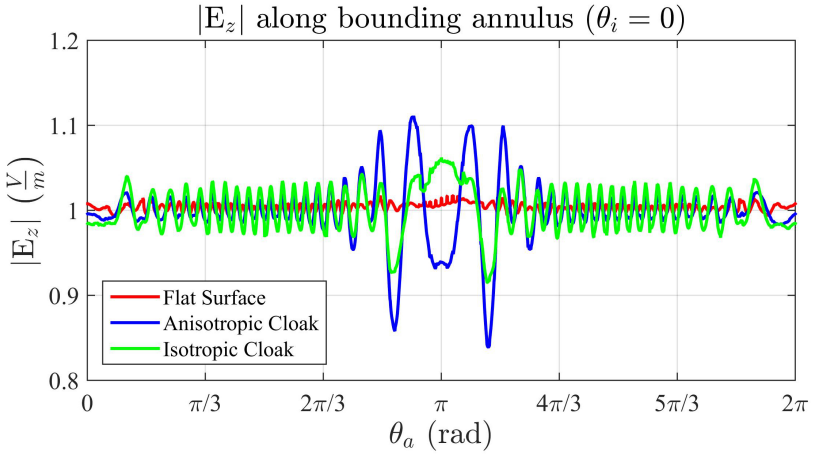

Figure 6.11: $|E_z|$ along the bounding ring for different scatterer configurations with $\theta_i = 0$ and uncloaked SD results removed.

$1\ V/m$ at all points along the bounding radius, but due to numerical artefacts (namely mesh quality and an imperfect implementation of a PML), and slight 'ripple' can be accounted for.

Continuing on, $|E_z|$ along the bounding ring is calculated for the three different surface configurations (Figure 6.12) when $\theta_i = \frac{\pi}{4}$. Here, just as the case when $\theta_i = 0$, the ISC cloaks the deformation better for all values of θ_a except for values of θ_a close to 0 and 2π and the overall scattering characteristics are effectively shifted $\frac{\pi}{4}$ to the right. Finally, the results are calculated for when a surface wave is incident upon the scatterer configurations at $\theta_i = \frac{\pi}{2}$, and the same trend as before is witnessed: all three scattering curves are shifted by $\frac{\pi}{4}$ to the right, and the ISC peforms better in the FSWS region and the ASC in the BSWS region (see Figure 6.13). Taking Figure 6.10–6.13 into

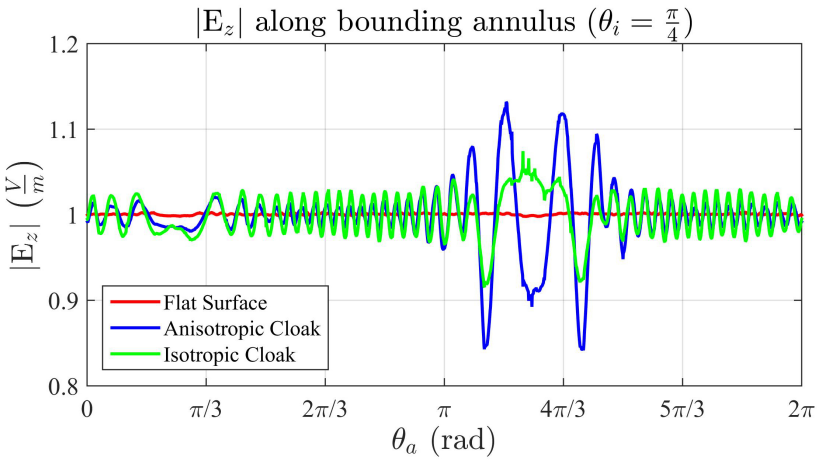

Figure 6.12: $|E_z|$ along the bounding ring for different scatterer configurations with $\theta_i = \frac{\pi}{4}$.

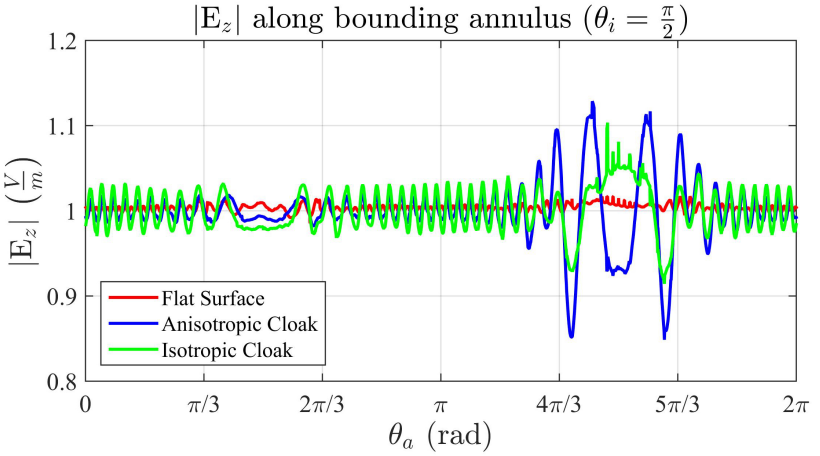

Figure 6.13: $|E_z|$ along the bounding ring for different scatterer configurations with $\theta_i = \frac{\pi}{2}$.

consideration it is clear that both cloaks offer a substantial improvement in reducing the overall scattering caused by the SD, but the ISC appears to do so better for the FSWS region and the ASC for the BSWS region. In order to obtain a better idea of 'how much better' another performance metric is proposed and utilized later on in this chapter.

Next the scattering characteristics of the SDs are investigated, but this time with respect to phase. Just as before, it is important to keep in mind that the total field (the sum of the incident and scattered fields) is investigated. The result of calculating $\phi(E_z)$ along the bounding ring for surface wave incident at $\theta_i = 0$ is displayed in Figure 6.14. Here there appears to be exceptional agreement for all scatterer configurations,

including the unloaked SD, at all points along the ring except for those near $\theta_a = \pi$ which corresponds to the FSWS region. A better plot (one excluding the results for the

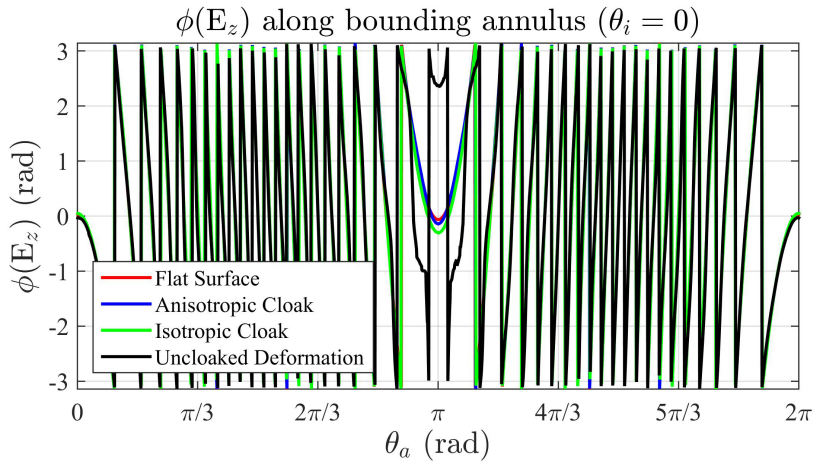

Figure 6.14: $\phi(E_z)$ along the bounding ring for different scatterer configurations with $\theta_i = 0$.

uncloaked SD) is displayed in Figure 6.15 where it is apparent that both the ISC and the ASC are performing exceptionally well, but with the ASC having a slight advantage in the FSWS-direction ($\theta_a = \pi$). Changing the angles of incidence to $\theta_i = \frac{\pi}{4}$ (Figure

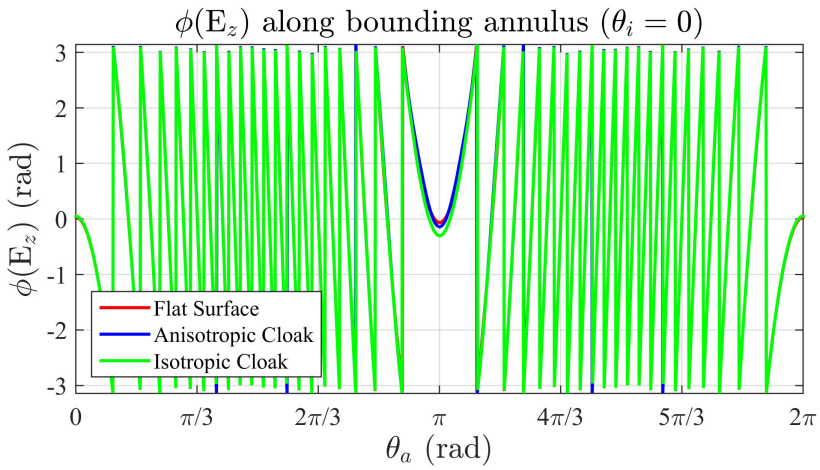

Figure 6.15: $\phi(E_z)$ along the bounding ring for different scatterer configurations with $\theta_i = 0$ with uncloaked SD results removed.

6.16) and $\theta_i = \frac{\pi}{2}$ (Figure 6.17) and performing the necessary calculations produces the same results, but with the expected curve shift to the right at $\frac{\pi}{4}$ increments. In summary, Figure 6.14 –6.17 reveal that both cloaking techniques offer an improvement with regards to emulating the phase behavior in the FSWS region of a flat surface. However, because the results overlap for nearly all θ_i and θ_a, it is not possible to

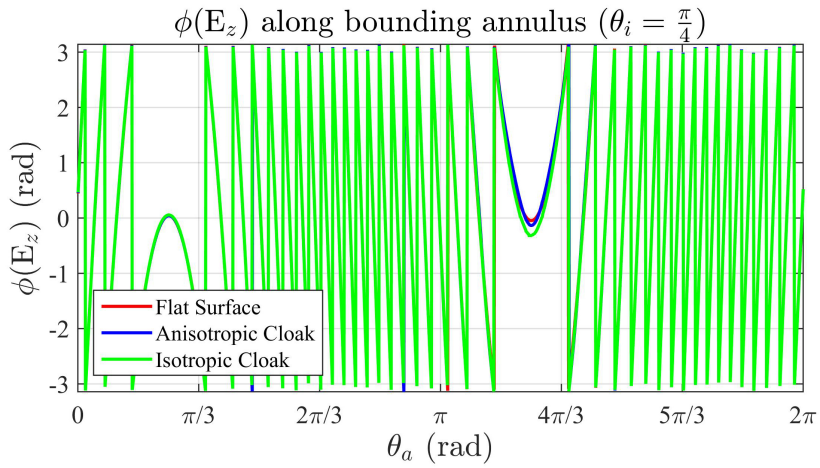

Figure 6.16: $\phi(\mathrm{E}_z)$ along the bounding ring for different scatterer configurations with $\theta_i = \frac{\pi}{4}$.

comment on which technique is superior other than that in the FSWS region, where the ASC appears to perform slightly better.

In Chapter 5 the mean absolute error (MAE) was introduced to gauge the level of agreement between partial derivatives calculated numerically and those calculated analytically. This technique allowed for a very easy and efficient method to compare two sets of data. More importantly, however, the MAE could handle data sets that contained the number 0 (as is the case for phase measurements), which would present problems for any error estimation technique, such as the classic percentage error, where there is a possibility of having 0 in the denominator of an equation (thereby leading to an undefined variable). Taking this into consideration, the MAE is an ideal method for determining the level of agreement (in terms of $|\mathrm{E}_z|$ and $\phi(\mathrm{E}_z)$) between the flat surface and proposed cloaks. The MAE is defined as

$$\mathrm{MAE} = \frac{1}{n_p} \sum_{i=1}^{n_p} |\alpha_{0,i} - \alpha_i| \,, \tag{6.4}$$

where n_p is the number of sampling points (namely the points that are on the bounding ring in Figure 6.9), α_0 is a value corresponding to the cloak (either ISC or ASC) and α is value a corresponding to the flat surface. Carrying out the necessary calculation for 13 different angles of incidence (θ_i) for both magnitude and phase agreement of E_z, produces the plots displayed in Figure 6.18 and Figure 6.19, respectively.

Before it is possible to draw any conclusions from Figure 6.18 one needs to know what the MAE values are for the uncloaked SD which turns out to be 0.2077 for nearly all θ_i. That being said, this means that on average both cloaking techniques offer

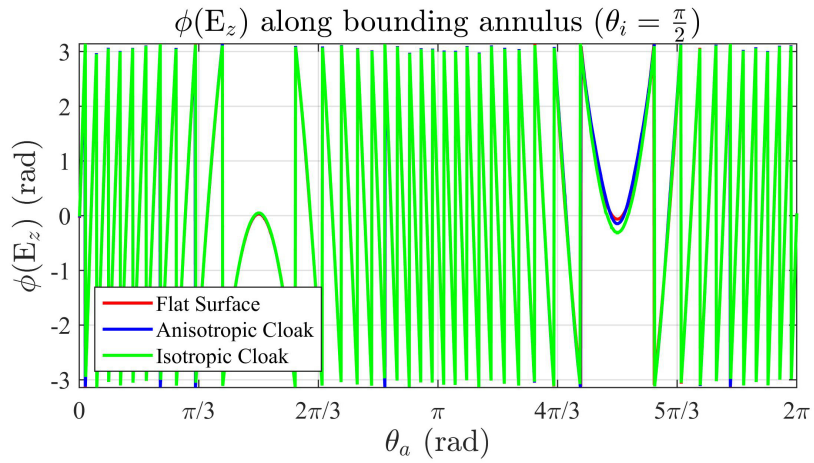

Figure 6.17: $\phi(E_z)$ along the bounding ring for different scatterer configurations with $\theta_i = \frac{\pi}{2}$.

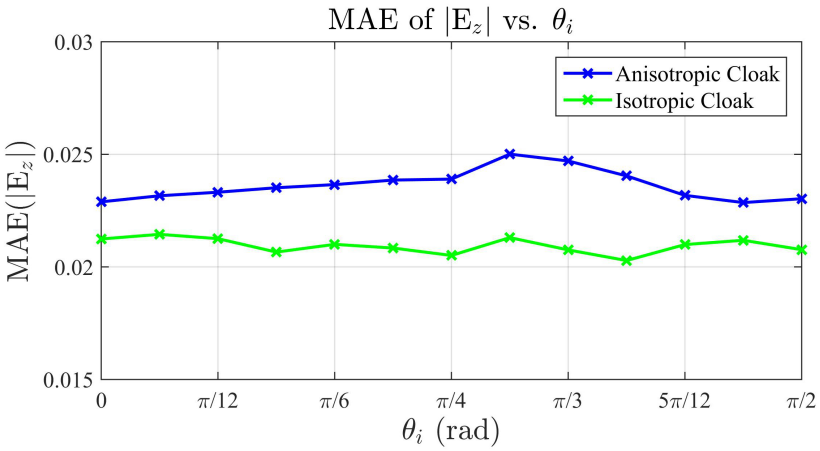

Figure 6.18: $|E_z|$ for various angles of incidence.

one order of magnitude improvement in performance (with respect to $|E_z|$ agreement). Also it is important to note that without exception, the ISC performs better than the ASC for all angles of incidence. This should be expected considering the previous figures describing $|E_z|$ scattering characteristics (Figure 6.10 – 6.13). However, the improvement that the ASC offered in the BSWS region (Figure 6.10 – 6.13) appears to have been nullified in this performance metric, a feature that will be addressed later in this section. Lastly, owing to the rotationally symmetric nature of the SD itself, the MAE($|E_z|$) for both cloaking techniques, is effectively a constant for all θ_i with only slight perturbations caused by the aforementioned numerical artefacts. Next, the level of phase agreement is investigated.

The same procedure as above is carried out, but this time with respect to $\phi(E_z)$ (see

Figure 6.19). In this instance, the average MAE value for the uncloaked deformation

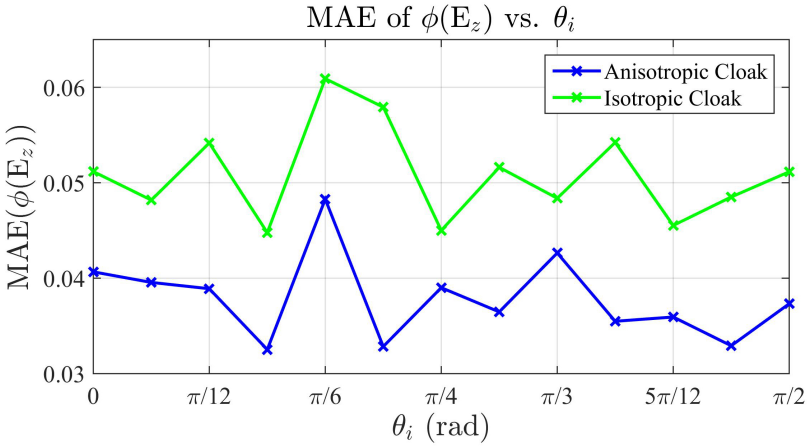

Figure 6.19: $\phi(E_z)$ for various angles of incidence.

is 0.5437 which means once again both cloaks offer an improvement of one order of magnitude. From Figure 6.19 it is apparent that the ASC is the superior of the two cloaks, for all θ_i, and also once again their is a near-constant value for both curves for all angles of incidence. Having conducted a MAE study for both the magnitude and phase of E_z it is concluded that the ISC is the superior candidate in terms of $|E_z|$ agreement and the ASC is the superior candidate in terms agreement with $\phi(E_z)$. This is assuming that all elements in the (6.4) are of equal weight, but as was hinted at earlier it may be advantageous to be able to manipulate (6.4) in such a way as to focus on particular scattering behaviors.

In Chapter 5 it was pointed out that depending on the application one may be interested in either the FSWS or BSWS and because of this a weighted MAE of sorts would be appropriate to gauge the performance of a cloak. One simple method to identify FSWS and BSWS in the context of this study is as follows. If a surface wave is incident upon the SD at, $\theta_i = 0$, then scattered waves that fall within $\frac{\pi}{2} \leq \theta_a \leq \frac{3\pi}{2}$ are classified FSWS, and the ones that fall within the remainder of the ring ($\frac{3\pi}{2} \leq \theta_i \leq \frac{\pi}{2}$) are classified as BSWS. In general if the wave is incident at θ_i, then FSWS are ones that exist at $\theta_i + \frac{\pi}{2} \leq \theta_a \leq \theta_i - \frac{\pi}{2}$, and BSWS fill the remainder of the ring. After decomposing the scattered surface waves into forward and backward scattering parts along the ring, one simply weights the absolute error elements as they appear in (6.5) appropriately which can be carried out programmaticaly by the use of a conditional statement. The weighted MAE equation is defined as

$$\text{MAE} = \frac{1}{n_p} \sum_{i=1}^{n_p} W(i) \left| \alpha_{0,i} - \alpha_i \right|, \tag{6.5}$$

where $W(i) = \frac{w_1(i)}{w_2(i)}$ is the weighting ratio that is a function of a points location along the bounding ring. In this scheme weights are assigned 'relative' to one another and w_1 and w_2 correspond to the BSWS and FSWS weights respectively.

For example, in Figure 6.20 $\frac{w_1}{w_2} = 3$, meaning the weighting factor assigned to absolute error values for BSWS components, as seen in (6.5), are three times greater than their FSWS components. The net effect of this is that any disparity that does arise between the flat surface and the cloak in the BSWS region are more pronounced than ones in the FSWS region. Figure 6.20 reveals that when it comes to omnidirectional

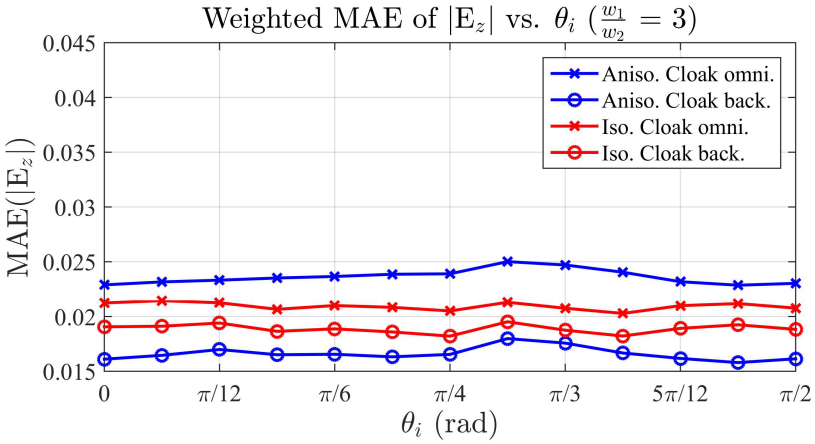

Figure 6.20: Weighted MAE of $|\mathrm{E}_z|$ with weight placed on the BSWS ($\frac{w_1}{w_2} = 3$).

weighting ($w_1 = w_2$) of $|\mathrm{E}_z|$, the ISC is superior across all angles of incidence (as was demonstrated in Figure 6.18) , but when the BSWS component is isolated and weighted, the ASC offers the better performance, also for all θ_i. More specifically, this calculation (blue curve with circular tick marks) accurately reflects the BSWS performance that was first commented on in Figure 6.11 – 6.13.

Next, the weighted MAE of $\phi(\mathrm{E}_z)$ is calculated (Figure 6.21) and it is revealed that the ASC offers superior scattering performance for all θ_i. In fact, Figure 6.21 reveals that even the omnidirectional weighting of the ASC (blue curve with cross ticks) performs better than the weighted ISC results (red curve with circular ticks). Taking Figure 6.20 and Figure 6.21 into consideration, it appears that the ASC offers superior performance with regards to emulating the magnitude and phase behavior of a flat surface in the BSWS region. One possible explanation for this is because in these particular simulations, the ISC is not impedance matched to the 'flat approach plane', where impedance for an isotropic medium is defined as

$$\eta = \sqrt{\frac{\mu}{\varepsilon}}. \tag{6.6}$$

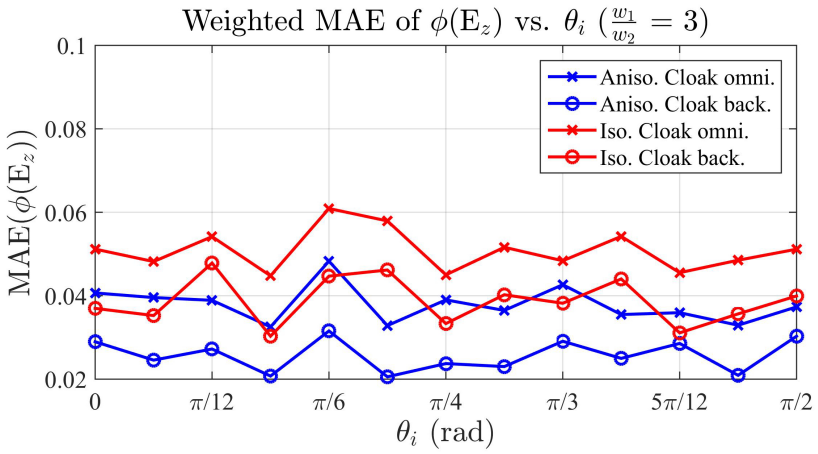

Figure 6.21: Weighted MAE of $\phi(\mathrm{E}_z)$ with weight placed on the BSWS ($\frac{w_1}{w_2} = 3$).

This is apparent when one realizes that in the case of the ISC, the flat approach plane has a material loading with $\eta = 1$ for all on-diagonals, because at all points along it $\mu_{i,j} = \varepsilon_{i,j}$, but when on the SD itself (where the cloak exists) $\mu_{i,j} \neq \varepsilon_{i,j}$, which leads to an impedance mismatch. In the case of the ASC, as stated in (6.3), $\boldsymbol{\mu} = \boldsymbol{\varepsilon}$ at all points along the surface, including the SD itself, which ensures an impedance match with the free-space approach plane which leads to little if any reflections.

Moving on, emphasis is now placed on the FSWS performance of the two cloaks and $\frac{w_1}{w_2} = \frac{1}{3}$. In Figure 6.23 it is demonstrated that the ISC performs better than the

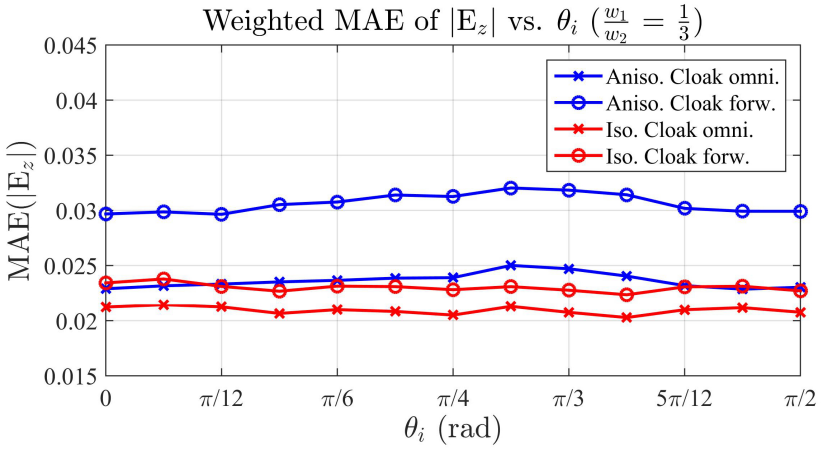

Figure 6.22: Weighted MAE of $|\mathrm{E}_z|$ with weight placed on the FSWS ($\frac{w_1}{w_2} = \frac{1}{3}$).

ASC for all θ_i, which is consistent with the results seen in Figure 6.11 – 6.13. Next, focusing on the phase agreement of the FSWS as is done in Figure 6.22, the ASC is the superior candidate for all θ_i which is to be expected considering findings in Figure 6.15 – 6.17. In conclusion, if a researcher is interested in a particular component of a

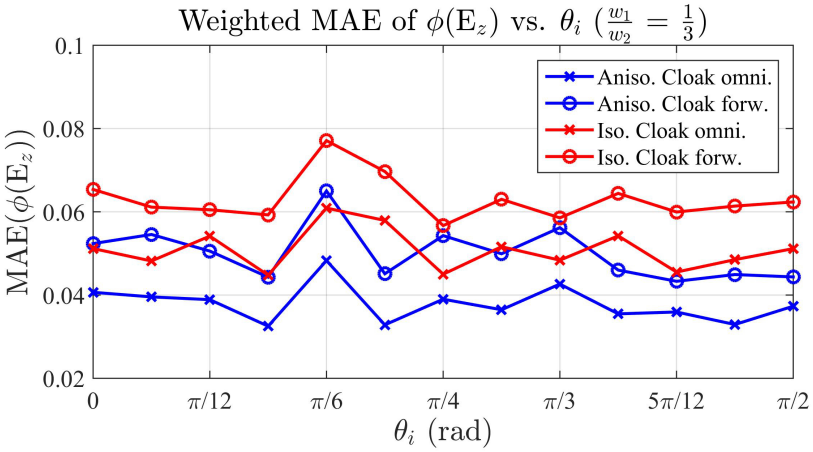

Figure 6.23: Weighted MAE of $\phi(E_z)$ with weight placed on the FSWS ($\frac{w_1}{w_2} = \frac{1}{3}$).

scattered surface wave and not the entire omnidirectional scattering, then the weighted MAE technique (6.5) may prove useful. Also worth mentioning, is that there is no numerical reason for why the FSWS and BSWS were focused on in this study other than that these tend to be the two scattering directions of most interest in the cloaking community. That said, one could easily manipulate (6.5) in such a way as to focus on particular 'lobes', as opposed to regions, of scattering by implementing a more complex 'classification algorithm' used on the points that constitute the bounding ring.

6.5 Conclusions

In this chapter a number of performance metrics were put forward to determine which of the derived cloaking techniques (ISC (6.1) and ASC (6.3)) were better at emulating the behavior of a surface wave traveling along a flat surface. This is an extension of not only the founding works of TO as it relates to surface waves [43, 44, 60, 80–82], but also works that compare different TO recipes [64, 74, 81]. The first step in this study was to find a surface deformation (SD) that was amenable to both cloaking techniques: a Gaussian deformation (Figure 6.1). To gain a deeper insight into the surface wave scattering (SWS) characteristics of the SD both the magnitude and the phase of E_z were inspected and analyzed which is an improvement over previous works regarding surface wave cloaks which normally would focus solely on the amplitude of E_z. Magnitude and phase plots of E_z along the entire surface were then inspected (Figure 6.5 – 6.8), and it was concluded that the ISC offered superior omnidirectional scattering performance with respect to $|E_z|$ for all θ_i. Also, the two cloaks performed equally well in terms of the minimizing the scattering of $\phi(E_z)$. Realizing that this was still not a truly quantitative one-to-one comparison between the scattering characteristics of the

two cloaks a unique sampling technique was implemented: the bounding ring (Figure 6.9). After doing so, it became apparent in Figure 6.10–6.13 that though the ISC was in better agreement with the flat surface for nearly all θ_i, it was not the case in the BSWS region, which was something that was not clear from Figure 6.5 and Figure 6.6. Thus, if one is primarily concerned with emulating the magnitude of a surface wave traveling along a flat surface for nearly all angles of incidence (except for a small amount of BSWS), the ISC would be the technique of choice.

Moving on and inspecting the level of phase agreement (Figure 6.14–6.17) it was reaffirmed that both the ISC and ASC performed very well with minimal differences for all θ_i, but with the ASC technique having a slight advantage. In a final attempt to further simplify and compare the overall scattering characteristics of the cloaks the mean absolute error (6.4) was introduced and implemented to account for 13 different angles of incidence (Figure 6.18,6.19). Here it was demonstrated that the ISC was the superior candidate when it came to minimizing $|\mathrm{E}_z|$ disagreement for all θ_i (relative to the ideal flat surface) and the ASC was the superior candidate when it came to minimizing $\phi(\mathrm{E}_z)$ disagreements, also for all θ_i. Lastly, as an added degree of quantification, a 'classification algorithm' was introduced that allowed for the unique weighting of the FSWS and BSWS error values as seen in (6.5). In doing so, it was revealed that the ASC was the superior candidate with regards to BSWS in terms of both $|\mathrm{E}_z|$ and $\phi(\mathrm{E}_z)$ agreement (Figure 6.20, 6.21). After applying the same weighting to the FSWS it was demonstrated that ISC was the superior candidate with regards to $|\mathrm{E}_z|$, but the ASC was the superior candidate with regards to $\phi(\mathrm{E}_z)$. The comparative study described in this chapter is unique because it is the first of its kind to directly compare two disparate surface wave cloaking techniques through the use a performance metric (i.e. MAE and weighted MAE) that is specifically crafted to encapsulate the important characteristics of surface wave cloaks.

Chapter 7

Conclusions and Future work

7.1 Conclusions

The aim of the work presented in this thesis was to derive, implement and validate different techniques to manipulate electromagnetic (EM) surface waves on non-Euclidean geometries via transformation optics (TO). The techniques borne out of this work included a unique application of Fermat's principle as well as a fundamental ground-up derivation used to link curved and flat surfaces. The first technique called for an electrically thin isotropic material overlay whereas the second called for an anisotropic one. Central to both of these methods was the geometrical optics (GO) approximation meaning that the surface deformations under investigation were electrically large. Lastly, a large part of this work involved the development and testing of a novel suite of numerical tools that were used to solve for the required device properties.

In Chapter 3 a new method (fundamentally different from previous methods proposed by transformation plasmonics [43, 80]), utilizing Fermat's principle, was used to create an omnidirectional, purely dielectric, electrically thin material overlay to cloak a finite, curved (i.e. non-Euclidean) surface deformation from surface waves in the microwave regime. First its derivation, was produced and a number of sample surface deformations (hemispheric, conic and Gaussian) were studied. Then, a numerical solution was derived to account for any limitations found in the analytical approach when $R(\theta)$ (which was related to the profile of a given surface deformation) could not be expressed in a closed-form. Next, a parallel plate waveguide simulation technique was introduced and the performance of a hemispheric, conic and Gaussian cloak was investigated using a full-wave electromagnetic solver (COMSOL 5.0). Here it was demonstrated that the curvature, K, mismatch between the surface deformation and the flat approach plane would lead to undesirable scattering and because of this, particular focus was placed on surfaces that did not have this problem (i.e. the cosine-shaped surface). To further

quantify the performance of each cloak, a sampling line study was carried out and it was determined that the Guassian cloak most closely emulated the wave behavior of a plane wave traveling in a flat waveguide.

Next, to convert the proposed material solution from its parallel plate waveguide form into a real surface wave form, the required material parameters (i.e. ε_r) for a thin material on a PEC ground plane were determined via the use of an eigenmode solver in CST Microwave Studio 2014. These results where then used to design an all-dielectric material overlay of uniform thickness, that would cloak a cosine-shaped surface deformation (whose profile can be found in the Appendix) from a surface wave. The proposed device was then simulated using the time domain solver in CST Microwave Studio 2014 and it was demonstrated that the surface wave cloak design functioned properly in the desired frequency band and possessed a good level of modal confinement. The surface wave cloaking design recipe described in this chapter is novel because it leads to the creation of a thin, isotropic, all-dielectric material overlay that can be used to cloak a rotationally symmetric surface deformation for all angles of incidence and over a given frequency band.

In Chapter 4 a realizable method for mapping flat, isotropic, surface wave lens onto rotationally symmetric surface deformations was proposed. First, the design recipe first used in Chapter 3 was expanded to allow for the mapping of flat refractive index profiles onto rotationally symmetric surfaces. To demonstrate how one does this, a number of analytical examples were gone through step-by-step which included the mapping of: a black hole lens onto a hemispheric deformation, a Luneburg lens onto a conic deformation, a Luneburg lens onto a hemispheric deformation and a MFE lens onto a hemisphere. The final case of attempting to map a MFE lens onto a hemispheric surfaces lead to the idea of an 'equivalent surface', which in its simplest sense was a curved homogeneous surface that behaved, electrically speaking, in the same fashion as its flat, inhomogeneous analogue. A general method for obtaining the equivalent surface of a flat lens was then derived and the relation between a hemispheric deformation and a MFE lens was used to check its validity. A numerical solution for mapping lenses onto curved surfaces was later derived for instances where $R(\theta)$ of a given rotationally symmetric surface was not expressible in closed-form. Moving on, the parallel plate waveguide simulation technique introduced in Chapter 3 was implemented again. Here the performances of a Luneburg lens and a MFE lens in a number of configurations were investigated using a full-wave electromagnetic solver (COMSOL 5.0). It was demonstrated (as was also witnessed in Chapter 3) that the curvature, K, mismatch between the surface deformation and the flat approach plane lead to undesirable pattern characteristics. Of all the curved surface lens configurations those that avoided these curvature discontinuities functioned (emulated the behavior of their flat

lens analogues) the best.

Finally, in an attempt to convert the proposed material solution from its parallel plate waveguide form into a real surface wave form, the required material properties for a thin material overlay on a PEC ground plane were determined. Here instead of maintaining the thickness of the material overlay and varying ε_r as was done in Chapter 3, the opposite was done were ε_r is maintained ($\varepsilon_r = 15$) and the thickness of the material overlay was varied according to a calculated relation between material thickness and modal refractive index. This design strategy was particularly interesting as it could be realized via the increasingly accessible rapid fabrication technique of 3D printing. To demonstrate the efficacy of the proposed designs they were simulated using the time domain solver in CST Microwave Studio 2014. Here it was demonstrated that the material realizations of the Luneburg lens and the MFE lens on a cosine-shaped surface deformation functioned properly withing a desired frequency band. These simulation results also revealed a good level of modal confinement across said band as well. The curved surface wave lens design recipe described in this chapter was novel in that it called for the creation of a thin, isotropic, homogeneous material overlay that can be used to control the propagation of surface waves along nearly any smooth rotationally symmetric PEC surface deformation.

In Chapter 5 the structural limitations found in Chapter 3 and Chapter 4, namely the required rotational symmetry of the surface deformation, were addressed. In order to do so, a fundamentally different approach needed to be considered that could deal with rotationally asymmetric surfaces (RASs) . First, in the case of the illusion device (a flat materially inhomogeneous device that emulates the scattering characteristics of a curved homogeneous device), a ground-up derivation was developed and the prescribed material properties for a sample surface (an asymmetric Gaussian deformation) were discussed. Then, moving onto the cloaking of a RAS, where to start a rotated plane was considered, another ground-up derivation was provided to cloak smooth surface deformations. Afterwards, a numerical solution was developed to handle computer-aided design (CAD) surfaces, and the validity of the proposed technique was tested in both one and two dimensions.

In order to validate that the prescribed material loadings borne out of the proposed techniques do in fact create the desired devices, the parallel plate waveguide simulation technique used in Chapter 3 was implemented in a full-wave electromagnetic solver (COMSOL 5.0). Here it was demonstrated that the scattering characteristics of the RAS could be faithfully recreated by an illusion device. To quantify just how well the illusion device was functioning a sample line study was conducted and it was found that an excellent level of agreement existed between the curved RAS and the flat illusion device. Next, the numerical technique found within this chapter was used to calculate

the required material properties to create an illusion device for a CAD surface, and it was demonstrated that it successfully recreated the scattering characteristics of its curved analogue for two different angles of incidence. Lastly, the same RAS used in the analytically defined illusion device case study was shown to be completely cloaked for two different angles of incidence and the efficacy of cloak itself was quantified by analyzing the field distribution along two different sample lines (one for each angle of incidence). Owing to the material complexity of the proposed devices in this chapter, it is noted that obtaining a true surface wave device, though outside the domain of this thesis, may be possible using a variety of different techniques that are currently proposed within the metasurface community. The surface wave illusion and cloaking design recipe described in this chapter is novel because it can be directly applied to nearly any smooth surface (whether its form is known analytically or in the form of a CAD file, hence the term 'general'), as well as the fact that all the devices borne out of it are omnidirectional.

Chapter 6 described a direct, comparative study between the surface wave cloaking techniques introduced in Chapter 3 and Chapter 5. The cloak from Chapter 3 was refereed to as an isotropic surface wave cloak (ISC) and the cloak from Chapter 5 was referred to as an anisotropic surface wave cloak (ASC), due to the material properties called for in the two techniques. Owing to the limiting factor of rotational symmetry inherent to the ISC approach, a surface deformation that can be handled by both techniques was examined. The simulation method used in the previous chapters was implemented and the performance of both of the cloaks for multiple angles of incidence was analyzed. As the two cloaks behaved virtually identically when inspecting the amplitude of their scattered E-field, focus was instead put on the performance of their scattered magnitude and phase. In doing so, clear distinctions were made between the two different methods. To add a more robust quantification of the surface wave cloaks performance, the idea of a 'bounding ring' was introduced. The latter was designed to capture the omnidirectional scattering of the surface deformations. Finally, in an attempt to quantify the performance of a surface wave cloak with a single value, a mean absolute error calculation was performed and the results for the different cloaking techniques were analyzed. The comparative study described in this chapter is unique because it is the first of its kind to directly compare two disparate surface wave cloaking techniques through the use a performance metric (i.e. MAE and weighted MAE) that is specifically crafted to encapsulate the important characteristics of surface wave cloaks.

7.2 Future Work

7.2.1 Generalized equivalent surfaces

In Chapter 4 the idea of an equivalent surface for surface waves was developed. A simple example of such a surface is the hemisphere which turned out to be the equivalent surface of Maxwell's fish-eye lens (MFL). Taking advantage of this equivalence between the refractive index, n, and a surface's profile, $z(r)$, may allow for the development of equivalent surfaces for otherwise difficult to obtain refractive indices. Advancing this idea a step further, would involve the study of surfaces (assuming they exist in the first place) that emulate the anisotropic material behaviors called for by the devices presented in the Chapter 5. This research could prove to be particularly useful from an applications perspective, because any equivalent surfaces borne out of it would be easily realizable through ever-advancing 3D printing techniques.

7.2.2 Volumetric quasi-conformal transformation optics

Earlier versions of quasi-conformal transformation optics (QCTO) schemes ([37, 45]) implicitly relied on the volume under investigation to be either rotationally or axially symmetric. In turn, the problem was effectively reduced to comparing the cross sections of volumes. From a computational perspective this makes the generation of the necessary mesh (what the TO formalism acts upon) very straightforward and this technique has been successfully exploited by a number of researchers [52, 53, 55, 81]. If however, one wants to deal with volumes that lack any discernible symmetries, then a different technique (one based on elemental volumes and not areas) needs to be developed. First, a 'volumetric quasi-conformal transformation optics' (VQCTO) formalism, which is simply a dimensional expansion of the QCTO approximation, is introduced

$$\varepsilon_p \approx \frac{\Delta x_v \Delta y_v \Delta z_v}{\Delta x_p \Delta y_p \Delta z_p} \varepsilon_v, \tag{7.1}$$

where the subscripts v and p denote the virtual and physical spaces, respectively. Before this scheme can be tested, however, a systematic approach for creating discretized volumetric meshes is investigated. To start, a rotationally symmetric structure, Υ, is created in a CAD client (COMSOL 4.4) (see Figure 7.1). Next, the CAD generated lens is exported in the form of a .stl file (a formatting language which represent objects via a triangular tessellation), into Pointwise (see Figure 7.2) which is a commercially available mesh generation software package. Given that Υ is a rotationally symmetric volume, it will have a 'symmetry primitive' (Figure 7.3) residing within its tessellated structure, which can be treated in the same fashion as the traditional cross section used in previous

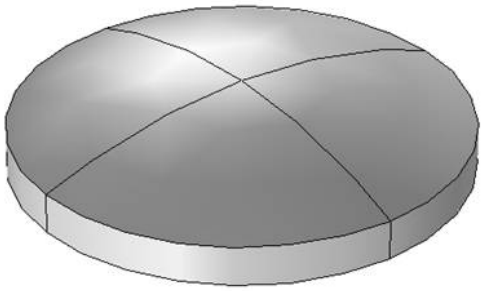

Figure 7.1: Classic biconvex lens in COMSOL 4.4.

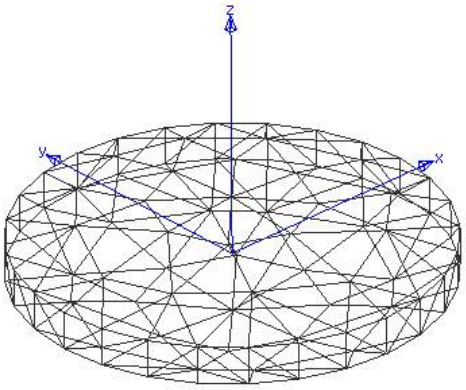

Figure 7.2: Imported tessellated biconvex lens.

QCTO schemes. After ensuring that no cells are too geometrically anisotropic (cells

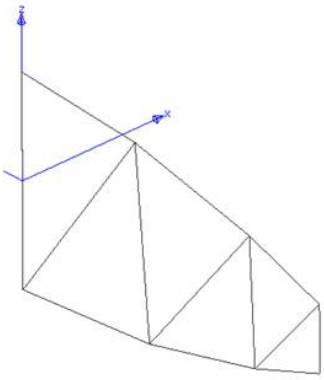

Figure 7.3: Symmetry primitive of biconvex lens.

are at least rectangular) and in turn that most cells are comprised predominately of right angles (a key feature in the conformal (angle preserving) argument), the surface mesh is extruded from $0 \leq \theta \leq \frac{\pi}{2}$ (Figure 7.4) to create a domain (volumetric mesh). It should be noted that in order to extrude the cross section, the primitive needs to be

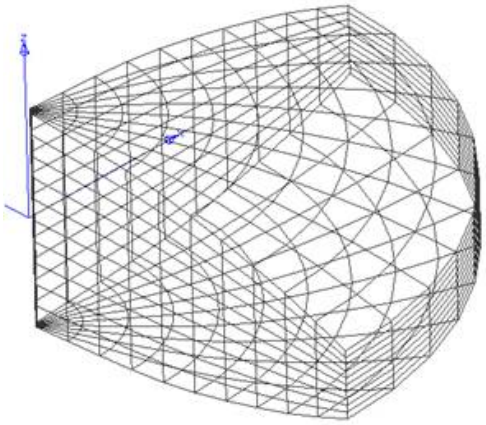

Figure 7.4: Extruded domain based on biconvex lens symmetry primitive.

displaced a very small distance away from the origin. This is necessary because in order for the extrusion process to be successful, the hexahedrons that constitute the domains closest to the axis need to have a finite dimension. Put another way, all hexahedrons that constitute a domain need to have six sides, and by not displacing the primitive in Figure 7.3 a number of hexahedrons would only have 5 sides, thereby causing the domain to be incorrect. Moving on, the domain in Figure 7.4 is then exported as a

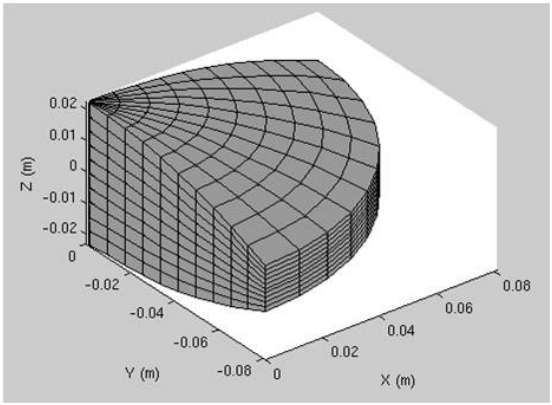

Figure 7.5: Domain creation in MATLAB.

.wrl file (a format traditionally found in the Virtual Reality Modeling Language) into a MATLAB script which is coupled with COMSOL MATLAB LiveLink to produce 'hexahedron objects.' These hexahedrons are treated as actual Java objects that have their own unique features such as coordinates, ε_r, σ, and other attributes that can be assigned to each hexahedron within COMSOL. The imported and discretized quarter of Υ, is displayed in Figure 7.5. Next, the domain is imported into COMSOL 4.4, via MATLAB LiveLink (Figure 7.6) and revolved twice to produce Υ_d, the complete

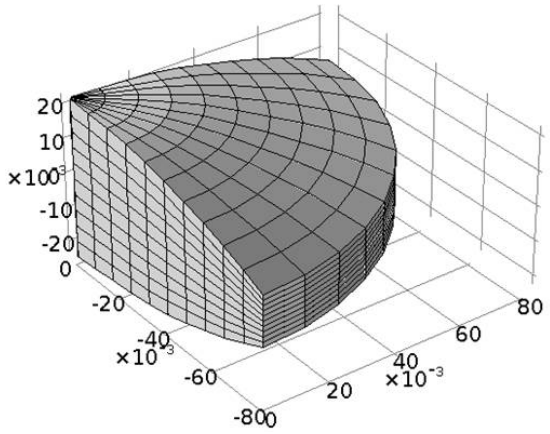

Figure 7.6: Imported discretized structure in COMSOL 4.4.

discretized version of Υ (see Figure 7.7). Having created a quasi-conformal discretized

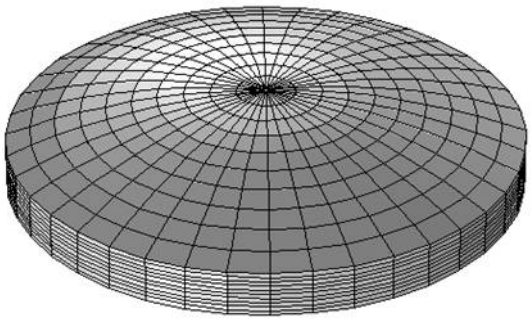

Figure 7.7: Discretized biconvex lens in COMSOL 4.4.

volume, Υ_d, from Υ, it is now possible implement the proposed VQCTO algorithm.

As a test of the proposed technique, a simple volumetric transformation is studied. First, a virtual space (Figure 7.8(a)), regarded here as a virtual volume (V_v) and a physical space (Figure 7.8(b)), V_p are chosen. V_v is a simple hyperbolic lens designed for use in the microwaves regime ($f_0 = 30.0$ GHz) with a diameter, $D = 63.5$ mm, a central thickness, $t = 20.0$ mm, and homogeneous material loading of $\varepsilon_{r,v} = 2.6$. V_p is another hyperbolic lens, with the same f_0 and D, but at half the thickness ($t_p = 10.0$ mm). This halving of the thickness of the V_p is simply a scaling by a factor of $\frac{1}{2}$ in the $\underline{k}$-direction, and from Fermat's principle one would expect to have to double the relative permittivity ($\varepsilon_{r,p} = 2\varepsilon_{r,v}$) of the new lens to account for this. Obviously, this simple relation does not take into account such things as impedance mismatch, but it does provide a general guide for what the value of $\varepsilon_{r,p}$, as calculated by the VQCTO algorithm, should be.

Utilizing the same procedure outlined above to descritize a biconvex lens, produces

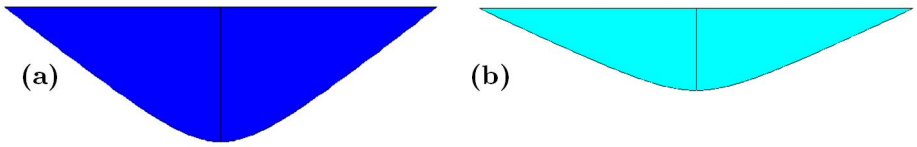

Figure 7.8: Hyperbolic lens acting as the virtual space (V_v) (a), and a scaled hyperbolic lens acting as the physical space (V_p) (b).

the lens displayed in Figure 7.9. The range of $\varepsilon_{r,p}$ values that are solved for by the

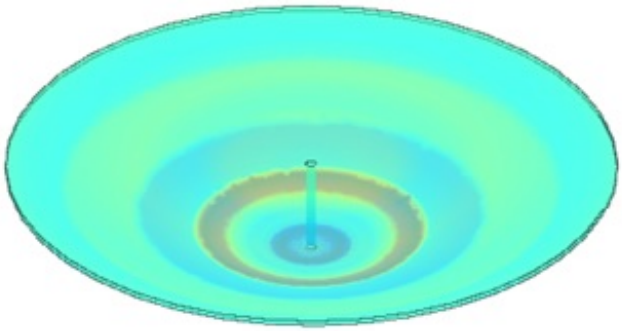

Figure 7.9: Scaled hyperbolic lens (V_p) with material loading determined by VQCTO algorithm.

VQCTO algorithm are displayed in the inset of Figure 7.10. On the whole, it appears that the scaled lens is primarily comprised of hexahedrons with $\varepsilon_{r,p} \approx 5.2$. In fact, inspecting the distribution of $\varepsilon_{r,p}$ within a quadrant of the scaled lens (Figure 7.10), reveals that $\mu = 5.14$ and $\sigma = 0.43$, where μ and σ represent the mean and standard deviation for a normal distribution, respectively. Equally important, this figure reveals

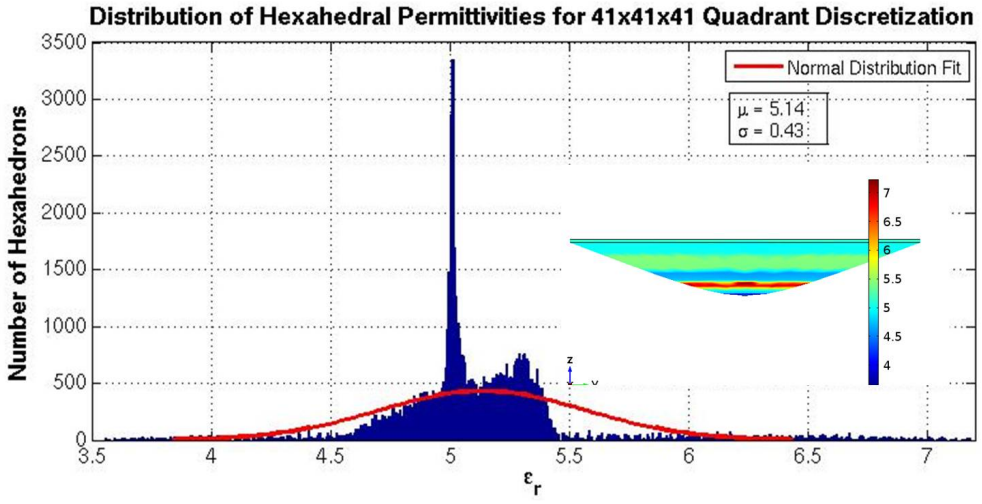

Figure 7.10: $\varepsilon_{r,p}$ distribution for V_p

that the number of hexahedrons that deviate from this expected value is in fact very small, something that the red band of material found in the inset of Figure 7.10 would lead one to conclude otherwise. The next step would involve simulating V_p with the prescribed $\varepsilon_{r,p}$ in a full-wave EM solver, and comparing its performance to the virtual lens, but the results shown in Figure 7.10 indicate that the VQCTO algorithm merits further investigation.

Ultimately, the true purpose of the VQCTO approach would be deal with volumes that lack any discernible symmetry or are effectively of an arbitrary shape, as long as the 'footprint' of the two volumes remains fixed. An example of such an 'arbitrary volume' is displayed in Figure 7.11(a), which would act as the virtual space, V_v. Figure

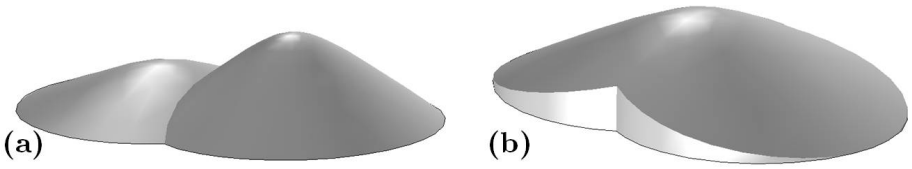

Figure 7.11: An axially asymmetric lens (a) and an axially symmetric lens (b).

7.11(b) is an axially symmetric lens that will act as the physical space (V_p) and will eventually be loaded with the necessary $\varepsilon_{r,p}$ to emulate the behavior (focusing, scanning, etc.) of V_v. Just as was done in the case of the biconvex lens, both volumes need to be prepared (Figure 7.12) before they can be discretized. This entire process involves three distinct 'dissection' steps in which a total of six faces need to be generated per partition. The first step is called 'coring' were a cylinder of arbitrarily small radius ($\lambda_0/100$ in this example) is removed from the host volume. Note, the location of the center of the core (x_0, y_0) must be the same in V_v and V_p as it ensures that eventual generated discretized volumes reside above the same regions in the XY-plane. Also, the coring step is implemented as a means to create one of the necessary faces needed for the final 'dissection' of the volume. For the next step, an edge of finite thickness is created along the boundary of the host volume. This is accomplished by adding an arbitrarily thin ($\lambda_0/100$) layer to the bottom of both volumes where they are closest to the XY-plane. This step also, generates a required face for the 'dissection' process. The result of these operations on V_v and V_p are displayed in Figure 7.12(a) and Figure 7.12(b), respectively. The third and final step in the 'dissection' of the volumes is the projection of space curves onto V_p and V_v which effectively define the partition in the XY-plane. This final step produces the remaining four faces per partition needed to successfully create the desired volumetric meshes. Volumetric meshes of the same color in Figure 7.13 represent corresponding partitions between the two volumes. In

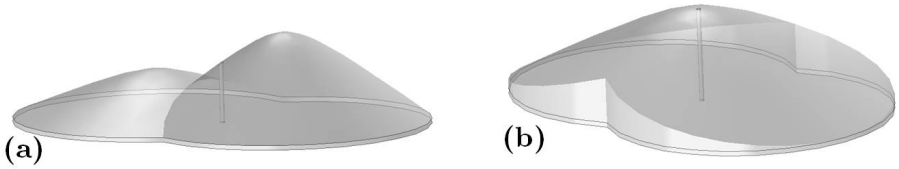

Figure 7.12: A 'prepared' axially asymmetric lens (a) and a 'prepared' axially symmetric lens (b).

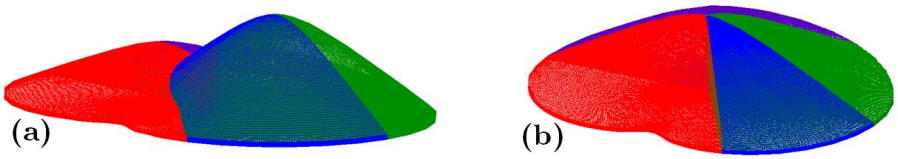

Figure 7.13: Proposed volumetric meshes for an axially asymmetric lens (a) and an axially symmetric lens (b).

this particular example, four partitions are chosen for illustrative purposes, but any number of partitions could be implemented as long as the resulting six faces could be readily identified to create the required volumetric meshes. In future investigations, the next step would be to implement (7.1), load V_p accordingly and simulate the structure with a full-wave EM solver to see if it does in fact behave (electrically speaking) the same as V_v. If this approach proved to be a valid approximation, VQCTO could allow engineers to create new and interesting all dielectric lenses, among other unique devices.

7.2.3 Nonorientable surfaces

Following on from the work done in Chapter 5, is a unique group of parametrically defined surfaces: nonorientable surfaces [122]. Such surfaces, as the name implies, are surfaces who lack a defined orientation, where orientabilty can manifest itself (among other ways) in the behavior of the unit normal vector, $\hat{\mathbf{n}}$, along a closed path on a surface. An example of an orientable surface is a sphere [123] where, depending on how the unit normal is defined, is always pointing in to or out of the sphere. The important feature here is that there exists no closed path on a sphere along which $\hat{\mathbf{n}}$ does not obey this rule, thereby making it an orientable surface. This does not, however, occur for surfaces such as a Möbius strip [124] (Figure 7.14) where the orientation of $\hat{\mathbf{n}}$ along a particular closed path will not exhibit this behaviour owing to its inherent 'one-sidedness.' This unique geometric feature may have RF engineering applications for such things as antenna miniaturization, or manipulating the polarization of EM waves along a surface, as has already been explored for photonic devices [125]. Another

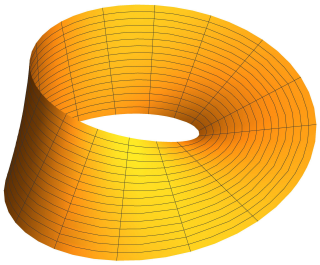

Figure 7.14: Isometric view of a Möbius strip in Mathematica 10.

well known nonorientable surface is the Klein bottle [126] (Figure 7.15) which has no inside or outside. This geometric feature, may also have some interesting engineering applications though it is worth pointing out that there are no unbounded nonorientable surfaces which do not intersect themselves [127] and this limitation will need to be kept in mind when contemplating fabricating such devices.

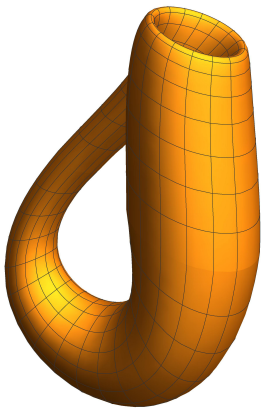

Figure 7.15: Isometric view of a Klein bottle in Mathematica 10.

Chapter 8

Publications and presentations

8.1 Publications and presentations

8.1.1 Refereed papers

- 'Isotropic and anisotropic surface wave cloaking techniques,' McManus, T. M., La Spada, L. and Hao, Y., *Journal of Optics*, accepted October 30, 2015. Contributions: Initial idea, theoretical derivations, numerical modeling, data post-processing and manuscript preparation.

- 'Illusions and cloaks for surface waves,' McManus, T. M., Valiente-Kroon, J. A., Horsley, S. A. R. and Hao, Y., *Scientific Reports*, **4**, 5977 (2014) doi 10.1038/srep05977.

- 'Lenses on curved surfaces,' Mitchell-Thomas, R.C., Quevedo-Tereul, O., McManus, T. M., Horsley, S. A. R. and Hao, Y., *Optics Letters*, **39**, Issue 12, 3551-3554 (2014) doi 10.1364/OL.39.003551.

- 'Perfect surface wave cloaks,' Mitchell-Thomas, R.C., Quevedo-Tereul, O., McManus, T. M., Horsley, S. A. R. and Hao, Y., *Phys. Rev. Lett.*, **111**, 213901(2013) doi 10.1103/PhysRevLett.111.213901.

8.1.2 Conference papers

- 'The anti-fish eye cloak for surface wave antennas,' Mitchell-Thomas, R. C., Quevedo-Tereul, O., McManus, T. M., Horsley, S. A. R. and Hao, Y., *Proceedings of the 8th European Conference on Antennas and Propagation*, 267-268, The Hague, Netherlands, April 6-11 (2014) doi 10.1109/EuCAP.2014.6901742.

- 'Conformal surface lenses from a bed of nails,' Quevedo-Tereul, O., Mitchell-Thomas, R. C., McManus, T. M., Horsley, S. A. R. and Hao, Y., *Proceedings of*

the 8th European Conference on Antennas and Propagation, 269-270, The Hague, Netherlands, April 6-11 (2014) doi 10.1109/EuCAP.2014.6901743.

- '2D optical transformations for surfaces,' Mitchell-Thomas, R. C., McManus T. M., Quevedo-Tereul O. and Hao, Y., *2014 IEEE Antennas and Propagation Society International Symposium*, 761-762, Memphis, Tennessee, U.S.A., July 6-11 (2014) doi 10.1109/APS.2014.6904710.

8.1.3 Oral presentations

- 'Asymmetric flat reflector from transformation optics,' McManus, T. M., Yang, R., Quevedo-Teruel, O. and Hao, Y., *Proceedings of the 7th European Conference on Antennas and Propagation*, 1836 - 1839, Gothenburg, Sweden, April 8-12 (2013).

- 'Current research efforts in transformation optics (non-Euclidean geometries) at QMUL', McManus, T. M., and Hao, Y., United States Army Research Lab, Aberdeen Proving Ground, Maryland, U.S.A., September 4-5 (2013).

- 'A generalized dipole moment based approach for modelling of nanoparticles,' Naeem, M., McManus, T. M., and Hao, Y., *The 30th International Review of Progress in Applied Computational Electromagnetics*, Jacksonville, Florida, U.S.A., March 23-27 (2014).

8.1.4 Poster presentations

- 'Surface and volumetric mesh generation for TO applications', McManus, T. M., and Hao, Y., *Spatial transformations: from fundamentals to applications*, The Royal Society at Chicheley Hall, U.K., January 26-27 (2015).

- 'Surface and volumetric mesh generation/manipulation for transformation optics applications', McManus, T. M., and Hao, Y., *QMUL Electronic Engineering and Computer Science Research Showcase*, London, U.K., April 22 (2015).

8.1.5 Awards

- 'Winner of the Best Antenna Group Poster Award', McManus, T.M., and Hao, Y., *QMUL Electronic Engineering and Computer Science Research Showcase*, London, U.K., April 22 (2015).

8.1.6 Oral presentations and posters - QUEST

The research covered in this thesis is part of the QUEST (Quest for Ultimate Electrogmagnetics using Spatial Transformations) projects which was a five-year, multidisciplinary, EPSRC programme (grant number: EP/I034548/1 [128]). The universities involved included Queen Mary University of London, Exeter University, St. Andrew's University and Oxford University. Over the three years of funding that constitute this thesis bi-monthly reports (a total of 16) were submitted for review by the programmes external board. Also, during this time four poster presentations and four oral presentations, outside of those mentioned above, were given in Oxford, Exeter and London.

Appendix A

Appendix

A.1 Fundamentals of tensor analysis

A.1.1 Raising and lowering indices

Given a contravariant vector, k_i, it is possible to determine the covariant vector, k^i by taking the inner product of the metric tensor g_{ij} and k_i

$$k_i = g_{ij}k^j, \tag{A.1}$$

which effectively 'lowers' a contravariant index to a covariant index. To 'raise' a covariant index to a contravariant one, one performs

$$k^i = g^{ij}k_j. \tag{A.2}$$

The indices of a general tensor can be raised and lower as follows

$$R_{ijkl} = g_{im}R^m{}_{jkl}, \quad R^i{}_j{}^k{}_l = g^{km}R^i{}_{jml}. \tag{A.3}$$

A.1.2 Covariant and contravariant derivatives

Let ψ be a scalar field in space described by coordinates x^i, then the partial derivative of ψ with respect to x^i can be represented as

$$\frac{\partial}{\partial x^i}\psi \equiv \partial_i\psi \equiv \psi_{,i}. \tag{A.4}$$

Therefore, a comma means partial differentiation, with the index following it giving the coordinate with respect to which the derivative is taken. This type of differentiation is referred to as covariant differentiation. Focusing now on vector fields, let $\boldsymbol{V} = V^i\boldsymbol{e}_i$,

meaning that $\boldsymbol{V}$ consists of the sum of products of scalar fields, V^i, and basis vector fields, $\boldsymbol{e}_i$. Using the chain rule,

$$\frac{\partial}{\partial x^i}\boldsymbol{V} = \frac{\partial V^j}{\partial x^i}\boldsymbol{e}_j + V^j\frac{\partial \boldsymbol{e}_j}{\partial x^i}. \tag{A.5}$$

As the derivative of a vector is a vector itself, $\partial \boldsymbol{e}_j/\partial x^i$ can be expanded as

$$\frac{\partial \boldsymbol{e}_j}{\partial x^i} = \Gamma^k{}_{ji}\boldsymbol{e}_k, \tag{A.6}$$

where $\Gamma^k{}_{ji}$ is a Christoffel symbol of the second kind, which is defined as

$$\Gamma^k{}_{ji} = g^{kr}\Gamma_{jir}, \tag{A.7}$$

where Γ_{jir} is the Christoffel symbol of the first kind which is defined as

$$\Gamma_{jir} \equiv \frac{1}{2}\left[\frac{\partial}{\partial x^j}\left(g_{ir}\right) + \frac{\partial}{\partial x^i}\left(g_{rj}\right) - \frac{\partial}{\partial x^r}\left(g_{ji}\right)\right]. \tag{A.8}$$

Substituting (A.6) into (A.5) and relabeling the summation indices, (A.5) is recast as

$$\begin{aligned}\frac{\partial}{\partial x^i}\boldsymbol{V} &= \left(V^j_{,i} + \Gamma^j{}_{ki}V^k\right)\boldsymbol{e}_j \\ &\equiv V^j_{;i}\,\boldsymbol{e}_j,\end{aligned} \tag{A.9}$$

meaning that $V^j_{;i} = V^j_{,i} + \Gamma^j{}_{ki}V^k$. The two-index tensor with components $V^j_{;i}$ is called the contravariant derivative of $\boldsymbol{V}$ and this differentiation accounts for the variation of both vector components as well as the basis vectors.

A.1.3 The Riemann tensor

The Riemann curvature tensor is defined as

$$R^i{}_{jkl} \equiv \Gamma^i{}_{jl,k} - \Gamma^i{}_{jk,l} + \Gamma^i{}_{mk}\Gamma^m{}_{jl} - \Gamma^i{}_{ml}\Gamma^m{}_{jk}. \tag{A.10}$$

Two other quantities relating to curvature are obtained by contracting the indices of $R^i{}_{jkl}$, namely the Ricci tensor which is defined by

$$R_{ij} = R^k{}_{ikj}, \tag{A.11}$$

and by contraction of the indices of the Ricci tensor, the curvature scalar which is defined by

$$R = g^{ij} R_{ij} = R^{i}{}_{i} = R^{ij}{}_{ij}. \tag{A.12}$$

Lowering the upper index of (A.10) produces the Riemann tensor of the first kind which is defined by

$$R_{ijkl} = \frac{1}{2}\left(g_{il,j,k} - g_{ik,j,l} + g_{jk,i,l} - g_{jl,i,k}\right) + g_{mn}\left(\Gamma^{m}{}_{il}\Gamma^{n}{}_{jk} - \Gamma^{m}{}_{ik}\Gamma^{n}{}_{jl}\right). \tag{A.13}$$

A.1.4 Derivative notation, divergence, curl and Laplacian

$$\nabla_i V^i \equiv V^{j}_{\;;i} \tag{A.14}$$

$$U_{i;j} \equiv \nabla_j U_i \equiv U_{i,j} - \Gamma^{k}{}_{ij} U_k \tag{A.15}$$

$$\underline{\nabla} \cdot \underline{V} = \frac{1}{\sqrt{g}} \partial_i \sqrt{g} V^i, \quad \text{where } g = \det \boldsymbol{g} \tag{A.16}$$

$$(\underline{\nabla} \times \underline{V})^i = \epsilon^{ijk} V_{k,j}, \quad \text{where } \epsilon_{ijk} = \pm\sqrt{g}[ijk] \tag{A.17}$$

$$(\underline{\nabla} \times \underline{V})_i = \epsilon_i{}^{jk} V_{k,j} \tag{A.18}$$

$$\underline{\nabla}^2 \underline{V} = V^{i}_{\;;j}{}^{;j} \underline{e}_i = \nabla_j \nabla^j V^i \underline{e}_i, \quad \text{where } \underline{e}_i \text{ is a basis vector field} \tag{A.19}$$

A.2 Rotationally symmetric surface wave cloak profile

x (mm)	$z(x)$ (mm)
0	17.1429
7.2103	15.3392
11.3966	12.8789
14.1086	10.924
16.7486	8.8810
20.4559	6.0099
25.1931	2.8067
34.2857	0

Table A.1: Surface deformation profile used in rotationally symmetric surface wave cloak realization found in Chapter 3. Here x represents the distance from the center of the deformation and z a points elevation above the flat approach plane.

A.3 VQCTO numerical solution

Chapter 7 proposed the idea of volumetric quasi-conformal transformation optics (VQCTO) and at the heart of this work was structured volumetric meshing and manipulation. Here the term 'structured' mesh refers to a collection of hexahedron cells. The actual generation of these meshes was discussed briefly in Chapter 7, but the exact numeric solution implemented to determine the volumes (and in turn the material properties of entire lenses) of each individual hexahedron (hex) cells is discussed here. Just as was the case for the structured surface mesh discussed in Chapter 5, a case study was first investigated to make sure that the proposed method of calculating the volume of an arbitrary hex was valid.

A.3.1 Hexahedral volume calculation

To start a simple volume (a quartered sphere of unit radius) is investigated (see Figure A.1. The structured volumetric mesh of this sphere was generated by the same extruded-surface-mesh technique used to generate the structured volumetric meshes used in Chapter 7. Having created the mesh, two different means of calculating the volume of a hex cell are investigated. In the first technique, the hex cell is assumed to be a cuboid which means its volume can be calculated as

$$V_{cube1} = a_1 b_1 c_1 \tag{A.20}$$

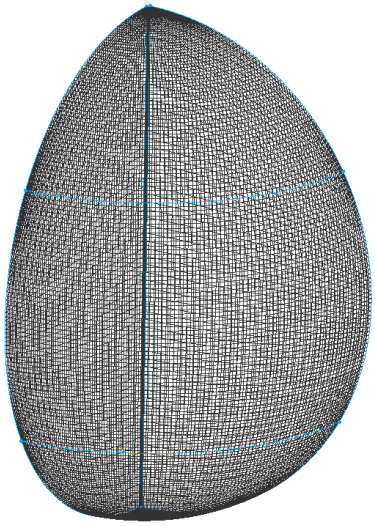

Figure A.1: Quartered sphere of unit radius used in structured volumetric case study.

where a_1, b_1 and c_1 are defined in Figure A.2. Taking into consideration that the

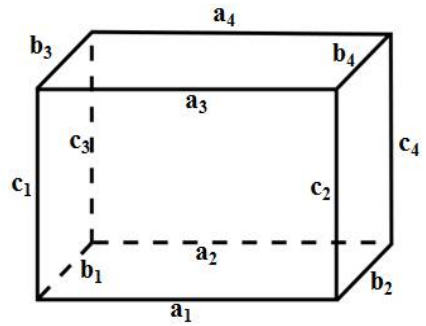

Figure A.2: Naming scheme for cuboid volume calculation (A.20).

elemental volume as defined in (A.20) is highly sensitive to skewed elements, another volume (located at the opposite edge of the cuboid) is studied as well $V_{cube4} = a_4 b_3 c_3$. Sensitivity aside, this algorithm is comparatively simple to implement and provides a nice 'base level' to gauge the performance of another volume calculating algorithm.

The second technique used in this study is the long diagonal method [129] which decomposes the hex cell into six tetrahedra after predetermining a logical cut-plane, and defining there volumes as the sum of three (3 x 3) determinants as is done in

$$\begin{aligned} 6V_{hex} = &|\underline{r}_H - \underline{r}_A, \underline{r}_B - \underline{r}_A, \underline{r}_F - \underline{r}_D| + \\ &|\underline{r}_H - \underline{r}_A, \underline{r}_C - \underline{r}_A, \underline{r}_D - \underline{r}_G| + \\ &|\underline{r}_H - \underline{r}_A, \underline{r}_E - \underline{r}_A, \underline{r}_G - \underline{r}_F|\,, \end{aligned} \tag{A.21}$$

where the points $(A, B, C...)$ are defined in Figure A.3. Having introduced two distinct

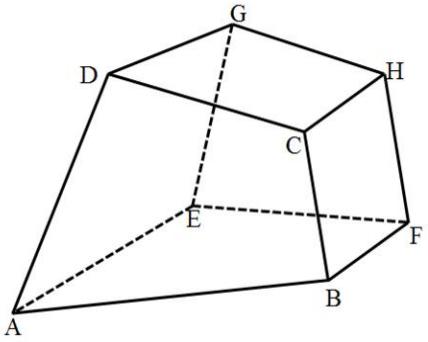

Figure A.3: Naming scheme for hexahedron volume calculation (A.21).

methods of determining the elemental volumes used in the structured meshes, their accuracy is put to the test in the form of calculating the total volume of a quartered sphere of unit radius ($V_{tot} = \pi/3 \approx 1.05$). Figure A.4 displays the results of calculating the total volume of said sphere using different sized meshes. Starting with the very first

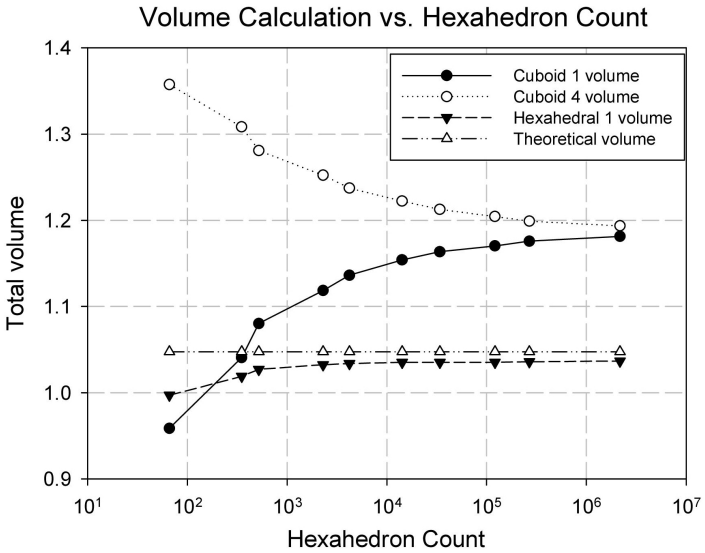

Figure A.4: Calculating the total volume of a quartered sphere using different elemental hexahedra approaches.

set of points on the far left of Figure A.4, which represent a very coarse mesh (≈ 80 hexahedra), it is apparent that both techniques are inaccurate and a finer mesh needs to be implemented. Doing so for a number of different hex counts reveals an interesting trend. Starting with the data that corresponds to Cuboid 1 volume (as defined in (A.20)) it is noted that it never (even for extremely fine mesh configurations) converges to the correct value for V_{tot}, though it does come somewhat close for a hex count of about

600. This 'near-correct' calculation for V_{cube1} is a result of the technique converging to its final value and just so happening to pass very close to V_{tot} while doing so. This same behavior (of converging to an erroneous value for V_{tot}) is displayed by the results for V_{cube4}. Here, the only difference is that due to the skewing the hex elements, it starts off at a far more inaccurate calculation for V_{tot}. The results for both V_{cube1} and V_{cube4} are to be expected considering that they do not accurately capture the facets of the hex elements themselves, something that V_{hex} clearly does.

Even at the coarsest mesh setting, V_{hex} outperforms both of the cuboid approximations and it rapidly converges to a value very close to V_{tot} as the mesh is refined. At about 10,000 hex cells, however, the value for V_{hex} does not converge to V_{tot} and the reason for this is due to a fundamental and well understood limitation of the long diagonal method. The reason for this is that depending on the how the hex cell is diagonalized ($(\underline{r}_H - \underline{r}_A)$ in this study) will influence the calculation of its volume to some extent. Put more precisely, if a hex cell is not too skewed along any one of its edges, one would expect very minimal influence caused by the selection of the diagonal because all such diagonal that can be formed in the hex cell are of about the same length. However, when a hex cell is skewed along one direction and the chosen diagonal fails to take this into account one will see volumes that are either less than or greater than the correct actual value for the volume as is demonstrated collectively in Figure A.4. To deal with this issue one calculates n different volumes for each hex cell: one for each chosen diagonalizing scheme, and then averages the n volumes. This can prove to be computationally costly (as just calculating a hex cells volumes using one diagonal reveals later on), however, and for the purposes of determining the material properties (ε_r) of a lens (as was done in Chapter 7), a small amount of error in the hex calculation is acceptable.

It is also important to keep in mind the computational resources required to implement a proposed algorithm. In Figure A.5 the RAM usage and compute time (for V_{hex} calculations) are plotted as a function of hex count. Starting at the coarsest mesh setting (4x4x4), one notes that very little RAM allocation is needed and the solution run time is a fraction of a second. However, this mesh configuration only serves as a starting point in this particular study and would never be of any real use to solving the problems discussed in Chapter 7. It is not until a 64x64x64 mesh is studied that appreciable computational resources are needed in both the form of RAM (about 1 GB) as well as the compute time (about 17 minutes). More importantly, it is clear that the compute time is in fact growing exponentially, while the RAM allocation is growing linearly meaning meaning a parallelization scheme of sorts may be needed to deal with extremely fine volumetric meshes.

Moving on, as was mentioned previously, the mesh required to properly describe a

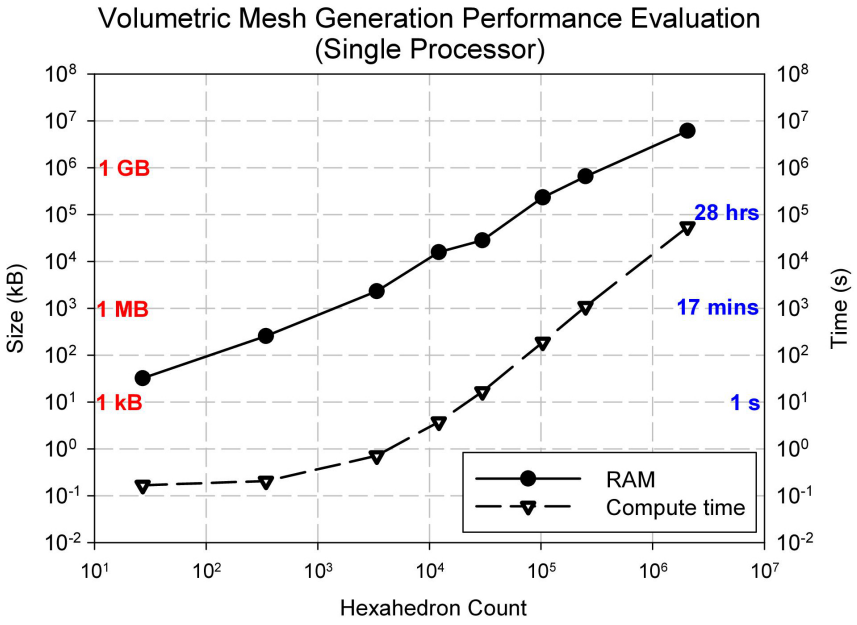

Figure A.5: Volumetric mesh generation resource usage study

structure will ultimately vary from case-to-case, but the very last set of data points in Figure A.5 (128x128x128 mesh (2,097,152 hexahedron cells)) is more representative of what one would expect to have to solve for when dealing with electrically large lenses that have a truly arbitrary shape (those proposed in Chapter 7). For this particular hex count, the amount of required RAM is 5.4 GB which is more-or-less the upper-limits of a typical laptop's capabilities (see Table A.2) and the compute time is about 15 hours. Here it is important to note that the solution to V_{hex} is solved for serially (not in parallel) which means that the compute time is directly related to the clock speed of the processor on which it is running, and not on any core configuration (e.g. dual, quad, etc.) More details concerning processor specifications that were used in this study can be found in Table A.2 in the Viglen Vig800s column.

A.4 Computational resources

Unless otherwise noted, the numerical algorithms developed and used throughout this thesis were carried out on the computers listed in Table A.2.

Computer	Viglen Vig800s (desktop)	Lenovo U410 (laptop)
RAM (GB)	32	8
Processor	Intel i5-3570K [130]	Intel i7-3537U [131]
Cache (MB)	6	4
Cores	4	2
Threads per core	1	2
Base freq. (GHz)	3.4	2.0
OS	Fedora 20	Windows 8.1
System Type	64 bit	64 bit

Table A.2: Computer specifications used in numerical testing.

References

[1] Leonhardt, U. and Philbin, T.G. *Geometry and Light: The Science of Invisibilty*. Dover, Mineola (2010). 7, 8, 10, 12, 16, 17, 19, 20, 24

[2] Jackson, J. *Classical Electrodynamics*. Wiley, New York, third edition (1999). 7, 9

[3] Kay, D.C. *Tensor Calculus*. McGraw Hill, New York (2011). 8, 20

[4] Priestly, A. *Elementary Differential Geometry*. Springer, second edition (2012).

[5] do Carmo, M.P. *Differential geometry of curves and surfaces*. Prentice-Hall, London (1976).

[6] Gray, A. *Modern Differential Geometry of Curves and Surfaces with Mathematica*. CRC Press, Boca Rotan, second edition (1997). 87

[7] Kuhnel, W. *Differential Geometry: Curves-Surfaces-Manifolds*. American Mathematical Society, Providence, second edition (2005).

[8] Burke, W. *Applied Differential Geometry*. Cambridge University Press, Cambridge (1985). 8

[9] Born, M. and Wolf, E. *Principles of Optics*. Cambridge University Press, Cambridge, 7th edition (1999). 10, 15, 17

[10] Riley, K., Hobson, M., and Bence, S. *Mathematical Methods for Physicis and Engineering*. Cambridge University Press, Cambridge (1998). 15

[11] Weisstein, E.W. Geometry. http://mathworld.wolfram.com/Geometry.html (accessed on: 19-06-2015). 19

[12] Szudzik, M. and Weisstein, E.W. Parallel postulate. http://mathworld.wolfram.com/ParallelPostulate.html (accessed on: 17-04-2015). 19

[13] Chernavski, A.V. Manifold. http://www.encyclopediaofmath.org/index.php?title=Manifold&oldid=23893 (accessed on: 19-04-2015). 19

[14] Laptev, B.L. Lobachevskii geometry. http://www.encyclopediaofmath.org/index.php?title=Lobachevskii_geometry&oldid=12005 (accessed on: 19-04-2015). 20

[15] Weisstein, E.W. Pseudosphere. http://mathworld.wolfram.com/Pseudosphere.html (accessed on: 19-04-2015). 20

[16] Ivanov, A.B. Elliptic geometry. http://www.encyclopediaofmath.org/index.php?title=Elliptic_geometry&oldid=15989 (accessed on: 19-04-2015). 20

[17] Pendry, J.B., Schurig, D., and Smith, D.R. Controlling electromagnetic fields. *Science (New York, N.Y.)*, **312**, 1780 (2006). 22, 23, 26, 30

[18] Leonhardt, U. Optical conformal mapping. *Science (New York, N.Y.)*, **312**, 1777 (2006). 22, 23, 26, 30

[19] Leonhardt, U. and Philbin, T.G. General relativity in electrical engineering. *New Journal of Physics*, **8** (2006). 22

[20] Guenneau, S., Amra, C., and Veynante, D. Transformation thermodynamics: cloaking and concentrating heat flux (2012). 22

[21] Han, T., Bai, X., Gao, D., Thong, J.T.L., Li, B., and Qiu, C.W. Experimental Demonstration of a Bilayer Thermal Cloak. *Physical Review Letters*, **112**, 054302 (2014). 22

[22] Farhat, M., Enoch, S., Guenneau, S., and Movchan, A.B. Broadband cylindrical acoustic cloak for linear surface waves in a fluid. *Physical Review Letters*, **101** (2008). 22

[23] Zhang, S., Xia, C., and Fang, N. Broadband Acoustic Cloak for Ultrasound Waves. *Physical Review Letters*, **106**, 024301 (2011). 22

[24] Farhat, M., Guenneau, S., and Enoch, S. Ultrabroadband Elastic Cloaking in Thin Plates. *Physical Review Letters*, **103**, 024301 (2009). 22

[25] Bückmann, T., Thiel, M., Kadic, M., Schittny, R., and Wegener, M. An elasto-mechanical unfeelability cloak made of pentamode metamaterials. *Nature Communications*, **5** (2014). 22

[26] Urzhumov, Y.A. and Smith, D.R. Fluid flow control with transformation media. *Physical Review Letters*, **107** (2011). 22

[27] Urzhumov, Y.A. and Smith, D.R. Flow stabilization with active hydrodynamic cloaks. *Physical Review E*, **86**, 056313 (2012). 22

[28] Ma, Y., Liu, Y., Raza, M., Wang, Y., and He, S. Experimental Demonstration of a Multiphysics Cloak: Manipulating Heat Flux and Electric Current Simultaneously. *Physical Review Letters*, **113**, 205501 (2014). 22

[29] Xu, J., Jiang, X., Fang, N., Georget, E., Abdeddaim, R., Geffrin, J.M., Farhat, M., Sabouroux, P., Enoch, S., and Guenneau, S. Molding acoustic, electromagnetic and water waves with a single cloak. *Scientific Reports*, **5**, 10678 (2015). 22

[30] Schurig, D., Pendry, J.B., and Smith, D.R. Calculation of material properties and ray tracing in transformation media. *Optics express*, **14**, 9794 (2006). 23

[31] Schurig, D., Mock, J.J., Justice, B.J., Cummer, S.A., Pendry, J.B., Starr, A.F., and Smith, D.R. Metamaterial Electromagnetic Cloak at Microwave Frequencies. *Science*, **314**, 977 (2006). 23, 30

[32] Kong, F., Wu, B.I., Kong, J.A., Huangfu, J., Xi, S., and Chen, H. Planar focusing antenna design by using coordinate transformation technology. *Applied Physics Letters*, **91** (2007). 23

[33] Li, J. and Pendry, J.B. Hiding under the carpet: A new strategy for cloaking. *Physical Review Letters*, **101** (2008). 23, 25, 30

[34] Ochiai, T., Leonhardt, U., and Nacher, J.C. A novel design of dielectric perfect invisibility devices. *Journal of Mathematical Physics*, **49**, 032903 (2008). 23

[35] Kwon, D.H. and Werner, D.H. Beam scanning using flat transformation electromagnetic focusing lenses. *IEEE Antennas and Wireless Propagation Letters*, **8**, 1115 (2009). 23

[36] Liu, R., Ji, C., Mock, J.J., Chin, J.Y., Cui, T.J., and Smith, D.R. Broadband ground-plane cloak. *Science (New York, N.Y.)*, **323**, 366 (2009). 23, 30

[37] Valentine, J., Li, J., Zentgraf, T., Bartal, G., and Zhang, X. An optical cloak made of dielectrics. *Nature materials*, **8**, 568 (2009). 23, 30, 123

[38] Hao, Y. and Mittra, R. *FDTD modeling of metamaterials: theory and applications*. Artech House, Boston (2009). 24

[39] Lai, Y., Ng, J., Chen, H., Han, D., Xiao, J., Zhang, Z.Q., and Chan, C.T. Illusion optics: The optical transformation of an object into another object. *Physical Review Letters*, **102** (2009). 24

[40] Lai, Y., Chen, H., Zhang, Z.Q., and Chan, C.T. Complementary media invisibility cloak that cloaks objects at a distance outside the cloaking shell. *Physical Review Letters*, **102** (2009). 24

[41] Guevara Vasquez, F., Milton, G.W., and Onofrei, D. Broadband exterior cloaking. *Optics Express*, **17**, 14800 (2009). 24

[42] Chen, T. and Yu, S.R. Design of optical cloaks and illusion devices along a circumferential direction in curvilinear coordinates. *Journal of Applied Physics*, **108** (2010). 24

[43] Huidobro, P.A., Nesterov, M.L., Martin-Moreno, L., and Garcia-Vidal, F.J. Transformation Optics for Plasmonics. *Nano Letters*, **10**, 1985 (2010). 24, 30, 31, 51, 52, 73, 100, 117, 119

[44] Kadic, M., Guenneau, S., and Enoch, S. Transformational plasmonics: cloak, concentrator and rotator for SPPs. *Optics express*, **18**, 12027 (2010). 24, 31, 52, 73, 100, 117

[45] Tang, W., Argyropoulos, C., Kallos, E., Song, W., and Hao, Y. Discrete coordinate transformation for designing all-dielectric flat antennas. *IEEE Transactions on Antennas and Propagation*, **58**, 3795 (2010). 24, 123

[46] Tang, W. *Coordinate Transformation Based Electromagnetic Design and Application*. Ph.D. thesis, Queen Mary, University of London (2012). 24, 25, 87

[47] Bao, D. *Design and Application of Optical Transformation Devices*. Ph.D. thesis, Queen Mary, University of London (2012). 24, 87

[48] Zheng, H.H., Xiao, J.J., Lai, Y., and Chan, C.T. Exterior optical cloaking and illusions by using active sources: A boundary element perspective. *Physical Review B*, **81**, 195116 (2010). 24, 30

[49] Ozgun, O. and Kuzuoglu, M. Form Invariance of Maxwell's Equations: The Pathway to Novel Metamaterial Specifications for Electromagnetic Reshaping. *IEEE Antennas and Propagation Magazine*, **52**, 51 (2010). 24

[50] Argyropoulos, C., Kallos, E., and Hao, Y. Bandwidth evaluation of dispersive transformation electromagnetics based devices. *Applied Physics A: Materials Science and Processing*, **103**, 715 (2011). 24

[51] Selvanayagam, M. and Eleftheriades, G.V. Transmission-line metamaterials on a skewed lattice for transformation electromagnetics. In *IEEE Transactions on Microwave Theory and Techniques*, volume 59, pages 3272–3282 (2011). ISBN 0018-9480. 24

[52] Yang, R., Tang, W., and Hao, Y. Wideband beam-steerable flat reflectors via transformation optics. *IEEE Antennas and Wireless Propagation Letters*, **10**, 1290 (2011). 25, 123

[53] Yang, R., Tang, W., and Hao, Y. A broadband zone plate lens from transformation optics. *Optics express*, **19**, 12348 (2011). 25, 123

[54] Chen, X., Luo, Y., Zhang, J., Jiang, K., Pendry, J.B., and Zhang, S. Macroscopic invisibility cloaking of visible light. *Nature Communications*, **2**, 176 (2011). 25, 30

[55] Wu, Q., Turpin, J.P., Werner, D.H., Werner, P.L., Tang, W., and Hao, Y. Flat collimating lenses based on quasi-conformal transformation electromagnetics. In *2012 6th European Conference on Antennas and Propagation (EUCAP)*, pages 1696–1700. IEEE (2012). ISBN 978-1-4577-0920-3. 25, 123

[56] Aghanejad, I., Abiri, H., and Yahaghi, A. Design of High-Gain Lens Antenna by Gradient-Index Metamaterials Using Transformation Optics. *IEEE Transactions on Antennas and Propagation*, **60**, 4074 (2012). 25

[57] Kwon, D.H. and Emiroglu, C.D. Non-orthogonal grids in two-dimensional transmission-line metamaterials. *IEEE Transactions on Antennas and Propagation*, **60**, 4210 (2012). 25, 96

[58] Tang, W., Hao, Y., and Mittra, R. Design of a Carpet Cloak to Conceal an Antenna Located Underneath. *IEEE Transactions on Antennas and Propagation*, **60**, 4444 (2012). 25

[59] Navau, C., Prat-Camps, J., and Sanchez, A. Magnetic Energy Harvesting and Concentration at a Distance by Transformation Optics. *Physical Review Letters*, **109**, 263903 (2012). 25

[60] Zhu, W., Rukhlenko, I.D., and Premaratne, M. Linear transformation optics for plasmonics. *Journal of the Optical Society of America B*, **29**, 2659 (2012). 25, 31, 52, 73, 100, 117

[61] Werner, D.H. and Kwon, D.H. *Transformation Electromagnetics and Metamaterials*. Springer, London (2013). 25

[62] Shen, X. and Cui, T. Conformal surface plasmons propagating on ultrathin and flexible films. *Proceedings of the ...*, **110**, 40 (2013). 25

[63] Li, T., Huang, M., Yang, J., Zhu, W., and Zeng, J. A Novel Method for Designing Electromagnetic Shrinking Device With Homogeneous Material Parameters. *IEEE Transactions on Magnetics*, **49**, 5280 (2013). 25

[64] Wu, Q., Jiang, Z.H., Quevedo-Teruel, O., Turpin, J.P., Tang, W., Hao, Y., and Werner, D.H. Transformation Optics Inspired Multibeam Lens Antennas for Broadband Directive Radiation. *IEEE Transactions on Antennas and Propagation*, **61**, 5910 (2013). 25, 100, 117

[65] Ma, Q., Mei, Z.L., Zhu, S.K., Jin, T.Y., and Cui, T.J. Experiments on Active Cloaking and Illusion for Laplace Equation. *Physical Review Letters*, **111**, 173901 (2013). 26

[66] Kraft, M., Pendry, J.B., Maier, S.A., and Luo, Y. Transformation optics and hidden symmetries. *Physical Review B*, **89**, 245125 (2014). 26

[67] Kinsler, P. and McCall, M.W. Transformation devices: Event carpets in space and space-time. *Physical Review A*, **89**, 063818 (2014). 26

[68] Ginis, V., Danckaert, J., Veretennicoff, I., and Tassin, P. Controlling Cherenkov Radiation with Transformation-Optical Metamaterials. *Physical Review Letters*, **113**, 167402 (2014). 26

[69] Oliveri, G., Bekele, E.T., Werner, D.H., Turpin, J.P., and Massa, A. Generalized QCTO for Metamaterial-Lens-Coated Conformal Arrays. *IEEE Transactions on Antennas and Propagation*, **62**, 4089 (2014). 26

[70] Mateo-Segura, C., Dyke, A., Dyke, H., Haq, S., and Hao, Y. Flat Luneburg Lens via Transformation Optics for Directive Antenna Applications. *IEEE Transactions on Antennas and Propagation*, **62**, 1945 (2014). 26

[71] Horsley, S.a.R., Hooper, I.R., Mitchell-Thomas, R.C., and Quevedo-Teruel, O. Removing singular refractive indices with sculpted surfaces. *Scientific Reports*, **4**, 4876 (2014). 26, 36, 56, 58, 63

[72] Xu, L. and Chen, H. Conformal transformation optics. *Nature Photonics*, **9**, 15 (2014). 26

[73] Kraft, M., Luo, Y., Maier, S.A., and Pendry, J.B. Designing Plasmonic Gratings with Transformation Optics. *Physical Review X*, **5**, 031029 (2015). 26

[74] Junqueira, M.A.F.C., Gabrielli, L.H., and Spadoti, D.H. Comparison of Anisotropy Reduction Strategies for Transformation Optics Designs. *IEEE Photonics Journal*, **7**, 1 (2015). 26, 100, 117

[75] Boston, S.R. Time travel in transformation optics: Metamaterials with closed null geodesics. *Physical Review D*, **91**, 124035 (2015). 26

[76] Thompson, R.T. and Fathi, M. Shrinking cloaks in expanding space-times: The role of coordinates and the meaning of transformations in transformation optics. *Physical Review A*, **92**, 013834 (2015). 26

[77] Leonhardt, U. and Tyc, T. Broadband invisibility by non-Euclidean cloaking. *Science (New York, N.Y.)*, **323**, 110 (2009). 27, 28, 30

[78] Tyc, T., Chen, H., Chan, C.T., and Leonhardt, U. Non-euclidean cloaking for light waves. *IEEE Journal on Selected Topics in Quantum Electronics*, **16**, 418 (2010). 27, 61

[79] Yao, K., Jiang, X., and Chen, H. Collimating lenses from non-Euclidean transformation optics. *New Journal of Physics*, **14** (2012). 27, 28

[80] Liu, Y., Zentgraf, T., Bartal, G., and Zhang, X. Transformational Plasmon Optics. *Nano Letters*, **10**, 1991 (2010). 30, 31, 51, 52, 73, 100, 117, 119

[81] Huidobro, P.A., Nesterov, M.L., Martín-Moreno, L., and García-Vidal, F.J. Moulding the flow of surface plasmons using conformal and quasi-conformal mappings. *New Journal of Physics*, **13**, 033011 (2011). 30, 31, 52, 100, 117, 123

[82] Kadic, M., Dupont, G., Guenneau, S., and Enoch, S. Controlling surface plasmon polaritons in transformed coordinates. *Journal of Modern Optics*, **58**, 994 (2011). 31, 52, 73, 100, 117

[83] Yang, R., Lei, Z., Chen, L., Wang, Z., and Hao, Y. Surface wave transformation lens antennas. *IEEE Transactions on Antennas and Propagation*, **62**, 973 (2014). 31, 52

[84] MathWorks. MATLAB R2015a (2015). 37, 82

[85] MathWorks. Symbolic ode solver. http://uk.mathworks.com/help/symbolic/dsolve.html (accessed on: 6-12-2015). 37

[86] MathWorks. Numeric ode solver. http://uk.mathworks.com/help/symbolic/mupad_ref/numeric-odesolve.html (accessed on: 6-12-2015). 37

[87] Rehmann, U. Runge-kutta method. https://www.encyclopediaofmath.org/index.php?title=Runge-Kutta_method&oldid=22999 (accessed on: 6-12-2015). 37

[88] Walter, C. Surface-wave luneberg lens antennas. *IRE Transactions on Antennas and Propagation*, **8** (1960). 38, 63, 89

[89] Technology, C.C.S. CST Microwave Studio (2014). 48, 68

[90] Volakis, J. *Antenna Engineering Handbook*. McGraw Hill, New York, fourth edition (2007). 50

[91] Monticone, F. and Alu, A. Leaky-Wave Theory, Techniques, and Applications: From Microwaves to Visible Frequencies. *Proceedings of the IEEE*, **103**, 793 (2015).

[92] Zucker, F. and Collin, R. *Surface-Wave Antennas*. McGraw Hill, New York (1969). 96

[93] Walter, C. *Traveling Wave Antennas*. McGraw Hill, Los Altos (1990).

[94] Rozzi, T. and Mongiardo, M. *Open Electromagnetic Waveguides*. The Institution of Electrical Engineers, London (1997).

[95] Marcuvitz, N. *Waveguide Handbook*. McGraw Hill, London (1951).

[96] Shevchenko, V.V. *Continuous transitions in open waveguides: introduction to theory*. The Golem Press, Boulder (1971). 50

[97] Mitchell-Thomas, R.C., McManus, T.M., Quevedo-Teruel, O., Horsley, S.A.R., and Hao, Y. Perfect surface wave cloaks. *Physical Review Letters*, **111** (2013). 52, 73

[98] Chen, T. and Yu, S.R. An electromagnetic black hole made of metamaterials. http://arxiv.org/abs/0910.2159 (2009). 54

[99] Luneburg, R.K. *Mathematical Theory of Optics*. Brown University, Providence (1944). 56, 59

[100] Gutman, A.S. Modified Luneberg Lens. *Journal of Applied Physics*, **25**, 855 (1954). 56

[101] Šarbort, M. and Tyc, T. Spherical media and geodesic lenses in geometrical optics (2012). 56, 60

[102] Berry, M.V. Attenuation and focusing of electromagnetic surface waves rounding gentle bends (2001). 61

[103] Parker, E. and Sanz-Izquierdo, B. 3D printing technique for fabrication of frequency selective structures for built environment. *Electronics Letters*, **49**, 1117 (2013). 67

[104] Macdonald, E., Salas, R., Espalin, D., Perez, M., Aguilera, E., Muse, D., and Wicker, R.B. 3D Printing for the Rapid Prototyping of Structural Electronics. *IEEE Access*, **2**, 234 (2014).

[105] Barton, J.H., Garcia, C.R., Berry, E.A., Salas, R., and Rumpf, R.C. 3-D Printed All-Dielectric Frequency Selective Surface With Large Bandwidth and Field of View. *IEEE Transactions on Antennas and Propagation*, **63**, 1032 (2015).

[106] Deffenbaugh, P.I., Rumpf, R.C., and Church, K.H. Broadband Microwave Frequency Characterization of 3-D Printed Materials. *IEEE Transactions on Components, Packaging and Manufacturing Technology*, **3**, 2147 (2013).

[107] Sanz-Izquierdo, B. and Parker, E.A. 3-D Printing of Elements in Frequency Selective Arrays. *IEEE Transactions on Antennas and Propagation*, **62**, 6060 (2014). 67

[108] Mitchell-Thomas, R.C., Quevedo-Teruel, O., McManus, T.M., Horsley, S.a.R., and Hao, Y. Lenses on curved surfaces. *Optics Letters*, **39**, 3551 (2014). 73

[109] MathWorks. Extrapolate function. http://uk.mathworks.com/help/curvefit/fnxtr.html (accessed on: 6-12-2015). 82

[110] Pointwise Inc. Pointwise 17.3 R4 (2015). 86

[111] Weisstein, E.W. Shoe surface. http://mathworld.wolfram.com/ShoeSurface.html (accessed on: 25-08-2015). 87

[112] Incorporated, C. COMSOL 5.0 (2015). 89

[113] Maci, S., Minatti, G., Casaletti, M., and Bosiljevac, M. Metasurfing: Addressing Waves on Impenetrable Metasurfaces. *IEEE Antennas and Wireless Propagation Letters*, **10**, 1499 (2011). 96

[114] Yu, N. and Capasso, F. Flat optics with designer metasurfaces. *Nature Materials*, **13**, 139 (2014). 96

[115] Patel, A.M. and Grbic, A. Transformation Electromagnetics Devices Based on Printed-Circuit Tensor Impedance Surfaces. *IEEE Transactions on Microwave Theory and Techniques*, **62**, 1102 (2014). 96

[116] Martini, E., Sardi, G.M., and Maci, S. Homogenization Processes and Retrieval of Equivalent Constitutive Parameters for Multisurface-Metamaterials. *IEEE TRANSACTIONS ON ANTENNAS AND PROPAGATION*, **62** (2014). 96

[117] Zedler, M. and Eleftheriades, G.V. Anisotropic transmission-line metamaterials for 2-d transformation optics applications. *Proceedings of the IEEE*, **99**, 1634 (2011). 96

[118] Quarfoth, R. and Sievenpiper, D. Surface Wave Scattering Reduction Using Beam Shifters. *IEEE Antennas and Wireless Propagation Letters*, **13**, 963 (2014). 96

[119] Gok, G. and Grbic, A. Tensor transmission-line metamaterials. *IEEE Transactions on Antennas and Propagation*, **58**, 1559 (2010). 96

[120] Gok, G. and Grbic, A. Alternative Material Parameters for Transformation Electromagnetics Designs. *IEEE Transactions on Microwave Theory and Techniques*, **61**, 1414 (2013). 96

[121] Bao, D., Mitchell-Thomas, R.C., Rajab, K.Z., and Hao, Y. Quantitative Study of Two Experimental Demonstrations of a Carpet Cloak. *IEEE Antennas and Wireless Propagation Letters*, **12**, 206 (2013). 100

[122] Weisstein, E.W. Non-orientable surface. http://mathworld.wolfram.com/NonorientableSurface.html (accessed on: 14-05-2015). 129

[123] Weisstein, E.W. Sphere. http://mathworld.wolfram.com/Sphere.html (accessed on: 14-05-2015). 129

[124] Weisstein, E.W. Möbius strip. http://mathworld.wolfram.com/MoebiusStrip.html (accessed on: 14-05-2015). 129

[125] Machon, T. and Alexander, G.P. Knots and nonorientable surfaces in chiral nematics. *Proceedings of the National Academy of Sciences of the United States of America*, **110**, 14174 (2013). 129

[126] Weisstein, E.W. Klein bottle. http://mathworld.wolfram.com/KleinBottle.html (accessed on: 14-05-2015). 130

[127] Kuiper, N.H. Convex immersions of closed surfaces in E3 - Non-orientable closed surfaces in E3 with minimal total absolute Gauss-curvature. *Commentarii Mathematici Helvetici*, **35**, 85 (1961). 130

[128] Hao, Y. Quest epsrc grant. http://gow.epsrc.ac.uk/NGBOViewGrant.aspx?GrantRef=EP/I034548/1 (accessed on: 25-03-2015). 133

[129] Grandy, J. Efficient computation of volume of hexahedral cells. http://www.osti.gov/scitech/servlets/purl/632793 (accessed on: 25-06-2015). 138

[130] Intel. Intel core i5-3570k processor. http://ark.intel.com/products/65520/Intel-Core-i5-3570K-Processor-6M-Cache-up-to-3_80-GHz (accessed on: 3-09-2015). 142

[131] Intel. Intel core i7-3537u processor. http://ark.intel.com/products/72054/Intel-Core-i7-3537U-Processor-4M-Cache-up-to-3_10-GHz?q=i7-3537U (accessed on: 3-09-2015). 142